NTNU – Trondheim
Norwegian University of
Science and Technology

Effect of Cathodic Polarization on the Susceptibility to Hydrogen Embrittlement in 5xxx, 6xxx and 7xxx Series Aluminium Alloys

Kjetil Fossland Veium

Chemical Engineering and Biotechnology
Submission date: June 2015
Supervisor: Trond Furu, IMTE
Co-supervisor: Roy Johnsen, IPM
Otto Lunder, IMTE

Norwegian University of Science and Technology
Department of Materials Science and Engineering

Preface

This master's thesis is submitted to the Norwegian University of Science and Technology (NTNU) as a part of the master's degree program Chemical Engineering and Biotechnology at Department of Materials Science and Engineering (DMSE). The project has been a collaboration between NTNU and Hydro, with Dr. Trond Furu as the main supervisor together with Professor Roy Johnsen and Dr. Otto Lunder as co-supervisors.

Acknowledgement

First of all, I would like to give a special thanks to my co-supervisor Professor Roy Johnsen for all help and guidance during the project period. I really appreciate his engagement, helpfulness and ability to provide constructive feedback. Not to forget his impressive ability to answer questions at any time, despite a busy schedule. I would also like to thank my supervisor Dr. Trond Furu and my co-supervisor Dr. Otto Lunder for valuable meetings and discussions throughout the project period. Furthermore, I am grateful for the financial support from Hydro.

Moreover, I would like to thank Kristian Knarbakk for close cooperation in the lab, and Ph.D candidate Gaute Stenerud, Nils-Inge J. Nilsen and Trygve Lindahl Schanche for help solving practical problems.

Finally, I would like to thank all my fellow students who made the past five years wonderful.

Trondheim, 2015-06-08

Kjetil Fossland Veium

Abstract

Aluminium is an interesting material for use in subsea applications due to the combination of low weight, good corrosion resistance and superior low temperature properties. So far, the use of aluminium alloys in offshore applications has mainly been restricted to topside structures. In order to use these alloys in subsea structures and components, there is a need for cathodic protection (CP) to avoid corrosion in contact with more noble metals. CP represents a source of hydrogen, and this may pose a threat to hydrogen embrittlement (HE).

In this study the effect of cathodic polarization on the susceptibility to HE in several variants of Al-Mg (5xxx), Al-Mg-Si (6xxx) and Al-Zn-Mg (7xxx) aluminium alloys was investigated. A stepwise loading tensile test with in situ cathodic polarization was performed on hydrogen pre-charged samples and on not pre-charged samples. In addition, reference samples were tensile tested in air. Fracture surfaces were examined using scanning electron microscope (SEM), and reduction of area (RA) measurements were also performed. The planned measurements of hydrogen content and microhardness were not conducted.

The results from this study indicate an effect of cathodic polarization on the susceptibility to HE in AA 7108.50, manifested by a decline in average fracture strength (FS) between reference samples and hydrogen pre-charged samples, respectively. Moreover, features associated with transgranular cleavage fractures were revealed from fractography. The EN AW 5083 H321 and EN AW 6082 T6 alloy variants do not seem to be particularly vulnerable to HE, regardless of both composition and thermal history. Minor variations in FS were found between reference samples and hydrogen pre-charged samples, and only ductile features were revealed from the fracture surface examinations. The reduction of area (RA) measurements were not included in the overall assessment of susceptibility to HE due to large inconsistency with the other test results. It should be emphasized that measurement of hydrogen content and execution of experiments in which several parallels of samples are tested are crucial for verification of the findings from this study.

Sammendrag

Aluminium er et interessant materiale for bruk i subsea applikasjoner på grunn av kombinasjonen av lav vekt, god korrosjonsmotstand og utmerkede lavtemperaturegenskaper. Frem til nå har bruken av aluminiumslegeringer i offshore applikasjoner hovedsakelig vært begrenset til topside strukturer. For å kunne bruke disse legeringene i subsea strukturer- og komponenter, trengs det katodisk beskyttelse (CP) for å unngå korrosjon i kontakt med mer edle metaller. Katodisk beskyttelse (CP) representerer en kilde til hydrogen, og dette kan utgjøre en fare for hydrogensprøhet (HE).

I denne studien ble effekten av katodisk polarisering på mottakelighet for hydrogensprøhet (HE) undersøkt i flere varianter av Al-Mg (5xxx), Al-Mg-Si (6xxx) og Al-Zn-Mg (7xxx) aluminiumslegeringer. Stegvis strekktesting med in situ katodisk polarisering ble gjennomført på prøver forladet med hydrogen samt prøver uten forlading. I tillegg ble referanseprøver strekktestet i luft. Bruddoverflatene ble undersøkt ved bruk av et scanning elektronmikroskop (SEM), og målinger av reduksjon i areal ble også utført. De planlagte målingene av hydrogeninnhold og mikrohardhet ble ikke gjennomført.

Resultatene fra denne studien indikerer at det er en effekt av katodisk polarisering på mottakelighet til hydrogensprøhet (HE) i AA 7108.50, markert med en nedgang i gjennomsnittlig bruddspenning (FS) mellom referanseprøver og prøver forladet med hydrogen. Videre ble det avdekket funn som kan assosieres med transgranulære kløyvningsbrudd fra fraktografi. Legeringsvariantene fra EN AW 5083 H321 og EN AW 6082 T6 ser ikke ut til å være særlig utsatt for hydrogensprøhet (HE), uavhengig av både sammensetning og varmebehandlingsmetoder. Små variasjoner i bruddstyrke (FS) ble funnet mellom referanseprøver og prøver forladet med hydrogen, og kun duktile kjennetegn ble avdekket fra bruddoverflateundersøkelsene. Målingene av reduksjon i areal ble ikke inkludert i helhetsvurderingen angående mottakelighet for hydrogensprøhet (HE) på grunn av høy uoverensstemmelse med de øvrige resultatene. Det bør understrekes at måling av hydrogeninnhold samt gjennomføring av eksperiment der flere paralleller av prøver testes er avgjørende for verifisering av funnene fra denne studien.

Contents

List of Abbreviations

A	Cross sectional area
AA	Aluminium Association standard
AD	Anodic Dissolution
a	Crack length
b	Tafel slope
b_a	Anodic Tafel constant
b_c	Cathodic Tafel constant
β	Equilibrium phase (Al_3Mg_2) in Al-Mg (5xxx) alloys
bcc	Body-centered cubic
CP	Cathodic Protection
D	Diffusivity
DCB	Double Cantilever Beam
DMSE	Department of Materials Science and Engineering
DSS	Duplex Stainless Steel
E_c	Cathodic potential
E_{corr}	Corrosion potential
EDXA	Energy-dispersive X-ray Analysis
EN AW	European standard
EPMA	Electron Probe Micro Analyzer
F	Load
f	Geometrical factor
fcc	Face-centered cubic
FPZ	Fracture Process Zone
FS	Fracture Strength
HAZ	Heat Affected Zone
HE	Hydrogen Embrittlement
HEDE	Hydrogen Enhanced Decohesion
HELP	Hydrogen Enhanced Local Plasticity
HER	Hydrogen Evolution Reaction

I^+_{Al}	Aluminium Ion Current
I^+_H	Hydrogen Ion Current
i	Current density
i_c	Cathodic current density
i_0	Exchange current density
K	Stress-intensity factor
K_{ISCC}	Threshold stress intensity level
L	Longitudinal direction
LVFESEM	Low Voltage Field Emission Scanning Electron Microscope
MIG	Metal Inert Gas
η	Overpotential
η	Equilibrium phase ($MgZn_2$) in Al-Zn-Mg (7xxx) alloys
η_a	Anodic overpotential
η_c	Cathodic overpotential
NTNU	Norwegian University of Science and Technology
OCP	Open Circuit Potential
R	Gas constant
R_m	Tensile strength
$R_{p0.2}$	Yield strength
RA	Reduction of Area
RA_{air}	Reduction of Area for reference samples
$RA_{charged}$	Reduction of Area for hydrogen pre-charged samples
RA_{loss}	Loss in Reduction of Area
RDS	Rate-determing Step
RRA	Retrogression and Re-ageing
RT	Room Temperature
S	Short-transverse direction
SCC	Stress Corrosion Cracking
SCE	Saturated Calomel Reference Electrode
SD	Standard Deviation
SDSS	Super Duplex Stainless Steel
SEM	Scanning Electron Microscope
SET	Straining Electrode Test

SMSS	Supermartensitic Stainless Steel
SS	Stainless Steel
SSRT	Slow Strain Rate Testing
SSSS	Supersaturated Solid Solution
T	Transverse direction
T	Temperature
TEM	Transmission Electron Microscope
TIG	Tungsten Inert Gas
v	Crack growth rate
wppm	Weight-parts per million
WVSA	Water Vapour Saturated Air
σ	Stress

Chapter 1

Introduction

The demands for cost effective transportation and installation solutions for the offshore oil & and gas industry makes aluminium an interesting material, especially for subsea structures and components. The density of aluminium is approximately 1/3 compared to steel, which allows considerable weight savings. Aluminium also has the ability to maintain ductility at low temperatures. This is particularly interesting as the offshore oil & and gas industry is moving further north and with possible future advancement into the Arctic region.

The use of aluminium in offshore applications has mainly been restricted to topside structures such as helicopter decks and living quarters [1]. As a result, there is limited literature on, and experience with use of aluminium for subsea activities. A general misconception about aluminium alloys in seawater is that they are non-corrosion resistant due to usage in sacrificial anodes for corrosion protection. It turns out, however, that certain Al-Mg (5xxx) and Al-Mg-Si (6xxx) alloys exhibit excellent corrosion resistance as long as galvanic contact with more noble metals is avoided [2, 3]. According to standards all subsea components should be protected against corrosion by use of coating in combination with cathodic protection (CP) [4]. Reliable CP systems may, therefore, allow aluminium alloys to be used in connection with other metals, without suffering from corrosion.

CP systems provide a source of hydrogen. Hydrogen embrittlement (HE) is known to pose a threat to different metals and this may also be the case for aluminium alloys. However, limited literature is available on this topic. The current studies regarding effect of cathodic polarization on the susceptibility to HE are mainly confined to high-strength Al-Zn-Mg (-Cu) (7xxx) alloys [5–10], and the experiments have been performed under considerably lower potentials than what would be expected from normal CP systems. This shows that there is a need for the seawater resistant alloys to be considered in terms of HE, and the experiments need to be done under actual operational conditions.

Previous work

Inspiration for this master's thesis was obtained from previous work performed by the author [11], where susceptibility to HE in Al-Mg (5xxx) and Al-Mg-Si (6xxx) alloys was investigated. The results indicated a negligible susceptibility to HE in these alloys, however the scope of work was restricted due to time limitations. The experience and knowledge gained from the previous work has been valuable for the implementation of this study.

Aim of this work

This study aims to investigate the effect of cathodic polarization on the susceptibility to HE in several variants of Al-Mg (5xxx), Al-Mg-Si (6xxx) and Al-Zn-Mg (7xxx) aluminium alloys. Susceptibility to HE will be assessed from a stepwise loading tensile test, where results from hydrogen pre-charged samples with in situ cathodic polarization, not pre-charged samples with in situ cathodic polarization and reference samples tested in air will be compared. Reduction of area (RA) measurements, hardness measurements, measurement of hydrogen content and fracture surface examinations will also be included in an effort to identify the HE susceptibility. Furthermore, this study aims to include the up-to-date literature about HE in aluminium alloys as well as an extensive review of the role of HE in stress corrosion cracking (SCC).

Chapter 2

Theory

2.1 Background

Aluminium and aluminium alloys exhibit an excellent combination of properties such as low weight, good corrosion resistance, high ductility, formability, electrical and thermal conductivity. Furthermore, aluminium is easily recycled by using only 5 % of the energy initially needed for the primary metal production [12]. Pure aluminium has a relatively low strength, and is therefore most often used in combination with alloying elements such as Cu, Mg, Si, Zn and Mn. The face-centered cubic (fcc) crystal structure of aluminium is illustrated in Figure 2.1.

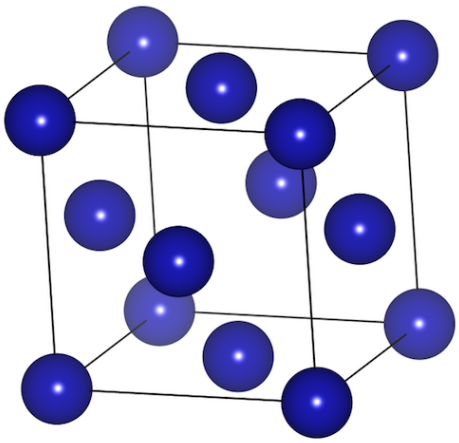

Figure 2.1: The face-centered cubic (fcc) crystal structure of aluminium.

2.1.1 Characterization and temper designations

Wrought aluminium alloys are classified according to the international alloy designation system each with a four-digit number based on composition, alloy additions and level of impurities [13]. A prefix is used to denote the standard AA for Aluminium Association or EN AW for the European standard. Several classes of aluminium alloys are age hardenable from which strength can be achieved through controlled precipitation during heat treatment. Non-heattreatable alloys normally obtain strength from work hardening, grain size reduction (Hall-Petch strengthening) and solid solution effects. Figure 2.2 shows the different series of wrought aluminium alloys associated with their main alloying elements and strengthening categories.

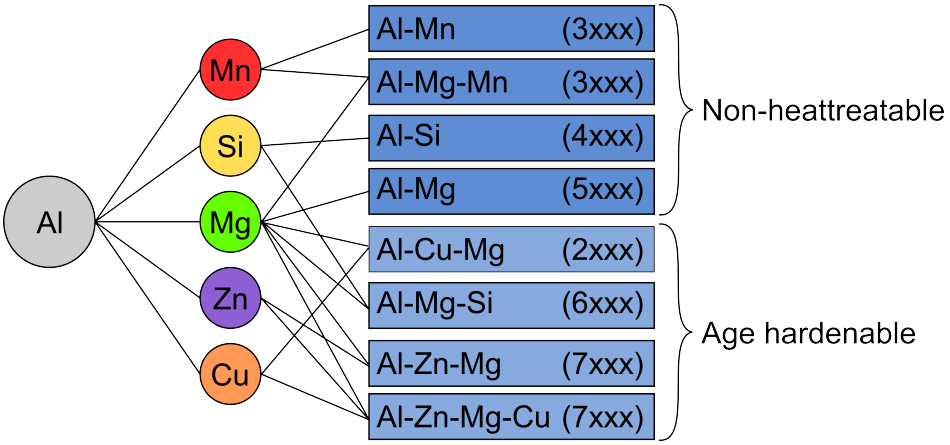

Figure 2.2: Wrought aluminium alloys associated with their main alloying elements and strengthening categories. Modified from [13].

A further nomenclature is used to describe how strength is provided to the alloys. As-fabricated (F) and fully annealed (O) are used for both strengthening categories, while tempered (T) and strain-hardened (H) are used for age hardenable and non-heattreatable alloys, respectively. There are nine different T-tempers, and three of the most common tempers are described in Table 2.1.

Table 2.1: Important T-tempers for age hardenable aluminium alloys [13].

Temper	Description
T3	Solution heat treated - cold worked - naturally aged
T6	Solution heat treated - artificially aged
T7	Solution heat treated - overaged

The strain-hardened (H) tempers are described by at least two additional digits, where the first digit expresses the secondary heat treatment applied and the second digit indicates the degree of strain hardening. A third digit may be used to express variations of the first two digits. Table 2.2 shows the different secondary heat treatments together with the levels of strain hardening.

Table 2.2: Strain-hardened (H) tempers are described by two additional digits, where the first digit expresses the secondary heat treatment applied and the second digit indicates the degree of strain hardening [13].

Secondary heat treatment	**Degree of strain hardening**
1: Cold worked only	2: Quarter hard
2: Cold worked and partially annealed	4: Half hard
3: Cold worked and stabilized	6: Three quarter hard
	8: Hard
	9: Extra hard

A brief introduction to the aluminium alloy series investigated in this study will be given in the following. These are Al-Mg (5xxx) alloys, Al-Mg-Si (6xxx) alloys and Al-Zn-Mg (7xxx) alloys.

2.1.2 Al-Mg (5xxx) alloys

Al-Mg (5xxx) alloys were developed due to demands for sheet materials with higher strength, better formability, increased corrosion resistance and weldability [14]. Typical applications for these alloys include shipbuilding, vehicle bodies and pressure vessels. The major alloying element is Mg, and other elements include of Si, Fe, Cu, Mn, Cr, Zn and Ti. Strength is normally obtained from cold working since the alloys are non-heattreatable. The stacking fault energy of pure aluminium is high, and strengthening by work hardening is hence limited. Addition of Mg reduces the stacking fault energy, and this can impede cross-slip and dislocation climb. Mg is therefore a very important strengthening provider in Al-Mg (5xxx) alloys. Typical mechanical properties for these alloys are given in Table 2.3.

Table 2.3: Selected mechanical properties for Al-Mg (5xxx) alloys [15].

	$R_{p0.2}$ [MPa]	R_m [MPa]	Elongation [%]
Al-Mg (5xxx)	185-345	200-415	6-15

2.1.3 Al-Mg-Si (6xxx) alloys

Al-Mg-Si (6xxx) alloys are characterized by medium strength, good weldability and good corrosion resistance [14]. Typical applications for these alloys include bridges, cranes and beer barrels. The main alloying elements are Mg and Si, while smaller amounts of Fe, Cu, Mn, Cr, Zn and Ti are also often added. In contrast to Al-Mg (5xxx) alloys, Al-Mg-Si (6xxx) alloys are age hardenable from which strength is provided from interactions between dislocations and precipitates formed during ageing. A selection of typical mechanical properties of Al-Mg-Si (6xxx) alloys is presented in Table 2.4.

Table 2.4: Selected mechanical properties for Al-Mg-Si (6xxx) alloys [15].

	$R_{p0.2}$ [MPa]	R_m [MPa]	Elongation [%]
Al-Mg-Si (6xxx)	130-325	210-345	12-26

2.1.4 Al-Zn-Mg (7xxx) alloys

Al-Zn-Mg (7xxx) alloys are known for their high strength, and are often referred to as high-strength aluminium alloys[1] [16]. Their high strength in combination with low density make them widely used within the transportation industry [14]. Zn and Mg are the main alloying elements, but these are often used in combination with smaller amounts of Cu, Cr, Fe, Mn, Si and Ti are often added. Table 2.5 shows typical mechanical properties for Al-Zn-Mg (-Cu) (7xxx) alloys.

Table 2.5: Selected mechanical properties for Al-Zn-Mg (-Cu) (7xxx) alloys [15].

	$R_{p0.2}$ [MPa]	R_m [MPa]	Elongation [%]
Al-Zn-Mg (-Cu) (7xxx)	225-625	340-675	7-18

[1] This term is often used for alloys with a tensile strength higher than 500 MPa, which typically include variants of Al-Cu (2xxx) and Al-Zn-Mg (-Cu) (7xxx) alloys.

2.2 Corrosion behaviour of aluminium

2.2.1 General aspects of corrosion

The use of aluminium and aluminium alloys in the offshore oil & gas industry has mainly been restricted to topside structures such as helicopter decks and living quarters [1]. A common misconception regarding aluminium in seawater is that they are non-corrosion resistant due to usage in sacrificial anodes for corrosion protection of steel structures. However, most alloys in the 3xxx, 5xxx and 6xxx series are resistant to corrosion in seawater, as long as galvanic contact with more noble metals is avoided [3]. Corrosion resistance is obtained from the passive oxide film, formed under natural atmospheric conditions according to Equation 2.1.

$$4\,Al + 3\,O_2 \rightarrow 2\,Al_2O_3 \tag{2.1}$$

Figure 2.3 shows the Pourbaix diagram for aluminium, where the red line indicate seawater conditions (pH 8.2). Apparently, aluminium seems to corrode when being exposed to seawater. However, alloying elements such as Mg and Mn are used to ensure passivation also in slightly alkaline environments. An experimental Pourbaix diagram for AA 5086 in a chloride solution is given in Figure 2.4. As it can be seen, the area passivity is extended to increased pH values due to the alloying elements.

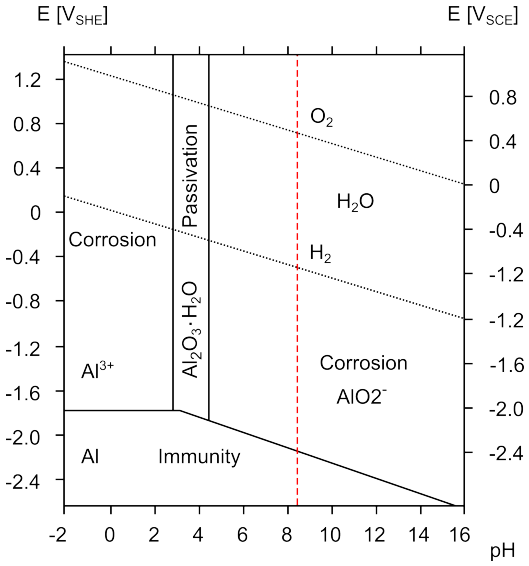

Figure 2.3: Pourbaix diagram for aluminium. Modified from [3].

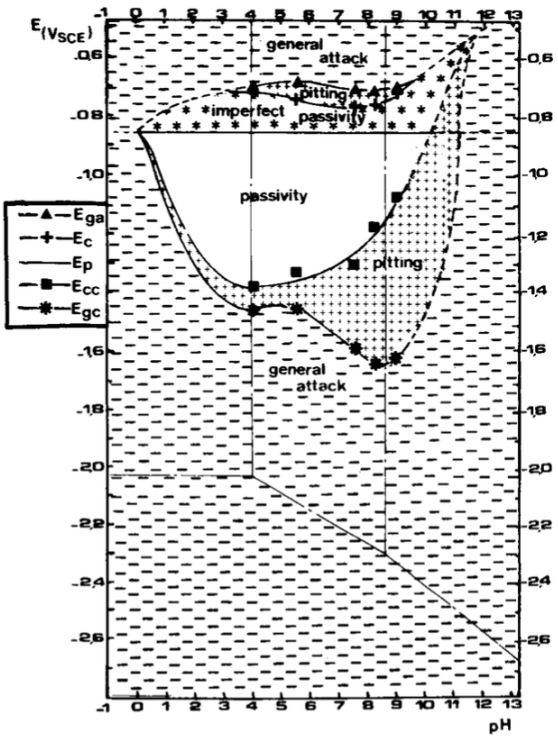

Figure 2.4: Experimental Pourbaix diagram for AA 5086 in a chloride solution [17].

The main concerns regarding corrosion of aluminium include pitting, flow-dependent corrosion and erosion-corrosion. Uniform corrosion, crevice corrosion and intergranular corrosion may also occur, however this can be avoided by appropriate material selection and design.

2.2.2 Pitting

Pitting is a localized corrosion form which occurs due to breakdown of the passivating oxide film. Breakdown is caused by formation of weak spots from flaws at the intermetallic particle-matrix interface. Pitting is believed to occur in almost any aluminium alloy exposed to an aqueous solution in the pH range of 4.5-8.5 [18], and deteriorates by the presence of aggressive ions such as Cl^-. Increased temperature and pressure do also have a negative effect on the pitting resistance [3]. The highest resistance is found for aluminium with high level of purity, while Al-Mg (5xxx) alloys provide the best resistance among the commercial alloys. Al-Cu-Mg (2xxx) alloys are the ones being most susceptible [18].

2.2.3 Effect of flow rate

At higher flow rates, there is a change from localized corrosion to uniform corrosion. The flow rate at which transition occurs is difficult to determine because it depends both on the type of alloy and on the hydrodynamic conditions. Nisancioglu [3] found the transition at a flow rate of about 6 cm/s for Al99.95 and AlMgSi1 as shown in Figure 2.5. Pitting is observed as scatter from the calculated uniform corrosion rate (straight line). These results indicate that AlMg3 exhibit a good pitting resistance for the flow velocities tested.

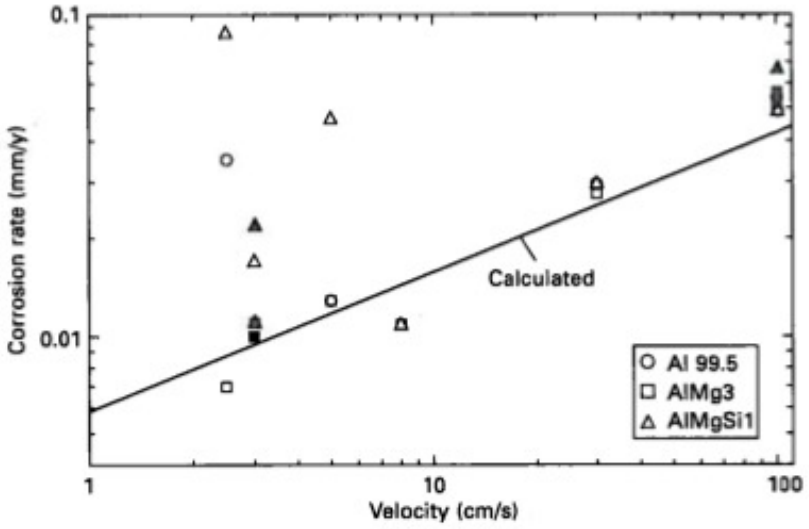

Figure 2.5: Corrosion rate as a function of seawater flow rate. Open-circuit conditions (open), and cathodic protection (CP) at -1000 mV_{SCE} (solid). The data is based on weight loss measurements after two months of exposure [3].

2.2.4 Material selection

Corrosion of aluminium and aluminium alloys in seawater can be restricted by appropriate material selection and design. According to NORSOK M-121 [2], AA 5083 and AA 6082 are the recommended aluminium alloys for use in seawater. These alloys provide the highest strength within their respective alloy classes, and in addition to low density and excellent corrosion resistance this makes them desirable for use in seawater applications [18]. Nevertheless, aluminium alloys will always be used in combination with other materials, and this poses a threat to galvanic corrosion in absence of corrosion protection. All seawater components are therefore protected against corrosion by use of coating in combination with cathodic protection (CP) [4]. Unfortunately, CP represents a source

of hydrogen which may affect the mechanical properties. An extensive review of the presence of hydrogen within aluminium and aluminium alloys will be given in the following.

2.3 Hydrogen in aluminium alloys

A general misconception about fcc materials like aluminium alloys was that they were less affected by the presence of hydrogen than the body-centered cubic (bcc) materials [14]. As a result of that, effects of hydrogen in aluminium have received limited attention in the past. Later years of study have, however, indicated serious significance of the presence of hydrogen within aluminium and aluminium alloys. Before going more deeply into how mechanical properties may be affected by hydrogen, some basic considerations about the presence of hydrogen within a lattice will be reviewed.

2.3.1 Hydrogen from cathodic protection

Hydrogen may be introduced into a metal or an alloy from different sources including welding, corrosion reactions and CP. From the fact that CP is used for corrosion protection, this constitutes the main source of hydrogen for aluminium alloys exposed to seawater. CP is performed by utilizing the effect of galvanic corrosion between two connected metals with different electrochemical potential [19]. Sacrificial anodes are typically made of aluminium and/or zinc alloys. They provide a protection potential in the order of -1050 $mV_{Ag/AgCl}$, which satisfies DNVs recommended practice for carbon and low-alloy steel protection [20]. This ensures that the less noble material corrode at the expense of the structures to be protected. Reduction of oxygen and hydrogen occur simultaneously, which for oxygen in alkaline solutions is given by Equation 2.2.

$$O_2 + 2H_2O + 4e^- \rightarrow 4OH^- \tag{2.2}$$

The overall hydrogen evolution reaction (HER), can be written according to Equation 2.3 [21].

$$2H_2O + 2e^- \rightarrow H_2 + 2OH^- \tag{2.3}$$

Alternatively, the overall HER may be written in two steps, where the first step for alkaline solutions is electrolysis of water to form atomic hydrogen according to Equation 2.4. The metal M provides a potential surface site for atomic hydrogen adsorption, MH_{ads}.

$$H_2O + e^- + M \rightarrow MH_{ads} + OH^- \tag{2.4}$$

Step two depends on both the metal and the cathodic current density, i_c, and includes either chemical desorption or electrochemical desorption to produce gaseous hydrogen according to Equation 2.5 and Equation 2.6, respectively.

$$MH_{ads} + MH_{ads} \rightarrow H_2 + 2M \tag{2.5}$$

$$MH_{ads} + H_2O + e^- \rightarrow H_2 + OH^- + M \tag{2.6}$$

The slowest reaction step from the individual reactions given in Equation 2.4-2.6 determines the rate-determing step (RDS) of the overall HER. Furthermore, the RDS determines i_c and the cathodic overpotential, η_c, which are related through Tafel's equation as shown in Equation 2.7. b_c is the cathodic Tafel constant and i_0 is the exchange current density.

$$\eta_c = b_c \log \frac{i_c}{i_0} \tag{2.7}$$

Cathodic protection of aluminium - different from cathodic protection of steel

There are significant differences between steel and aluminium alloys when it comes to CP. The protective oxide film of aluminium exhibits an amphoteric behaviour, which means that it becomes unstable in acidic or alkaline environments. If applied cathodic potential is too negative, *i.e.* the rate of the cathodic reaction becomes too high, an alkalinization of the metal surface may initiate localized corrosion known as cathodic pitting [3]. Figure 2.6 shows the cathodic polarization curves of freshly exposed aluminium alloys in seawater under almost stagnant conditions. These curves are obtained from work done by Gundersen and Nisancioglu [22]. At an applied potential of -1050 $mV_{Ag/AgCl}$ (-1093 mV_{SCE}), required cathodic current density for AlMg3 is about 8.5 mA/m^2.

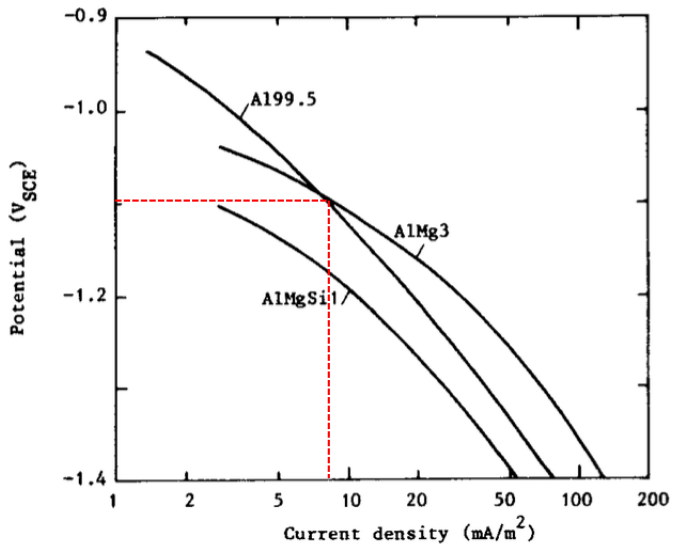

Figure 2.6: Cathodic polarization curves of aluminium alloys exposed to seawater under almost stagnant conditions. The dotted red line indicates the current density requirement for an AlMg3 alloy at an applied potential of -1050 $mV_{Ag/AgCl}$ (-1093 mV_{SCE}). Modified from [22].

The low current density requirements can be understood from a qualitative energy-dispersive x-ray analysis (EDXA) performed by Gundersen and Nisancioglu [22]. A larger amount of Mg relative to Ca was found in deposits on intermetallic particles compared to the matrix. As increased pH makes deposition of $Mg(OH)_2$ more favourable than deposition of $CaCO_3$, this indicates that the oxygen reduction and the hydrogen evolution reactions essentially occur on intermetallic particles. Because the intermetallic particles represent a small fraction of the total exposed surface area, the current density requirements will be limited as well.

Interesting is also the current-time behaviour of aluminium alloys exposed to CP. Gundersen and Nisancioglu [22] studied the current density requirements for different aluminium alloys over 1000 hours, and found a trend which is illustrated in Figure 2.7. First, an alkaline diffusion layer is formed close to the intermetallic particle due to oxygen reduction and hydrogen evolution (Figure 2.7 **(a)**). The oxide film becomes unstable as a result of alkalinization, and this leads to dissolution of the particle and corrosion of adjacent areas (Figure 2.7 **(b)**). This will increase the current density. Then, corrosion causes detachment of the particle, and a crevice is formed between the particle and the matrix. Finally, $Al(OH)_3$ and calcareous deposits are formed (Figure 2.7 **(c)**). This will reduce the cathodic and anodic reaction activities, and hence also the current density. An illustration of the current-time behaviour is given in Figure 2.8.

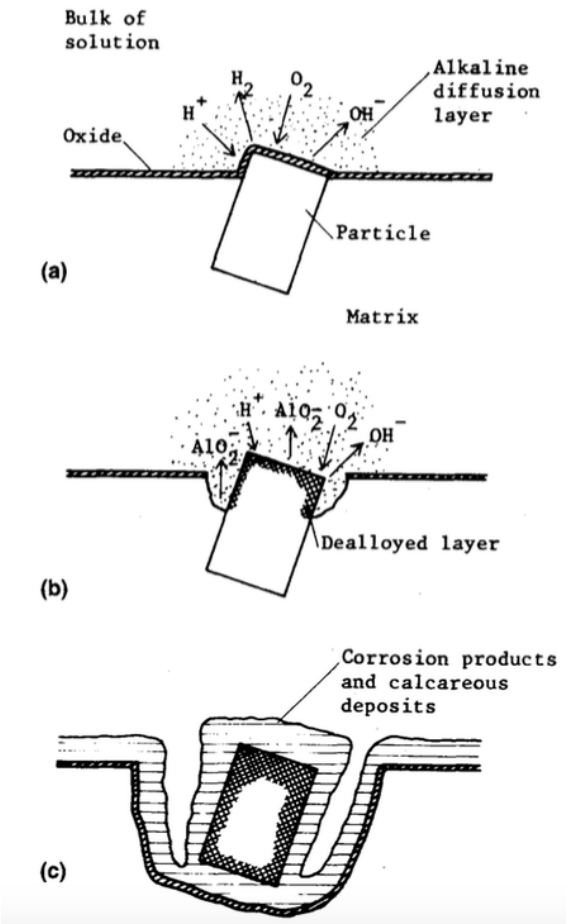

Figure 2.7: Illustration of the mechanism of cathodic protection (CP) of aluminium alloys in seawater: **(a)** formation of an alkaline diffusion layer, **(b)** dissolution of the particle and corrosion of adjacent areas, **(c)** detachment of the particle and eventually repassivation of the particle surface [22].

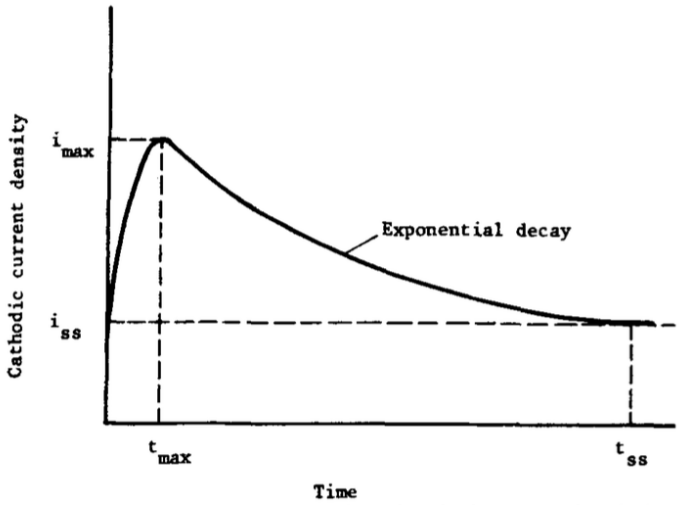

Figure 2.8: Illustration of the current-time behaviour during cathodic protection (CP) of aluminium alloys [22].

2.3.2 Hydrogen entry

The formation of atomic hydrogen in alkaline solutions was explained by electrolysis of water according to 2.4. Small amounts of the accessible hydrogen are able to enter the lattice, and the absorption reaction can be written according to Equation 2.8.

$$MH_{ads} \rightarrow MH_{abs} \tag{2.8}$$

There are several factors that may affect the accessible hydrogen and the subsequent rate of absorption into metals and alloys [23]:

- CP potential
- Surface temperature
- Water depth/hydrostatic pressure
- Surface conditions
- Load (stress/strain)
- Creep/plastic deformation
- Type of material/alloy
- Yield strength

Due to the large number of parameters, it is difficult to understand the local hydrogen concentration exactly.

2.3.3 Solubility and diffusivity of hydrogen

Hydrogen atoms are small and tend to enter interstitial sites in the lattice of aluminium. The solubility is strongly temperature dependent, and a decline from 10^{-6} atomic fraction (0.04 wppm) at the melting point to $1.5 \cdot 10^{-12}$ atomic fraction ($5.6 \cdot 10^{-8}$ wppm) at room temperature has been reported [24].

The closed-packed crystal structure of aluminium restricts the diffusivity of hydrogen, which is considerably lower than in bcc materials. Ishikawa and McLellan [25] studied the hydrogen diffusivity in an Al foil with 50 wppm metallic impurities, and found the Arrhenius relationship as given in Equation 2.9 for temperatures in the range of 285-328 K.

$$\mathrm{D}\ [\mathrm{cm}^2/\mathrm{s}] = 0.92 \cdot \exp\left(\frac{-55250\ \mathrm{J/mol}}{RT}\right) \tag{2.9}$$

D is the diffusivity of hydrogen in aluminium, R is the gas constant [J/mol K] and T is temperature in Kelvin. Equation 2.9 gives a hydrogen diffusion rate of approximately $1.90 \cdot 10^{-10}$ cm^2/s at room temperature (298 K). This is in accordance with what Ai et al. [26] found for AA 5083, where a diffusivity of 1.0-1.5 $\cdot 10^{-10}$ cm^2/s was reported. Table 2.6 shows hydrogen diffusion rates in different metals.

Table 2.6: Hydrogen diffusion rates in different metals [25, 27, 28].

Material	**Diffusivity [cm^2/s]**	**Temperature [K]**
AA 5083	$1.00\text{-}1.50 \cdot 10^{-10}$	298
Pure α-iron	$7.20 \cdot 10^{-5}$	298
Inconel-718	$1.42 \cdot 10^{-15}$	298
Low alloy steel (X65)	$1.00\text{-}2.00 \cdot 10^{-5}$	298
Duplex stainless steel (DSS)	$2.80\text{-}3.00 \cdot 10^{-11}$	295
Super duplex stainless steel (SDSS)	$1.10 \cdot 10^{-15}$	295

2.3.4 Hydrogen interactions with defects

Hydrogen solubility and diffusivity can be significantly altered by interactions between hydrogen atoms and lattice defects. Lattice defects such as dislocations, vacancies, precipitates and grain boundaries provide potential trapping sites for hydrogen [24], and the sites can be either reversible or irreversible [27]. Reversible trapping sites got a low hydrogen binding energy where hydrogen easily can be released by tempering. In contrast, irreversible trapping sites got a high hydrogen binding energy, where conventional tempering methods may not be sufficient for hydrogen to be released. Figure 2.9 shows potential trapping sites for hydrogen within the lattice of metals and alloys.

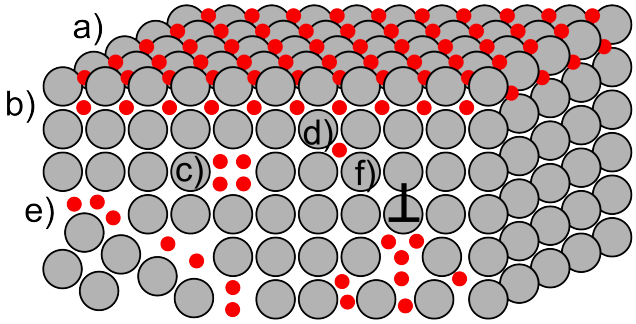

Figure 2.9: Illustration of potential trapping sites of hydrogen within the lattice of metals and alloys: **(a)** surfaces, **(b)** subsurfaces, **(c)** vacancies, **(d)** interstitial sites, **(e)** grain boundaries and **(f)** edge dislocations. Modified from [21].

Trapping reduces the amount of mobile hydrogen, and this makes transport of hydrogen more difficult. Ishikawa and McLellan [25] observed a further reduction in hydrogen mobility with increasing temperature. Because the equilibrium concentration of vacancies is around three orders of magnitude higher than the solubility of hydrogen in aluminium at the melting temperature [14], it is likely that vacancies can act as traps for hydrogen in aluminium. Trapping of hydrogen reduces the vacancy formation energy, and a significant increase in the equilibrium vacancy concentration have been observed (10^7 times for Fe) [29]. This will, in turn, provide more trapping sites for hydrogen and subsequently increase the hydrogen solubility. Other potential trapping sites include grain boundaries, where experiments have shown a decline in hydrogen solubility with increasing grain size [30]. This can be explained by preferred hydrogen diffusion to grain boundaries, which occurs to a lower extend when the grain boundary area is reduced.

2.4 Effect of hydrogen on the mechanical properties of aluminium

Considerable amount of literature confirm the significant effects of hydrogen on the mechanical properties of aluminium and aluminium alloys. Most studies are related to occurrence of hydrogen embrittlement (HE). HE will be further described in the following.

2.4.1 Hydrogen embrittlement

HE is an embrittlement mechanism caused by atomic hydrogen absorption into the lattice of a metal or an alloy [4, 24]. A complete understanding of how interactions between hydrogen and the surrounding matrix are causing embrittlement and subsequent failure is lacking, although several mechanisms have been proposed. Hydrogen enhanced decohesion (HEDE), hydrogen enhanced local plasticity (HELP) and brittle hydride formation are mechanisms often cited.

Hydrogen enhanced decohesion

HEDE was first proposed by Troiano in 1960 [14], and has been verified among a number of researchers since then. The mechanism is based on the fact that hydrogen tends to accumulate into areas of triaxial stress states where the microstructure is dilated. This causes a reduction in cohesive forces between the atoms, which again leads to embrittlement. Area of high stresses are typical related to an advancing crack, in which easily can propagate when the atomic cohesive strength is lowered. The region of damage is called the fracture process zone (FPZ) [21], and the FPZ is located just ahead of the crack tip. An illustration of the HEDE mechanism is given in Figure 2.10.

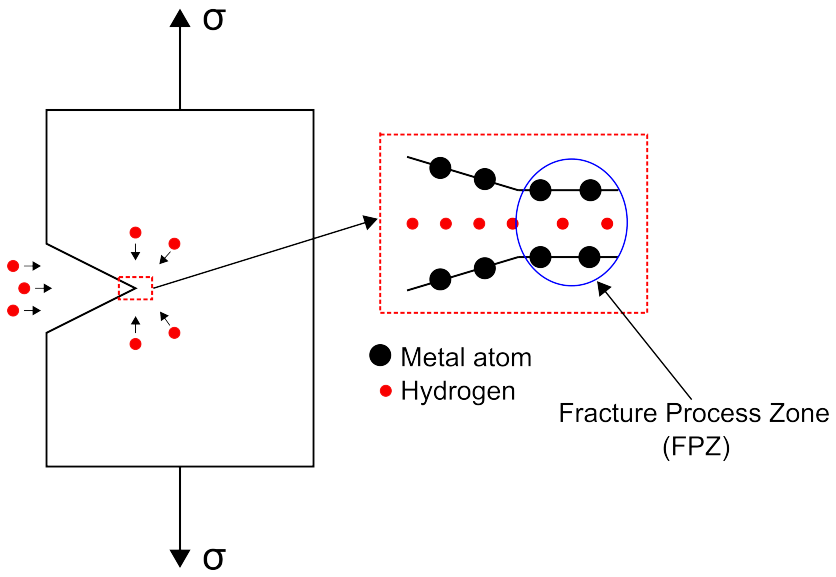

Figure 2.10: Illustration of the hydrogen enhanced decohesion (HEDE) mechanism. Hydrogen accumulates into areas of high stresses (*e.g* a crack tip), and this causes a reduction in cohesive forces between the atoms and eventually crack propagation. Based on ideas from [28].

Olden et al. [27] made an illustration of the FPZ showing how accumulation of hydrogen is related to the areas of high stresses. The illustration is based on studies of SDSS, and given in Figure 2.11.

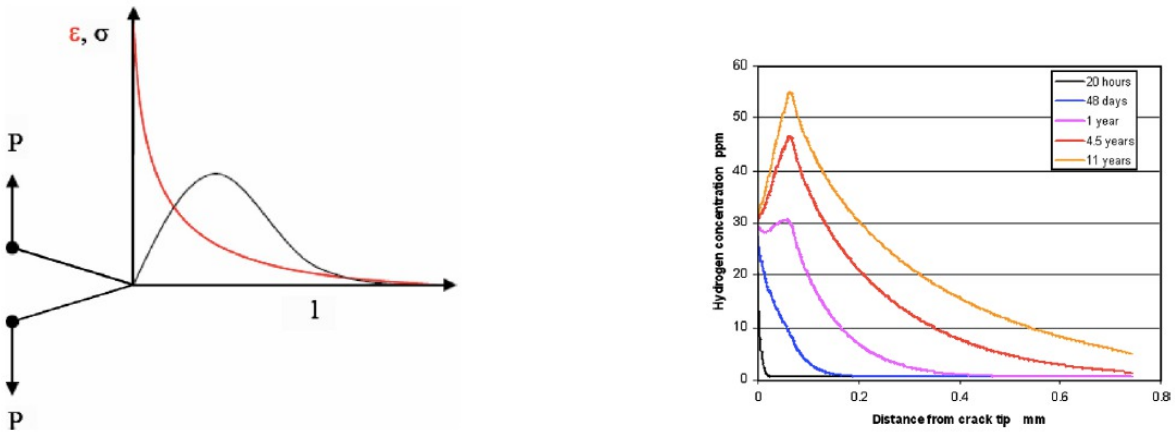

(a) **(b)**

Figure 2.11: Graphics from Olden et al. [27] showing **(a)** the stress and strain field ahead of a crack tip under mode I loading, and **(b)** the distribution of hydrogen ahead of a crack tip.

A slightly different HE mechanism is related to hydrogen's attraction to grain boundaries. Accumulation of hydrogen lowers the cohesive strength between adjacent grains, and this is hence rather an extension of what Troiano proposed [14].

Hydrogen enhanced local plasticity

The HELP mechanism proposes that hydrogen lowers the interactions between dislocations and other obstacles, resulting in increased dislocation mobility [21]. This occurs in regions close to crack tips, again because hydrogen tends to accumulate into areas of high stresses. The HELP mechanism has been confirmed by investigation of specimens during plastic deformation and hydrogen exposure done in TEM, where the number of dislocations in a pileup was observed to increase due to hydrogen. This gives rise to a localized region of increased plasticity, and microvoid coalescence may eventually result in a macroscopically brittle fracture [27]. An illustration of the HELP mechanism is given in Figure 2.12.

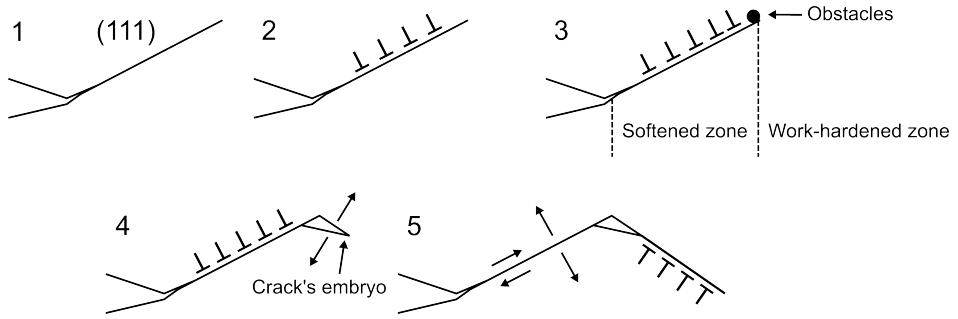

Figure 2.12: Illustration of the hydrogen enhanced local plasticity (HELP) mechanism. 1: activated slip plane in front of a crack tip, 2: increased dislocation mobility due to hydrogen, 3: pile up of dislocations, 4: microvoid formation, 5: crack propagation. Modified from [27].

Brittle hydride formation

Brittle hydride formation and cleavage has widely been studied, and this is believed to be the main embrittlement mechanism for the hydride forming elements such as V, Nb, Ti and Zr [21]. Hydrides are observed to nucleate in the stress fields of cracks, and growth occurs by further nucleation in stress fields caused by other hydrides. Scamans et al. (1987) [31] related hydride formation in aluminium alloys to grain boundary segregation of Mg. It was suggested that Mg segregation promotes increased reactivity and hydrogen absorption along grain boundaries, eventually leading to crack initiation and embrittlement. In overaged microstructures, the grain boundary precipitates facilitate hydrogen discharge rather than hydride formation. Another HE mechanism is related to hydrogen uptake during melting and heat treatment of aluminium alloys, known as blistering or irreversible hydrogen embrittlement [32]. The hydrogen solubility decreases during solidification, and this can lead to gas bubble formation from precipitation of molecular

hydrogen at inclusion-matrix interfaces. As a consequence, the ductility is permanently reduced. Blistering can easiest be avoided by reducing the hydrogen content.

Important to note from the preceding is that neither HEDE or HELP are confirmed mechanisms in HE of aluminium alloys. The mechanisms itself are debated because of the limited experimental evidence, which mainly are based on investigation of HE in steels. This will not be investigated into more details during this study.

2.4.2 Hydrogen embrittlement testing

Testing procedures

HE testing of aluminium alloys has often been conducted by use of cylindrical hydrogen pre-charged samples which have been tensile tested. Precharging is a method to promote hydrogen uptake into a material, and is commonly performed by cathodic polarization under potentiostatic conditions. Applied potential is typically -1500 mV_{SCE}, and HCl with pH 1 is an often used electrolyte. Precharging may last for various amount of time, where 6, 10 and 24 hours have been reported in the literature [5–10]. A precharging method known as the straining electrode test (SET) procedure has been utilized in certain HE studies [5–7]. The SET procedure is developed from theories about hydrogen transport by dislocations due to the low hydrogen diffusivity, and combines cathodic polarization with slow plastic straining ($1.0\text{-}3.0 \cdot 10^{-6}$ s^{-1}). Evidence is not confirmed, but results from experiments indicate an increased susceptibility to embrittlement for samples pre-charged by the SET procedure.

Hydrogen pre-charged samples and samples not being pre-charged are tensile tested according to standard tensile test procedures, and the tests are most often performed in air. There are also tensile tests designed to investigate the effect of CP on susceptibility to HE during testing. A stepwise loading tensile test has been developed by Johnsen et al. [23], where the samples are immersed in an electrolyte and exposed to cathodic polarization while simultaneously being tensile tested. The load is incrementally increased every hour until fracture occurs. Applied stress is monitored, and the stress under which fracture occurs is compared between hydrogen pre-charged samples, not pre-charged samples and reference samples tested in air.

Loss in reduction of area (RA_{loss}) is a frequently used measurement for reduction in ductility, and hence also a measurement on HE susceptibility. RA_{loss} is calculated from Equation

2.10, where RA_{air} is the reduction of area for reference samples tested in air, and $RA_{charged}$ is the reduction of area for hydrogen pre-charged samples tested with in situ cathodic polarization.

$$RA_{loss}[\%] = \frac{RA_{air} - RA_{charged}}{RA_{air}} \cdot 100 \tag{2.10}$$

The fracture surfaces are often examined by using scanning electron microscope (SEM), and the hydrogen concentration may eventually be measured in order to verify the results obtained. The hydrogen concentration can be measured by the use of an ion mass microprobe, where concentration is related to the hydrogen ion current/aluminium ion current-ratio, I_H^+ / I_{Al}^+ [33].

Aluminium may be subjected to cold creep during a stepwise loading tensile test, and load adjustments may hence be necessary to keep the load constant between each incremental increase. The creep behaviour of pure aluminium under high pressure and at low temperature (cold creep) has been investigated by Ishikawa et al. [34]. They found the creep rate to be stress dependent, and to increase by repeated loading. The creep resistance of Al-Mg (5xxx) alloys is generally high, although it depends on how the alloying elements are distributed [16]. Fine precipitates are observed to increase the creep resistance as well as a high Mg content. For Al-Mg-Si (6xxx) alloys, the resistance deteriorates with increased Si content [16]. The creep resistance of Al-Zn-Mg (7xxx) alloys is also low, and worst for the high-strength alloys.

Fractography

HE testing is often completed by fracture surface examination by using SEM, as it provide both high resolution and a good depth of view. The fracture surfaces may provide important information about the mechanical effects of hydrogen. By visual inspection, a brittle fracture is characterized by little or no necking, and the fracture surfaces do often appear bright and shiny. Higher magnification may either reveal intergranular fractures or transgranular fractures. In case of an intergranular fracture, the cracks propagate along grain boundaries creating facets. A transgranular fracture is often characterized by river patterns on flat faces, and these are formed when cracks propagate along certain crystallographic planes. These fractures are also known as cleavage fractures. Figure 2.13a shows an intergranular fracture in AA 5083 and Figure 2.13b shows a transgranular fracture in AA 7010.

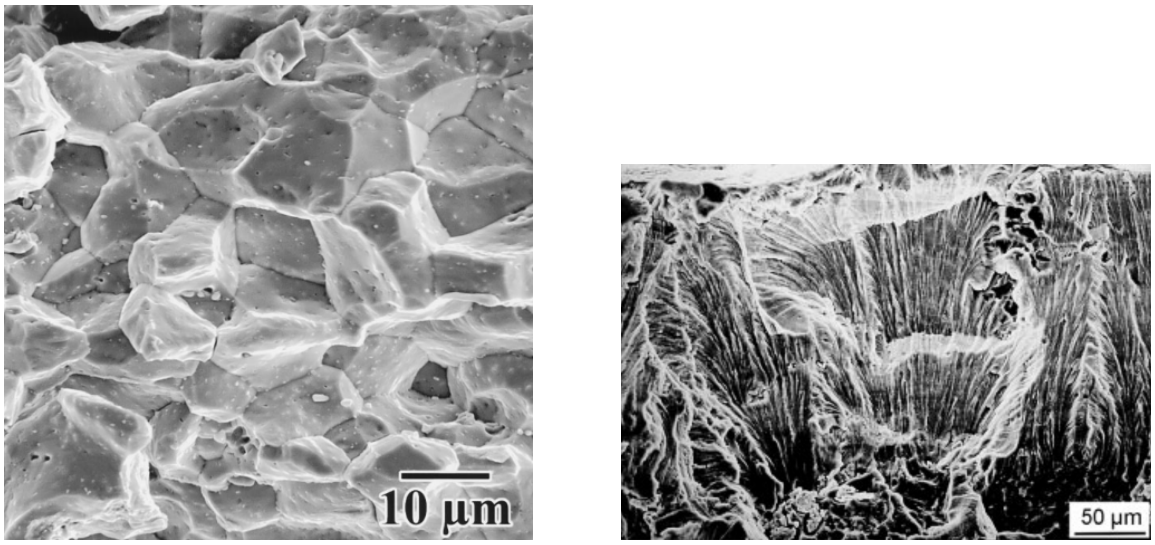

(a) **(b)**

Figure 2.13: SEM images showing **(a)** an intergranular fracture in AA 5083 and **(b)** a transgranular fracture in AA 7010 [35, 36].

A ductile fracture is recognized by matt and fibrous surfaces, often with a considerable amount of necking. The fracture can be either flat (90° to applied tensile stress), or shear (45° to applied tensile stress). Shear features are typically formed under plane stress conditions like for thin sections. Nucleation and growth of microvoids occurs as a result of particle-matrix decohesion or cracking of secondary particles, and their subsequent coalescence causes the ductile fractures. Microvoid coalescence creates characteristic dimples, which become visible at high magnification. Figure 2.14 shows a SEM image of a ductile fracture in AA 5083.

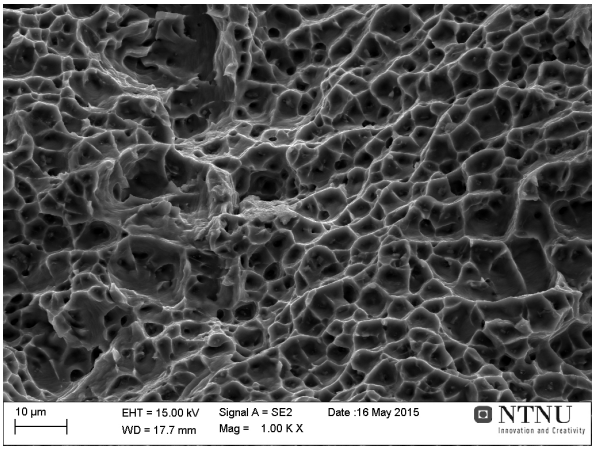

Figure 2.14: SEM image showing a typical ductile fracture characterized by dimples in AA 5083 (1000× magnification).

2.4.3 Examples from the literature

Effect of hydrogen on mechanical properties in 99.99 % pure aluminium has been investigated by Watson et al. [37]. The experiments revealed increased yield and tensile stresses and a decrease in strain-to-failure due to cathodic charging. Furthermore, microhardness tests revealed regions of increased hardness close to charged surfaces. Recombination poison, which facilitates hydrogen absorption, was used in a few experiments to ensure that the effects were caused by hydrogen. No differences in microhardness were found across these results, and the effect of cathodic charging was hence attributed to hydrogen absorption. By annealing, the recovery mechanism for a hardened region was compared with the recovery behaviour of a sample not being charged. For the hydrogen charged sample, a two-stage recovery at 300 °C and at 350 °C was observed, while the sample not being charged showed a single stage recovery at 300 °C. The first recovery stage was explained by loss of hardness, eventually being similar for the surface and the interior regions. Electron microscopy revealed an increased dislocation density due to charging, and the second recovery stage was hence likely connected to dislocation annihilation. From these results, it was accepted that the hardening in cathodically charged aluminium was caused by hydrogen and dislocations [24].

High-strength aluminium alloys have been subjected to a number of studies where effects of hydrogen on mechanical properties have been investigated [5–10]. The susceptibility to embrittlement is assessed from experiments where samples have been cathodically precharged with hydrogen and subsequently tensile tested. From the studies of HE in high-strength aluminium alloys [5–10], it is found that:

(1) Hydrogen has a pronounced effect on the mechanical properties in AA 2124, AA 7050 and AA 7075 alloys, as determined from a RA_{loss} between reference samples and hydrogen pre-charged samples, respectively.

(2) Susceptibility to HE is a function of temperature, microstructure and strain rate. At temperatures above -100°C, the greatest susceptibility is found for underaged microstructures. Only minor effects are found for overaged microstructures, while peak aged (T6 temper) microstructures show an intermediate susceptibility to embrittlement. Low-copper alloys have, however, showed embrittlement for all microstructures.

(3) The fractures are mainly transgranular independent of charging conditions, but regions of brittle intergranular fractures have been observed close to external surfaces. The characteristic discontinuous crack propagation due to time-dependent hydrogen diffusion appears as distinct striations on the fracture surfaces.

From the studies previously reviewed, there is no doubt that hydrogen has a pronounced effect on the mechanical properties of aluminium and aluminium alloys. However, the literature is confined to pure aluminium and alloys of high strength within the 2xxx and 7xxx series, and do not include studies of HE in seawater resistant alloys from the 5xxx and 6xxx series. It should also be noted that cathodic charging is performed at considerably lower potentials and pH values than what would be the case for CP of aluminium alloys exposed to seawater. As will be explained in the following, there are evidence indicating HE to be involved in stress corrosion cracking (SCC) of aluminium alloys. In that case, susceptibility to HE has been discussed also for other alloys than those being presented so far.

2.5 Stress corrosion cracking

SCC is defined as the combined action between stress and a corrosive environment in a susceptible material, eventually leading to fracture at stress levels well below the theoretical yield stress of the material [24]. It was first reported in aluminium alloys in 1923, and many efforts have since then been done to understand the phenomenon. SCC of aluminium alloys is mainly intergranular [35], however transgranular craking has also been reported [38]. Moreover, the crack propagation is time-dependent, and can result in brittle fractures of ductile materials [39]. High-strength wrought alloys and medium-strength weldable alloys are the major contributors to service failures due to SCC in aluminium alloys [40].

2.5.1 Mechanisms

Despite the fact that SCC of aluminium alloys is widely studied, there is no general agreement about the underlying mechanism to cause it [33,40–42]. Nevertheless, a literature review indicates anodic dissolution (AD) and hydrogen embrittlement (HE) to be the dominating mechanisms [24]. A third mechanism is related to rupture of the passive film along

grain boundaries, however only mentioned in a few studies [39, 40, 43]. A further description of AD and HE will be given in the following.

Anodic dissolution

AD is a dissolution mechanism where regions being anodic to the matrix cause potential differences which lead to localized corrosion. Initial corrosion sites include grain boundary precipitates, precipitate-free zones, solute depleted zones and zones of grain boundary segregation of copper [14, 35]. Breakdown of the protective oxide occurs as the anodic regions dissolve according to Equation 2.11 [41], and the oxide is further cracked by stresses (applied or residual).

$$\mathrm{M} \rightarrow \mathrm{M}^{n+} + n\mathrm{e}^{-} \tag{2.11}$$

Metal cations (M^{n+}) are then hydrolyzed to form hydroxydes as shown in Equation 2.12.

$$\mathrm{M}^{n+} + z\mathrm{H_2O} \rightarrow \mathrm{M(OH)}_z^{(n-z)+} + z\mathrm{H}^{+} \tag{2.12}$$

Furthermore, acidification promotes proton reduction according to Equation 2.13.

$$\mathrm{H}^{+} + \mathrm{e}^{-} \rightarrow \mathrm{H_{ads}} \tag{2.13}$$

Atomic hydrogen atoms may either recombine to form gaseous hydrogen, or get absorbed into the material as previously explained in Section 2.3.2. The latter forms the basis for the second of the two dominating mechanisms, HE.

Hydrogen embrittlement

A general assumption in hydrogen assisted SCC of aluminium alloys is that hydrogen is formed by a cathodic reaction (Equation 2.13), and that it enters the alloys via grain boundaries eventually to cause embrittlement [14]. The distinction between cracking as a clear consequence of HE, and SCC where hydrogen is involved appears somewhat arbitrary from the literature. It should be appreciated that CP is used to prevent corrosion, however with HE as a possible consequence due to hydrogen evolution. On the other side,

hydrogen assisted SCC involves hydrogen as provided from the corrosion reactions given in Equation 2.11-2.13.

2.5.2 Crack initiation and propagation

Measurements of SCC resistance on smooth tensile specimens have revealed a threshold stress intensity level K_{ISCC}, below which initiation of stress corrosion cracks will not occur under given conditions [40]. Important to note is that K_{ISCC} is not a material property; its value depends on other factors that affect SCC, such as type of material and environment. When the plastic zone ahead of a crack is small compared to the crack length, the stress intensity factor K is given by Equation 2.14, where σ is applied stress, a is the crack length and f is a geometrical factor [39].

$$K = \sigma\sqrt{a \cdot \pi} f \tag{2.14}$$

K_{ISCC} can be determined from a double cantilever beam (DCB) test, which is a method used to study stress corrosion crack propagation. A DCB specimen used for SCC testing of high-strength aluminium alloys is shown in Figure 2.15.

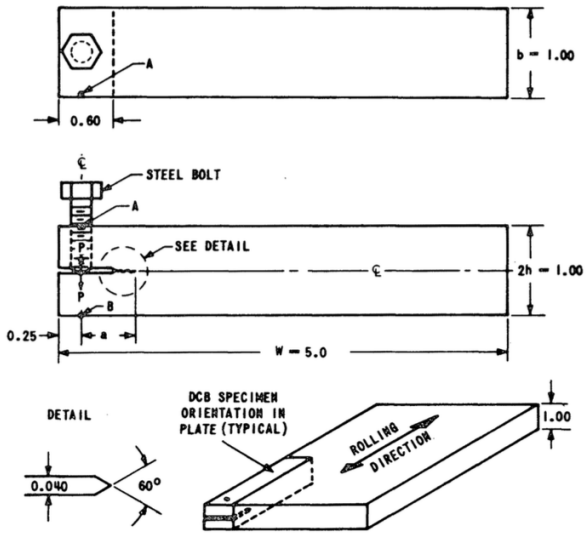

Figure 2.15: Double cantilever beam (DCB) specimen used for stress corrosion cracking (SCC) testing of high-strength aluminium alloys [44].

Data from DCB tests are presented as crack growth rate (v) as a function of K [14]. The v-K curves tend to exhibit a shape which is characteristic for aluminium alloys and also for other alloys: In the transition region from low to intermediate and high stress intensities, the crack growth rate goes from one being strongly stress dependent (Region I) to one being independent of stress intensity (Region II) [32]. Region II is also used to rank SCC resistance of aluminium alloys [35]. Figure 2.16 shows v-K curves for an Al-Zn-Mg (7xxx) alloy tested in a 3.5 wt% NaCl solution at different temperatures.

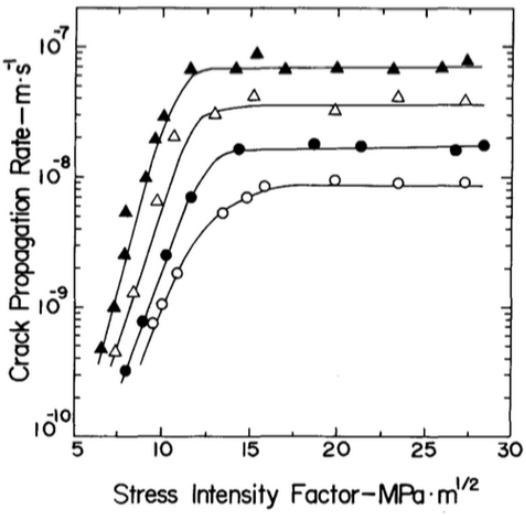

Figure 2.16: Stress corrosion crack propagation rate (v) vs applied stress intensity factor (K) for an Al-Zn-Mg (7xxx) alloy tested in a 3.5 wt% NaCl solution at 55 °C (black triangles), 45 °C (open triangles), 35 °C (black circles) and 25 °C (open circles) [42].

One disadvantage by the use of DCB tests is that they are very time consuming. For that reason, a dynamic testing procedure is often applied [39]. Further information about DCB testing can be found in the ASTM International standard ASTM E 399 [45].

Required tensile stress for SCC initiation is often below the yield strength, and may either be externally applied or residual. The latter is often introduced during heat treatment and quenching. Compressive stresses may on the other hand prevent crack initiation. Reported service problems due to SCC indicate that most stress corrosion cracks tend to initiate from surface stress raisers like notches, flaws, fatigue cracks or sites of localized corrosion [40]. For the same reason, pre-cracked specimens are more recently used in SCC testing of aluminium alloys. As previously mentioned, SCC failures can be both transgranular and intergranular, but intergranular cracking is most frequently observed [35]. Song et al. [33] revealed a decline in the fraction of intergranular fractures with increasing ageing time. Investigation done by Hardwick et al. (1982) [5] showed a connection between

the relative orientation of the stress axis and the grain structure on the fracture mode; when the tensile axis is parallel to the rolling direction, most of the grains will be parallel to tensile axis and intergranular crack propagation is hence unlikely.

2.5.3 Environmental effects

The importance of humidity on stress corrosion crack initiation in an Al-Zn-Mg (7xxx) alloy is shown in Figure 2.17, where stress corrosion crack velocity is plotted as a function of humidity. A significant acceleration in crack velocity is observed for increased humidity. Crack propagation is further intensified by the presence of halide ions such as Cl^-, Br^- and I^-, where Cl^- is most important because it is a natural part of marine environments [39]. Cl^- is hence an important component under SCC testing, and most experiments are performed in an aqueous 3.0-3.5 % NaCl solution [33, 36, 38, 41, 46]. Other important environmental factors include:

- The effect of temperature: Pathania [47] found decreasing stress corrosion crack initiation times with increasing temperatures.
- The effect of pH: The highest SCC susceptibility is found in neutral solutions [39].
- The effect of applied potential: SCC susceptibility can be significantly reduced by cathodic polarization [39].

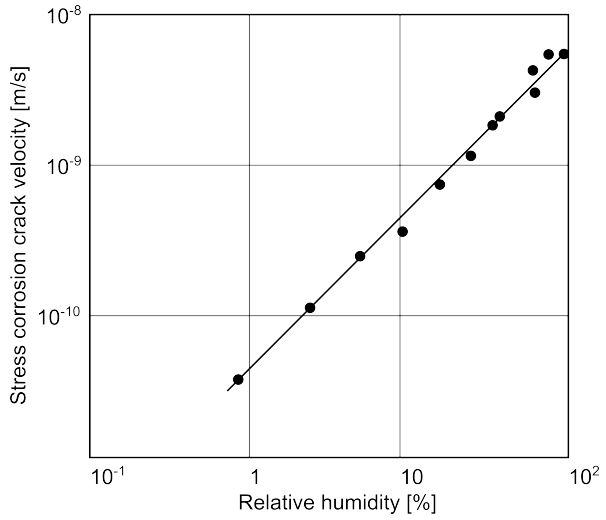

Figure 2.17: Effect of humidity on stress corrosion crack velocity in an Al-Zn-Mg (7xxx) alloy. A linear relationship is observed between the stress corrosion crack velocity and the humidity. Modified from [39].

2.5.4 Material parameters

The microstructure, of which composition and heat treatment are the most important factors, affects the susceptibility to SCC of aluminium alloys. High resistance to SCC is provided by either a precipitate-free microstructure, or a microstructure with equally distributed precipitates [39].

Effect of heat treatment

Precipitation hardening is a critical strengthening provider in heattreatable aluminium alloys, however with a strong effect on the susceptibility to SCC [40]. Al-Mg (5xxx) and Al-Zn-Mg (-Cu) (7xxx) alloys are generally considered to be immune to SCC in an as-quenched non-precipitated condition [31], but the resistance is significantly reduced by precipitation hardening until a minimum is reached before the peak strength. Further ageing (overageing) is beneficial for the SCC resistance, however at the expense of strength, as shown in Figure 2.18. Holroyd and Scamans [48] investigated crack growth rates for underaged tempers and overaged tempers of Al-Zn-Mg-Cu (7xxx) alloys, and they found the growth rates to be at least two orders of magnitude greater for the underaged tempers.

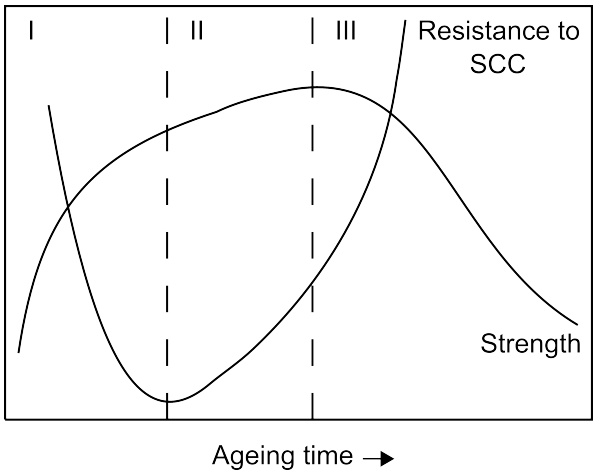

Figure 2.18: Changes in strength and stress corrosion cracking (SCC) resistance as a function of ageing. I: underaged, II: peak-aged, III: overaged. Modified from [40].

There is a general agreement about the beneficial effects of overageing on SCC resistance in aluminium alloys, and some of the theories that aim to explain these effects will be presented in the following.

Interactions between dislocations and precipitates provide strength by reducing the dislocation mobility. For small particles (*ex*. underaged conditions) this tends to occur by shearing. Shearing means that the moving dislocations shear through the particles. It is suggested that SCC susceptibility is enhanced by shearing, and that the degree of shearing depends on particle size, volume fraction and coherency stress field [14]. Further ageing (overageing) increases the particle size, and moving dislocations go from shearing the precipitates to bypassing the precipitates. As a result, loops are formed around the particles and this causes a change in slip mode from coarse slip to fine slip. This is believed to affect the susceptibility to SCC [6, 40].

It is also interesting to note how the beneficial effects of overageing have been explained by trapping of hydrogen during ageing. Puiggali et al. [49] suggested that the larger precipitates formed by overageing provide more trapping sites for hydrogen which consequently reduce the lattice concentration. As this would increase the time necessary to obtain a sufficient hydrogen concentration for crack initiation and propagation, resistance to SCC is increased. Song et al. [33] proposed that the observed reduction in hydrogen concentration with increased ageing time could be explained by the corresponding decline in excess vacancy concentration.

From the observed effects of overageing on SCC resistance, efforts have been made to achieve high SCC resistance materials without suffering from reduction in strength. An optimal combination between SCC resistance and strength has been obtained by a heat treatment known as retrogression and re-ageing (RRA). RRA of AA 7075 has shown to provide SCC resistance equivalent to the T73 (overaged) temper, while strength similar to the T6 (peak strength) temper is maintained [50]. This is achieved by holding a material in the T6 temper at a temperature of 200-280 °C for 5-6 seconds followed by re-ageing under the same conditions as used for the T6 temper. Investigators believe that the observed improvements can be attributed to changes in the grain boundary precipitate structure, however this is not fully understood [35].

Effect of alloy composition

Susceptibility to SCC is greatly affected by the presence of precipitates, which in turn depend on the alloy composition. Alloying elements are important strengthening providers in aluminium alloys, but unfortunately at the expense of SCC resistance which decreases with amount of alloying elements in supersaturated solid solution (SSSS). Alloys containing Cu, Mg and Zn are all susceptible [14], while minor additions of Cr, Mn, Zr, Ti, V, Ni and Li have shown beneficial effects on SCC resistance [40]. Addition of Cu to high-strength Al-Zn-Mg (7xxx) alloys is known to alter the precipitation kinetics by promoting bypassing of precipitates rather than shearing [6]. Previous work done by Sarkar et al. [51] indicated an improvement in SCC resistance by copper additions higher than 1 wt%.

2.5.5 Effect of grain orientation and stress direction

Aluminium alloys with highly directional grain structures are anisotropic regarding susceptibility to SCC [39]. This is typical for extrusions with an elongated pancake structure. The SCC resistance is lowest when applied stress is parallel to the short-transverse (S) direction, and highest when applied stress is parallel to the longitudinal (L) direction. An illustration of the different directions is given in Figure 2.19.

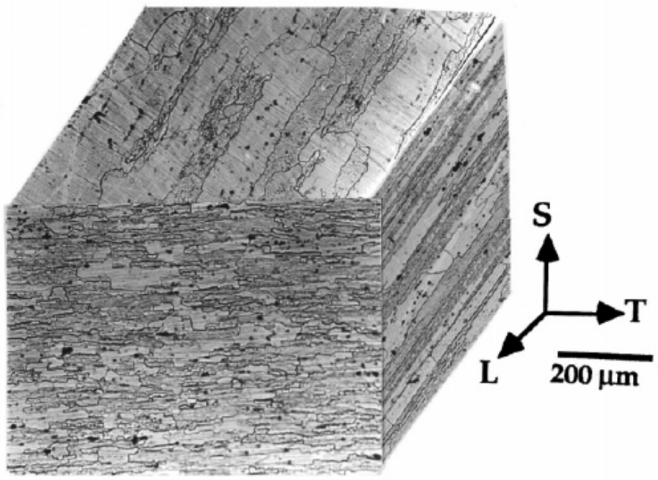

Figure 2.19: Grain structure in an AA 7075 aluminium alloy plate. **L**: Longitudinal direction (rolling direction), **T**: Transverse direction and **S**: Short-transverse direction [41].

2.6 Stress corrosion cracking testing

There are several test methods available for SCC testing of aluminium alloys. In order to achieve results in a short time, accelerated testing procedures are often used [39]. As stress corrosion cracks tend to initiate from surface stress raisers like notches, flaws, fatigue cracks and localized corrosion, pre-cracking of specimens is an appropriate way for accelerated SCC testing. The presence of a mechanically induced notch also creates a triaxial stress system which is beneficial for HE studies [39]. Typical tensile test methods include DCB testing (Section 2.5.2) and slow strain rate testing (SSRT). The samples are completely immersed in a corrosive environment during testing, where an aqueous 3.0-3.5 % NaCl solution often have been used [33, 36, 38, 41, 46].

2.6.1 Slow strain rate testing

SSRT is a commonly used method for SCC testing of aluminium alloys [33, 41, 49, 52]. Smooth or notched tensile specimens are strained at a constant rate, typically in the range of 10^{-8}-10^{-3} s^{-1} , until fracture occurs [35]. The major advantage of SSRT is the relatively short period of time necessary to determine SCC susceptibility. SSRT is, however, mainly confined to identification of aluminium alloys with high SCC susceptibility [39]. The factors used to determine SCC susceptibilty in SSRT include:

- Time-to-failure
- Percent elongation
- Reduction in yield/tensile strength
- Reduction in area
- Presence of secondary cracks
- Fracture surface appearances

A detailed description of SSRT can be found in the ASTM International standard ASTM G 129 [53].

2.7 Hydrogen embrittlement in stress corrosion cracking of aluminium alloys

2.7.1 Historical background

AD received great attention during the early years of research, and was more or less accepted as the dominating mechanism in SCC of aluminium alloys. There was especially one argument that contradicted a HE mechanism, namely the beneficial effects of cathodic polarization [32]. A mechanism driven on the presence of hydrogen was indeed believed to accelerate at more negative potentials, however the opposite was observed. This remained as the major argument against a HE mechanism in SCC of aluminium alloys until the early seventies, when Gest and Troiano [38] aimed to explain the unexpected observations by measurements of hydrogen permeability.

"Stress Corrosion and Hydrogen Embrittlement in an Aluminium Alloy" [38] is an acknowledged article published by Gest and Troiano in 1974. Gest and Troiano [38] managed to measure the hydrogen permeability through AA 7075 T651 aluminium membranes as a function of applied potential. From these results, an almost parallel behaviour has been found between hydrogen permeability and crack growth velocity when plotted vs. applied potential. Figure 2.20 shows hydrogen permeability curves (dotted lines) together with stress corrosion crack velocities, both reaching a minimum at intermediate potentials. The increased crack growth rates and hydrogen permeabilities at more negative potentials are expected from increased hydrogen evolution, and may also be understood by the case of cathodic pitting [40]. At high anodic potentials, increased crack growth rates and hydrogen permeabilities can be explained by increasing corrosion rates and acid hydrolysis of corrosion products [32].

Another argument against a HE mechanism was attributed to the negligible effect of pH variations on crack growth velocities, where studies showed that only pH values below 3 could enhance the crack growth rates [24]. Later research has, however, revealed an almost constant pH of 3.5 within cracks due to localized hydrolysis of aluminium ions, independent of the pH in the bulk solution.

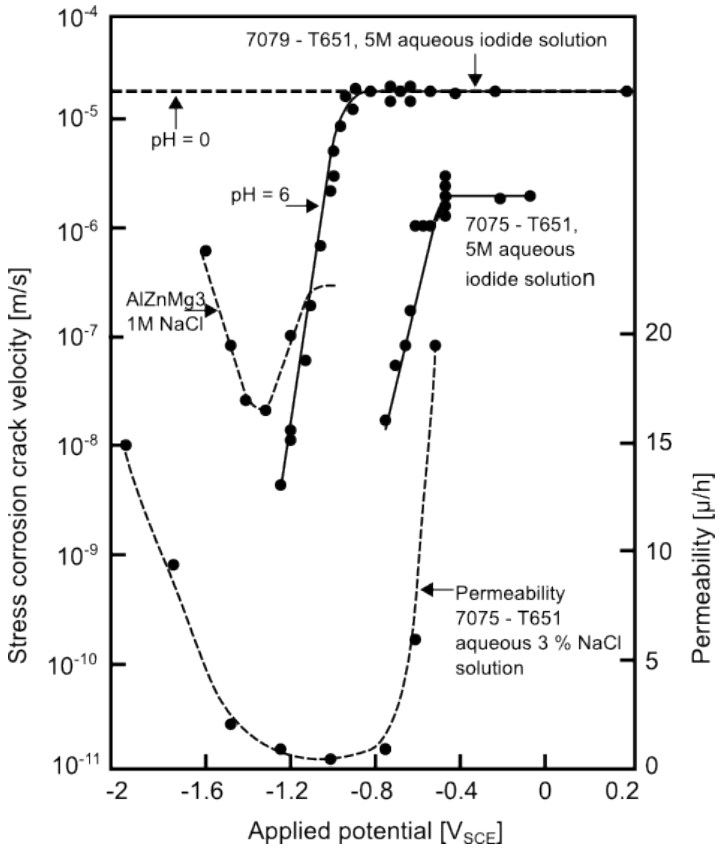

Figure 2.20: Effect of applied potential on hydrogen permeability (dotted lines) and stress corrosion crack velocity (solid lines) in different aluminium alloys. Modified from [32].

2.7.2 Experimental support of a hydrogen assisted mechanism

With two of the major arguments against the HE operating mechanism being disproved, extensive research has been devoted to studies concerning the role of hydrogen in SCC of aluminium alloys. A review of the experimental evidence supporting hydrogen assisted SCC of aluminium alloys will be given in the following.

One of the most convincing evidence supporting a HE mechanism in SCC of aluminium alloys was provided by Ratke and Gruhl [54] who showed that SCC initiation in an Al-Zn-Mg (7xxx) alloy occurred without any contact with an aqueous environment. A hollow tube with an external circumferential notch was filled with a corrosive solution, and loaded in tension. Fractographic investigation revealed crack initiation only in a region ahead of the external notch, with no connection to the corrosive environment. The explanation was attributed to hydrogen, likely generated through an electrochemical reaction

in the corrosive solution and absorbed into the alloy through the grain boundaries [14]. Similar considerations can be drawn from the effect of humidity on stress corrosion crack velocity as earlier shown in Figure 2.17. From the Kelvin equation [2], capillary condensation within cracks is not believed to occur at lower humidities than 30 %. This means that the crack tip is most likely not in contact with an aqueous environment for the lower humidities in Figure 2.17 [32]. Areas of bare aluminium close to the crack tip may, however, react with water to form hydrogen according to Equation 2.15. This leaves HE likely to be involved in SCC of aluminium alloys.

$$2\,Al^{3+} + 3\,H_2O \rightarrow Al_2O_3 + 6\,H^+ \tag{2.15}$$

Microscopic evidence supporting a hydrogen assisted cracking mechanism in SCC of Al-Zn-Mg (7xxx) alloys include observations of discontinuous cleavage-like fractures. The discontinuity is characterized by distinct crack arrest markings caused by time-dependent hydrogen diffusion. A SEM image showing distinct crack arrest markings in AA 7075 T7351 is given in Figure 2.21. Among others [50,56], Gest and Troiano [38] suggested a HE mechanism to be operating in SCC of aluminium alloys from their observations of discontinuous crack propagation in a 3 % NaCl environment. On the other hand, Zieliński [52] claimed that the discontinuous crack propagation was a result of time-dependent AD of grain boundary precipitates. This assertion is not further investigated in this study.

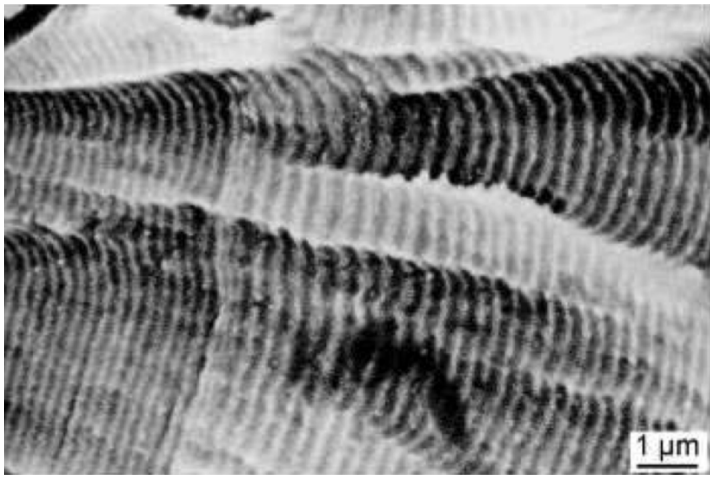

Figure 2.21: SEM image showing distinct crack arrest markings on the fracture surface of AA 7075 T7351 [35].

[2] The Kelvin equation relates the vapour pressure of a droplet with its radius [55], and can be used to determine whether condensation of a given specie within a capillary will occur or not.

A growing confidence for a HE operating SCC mechanism in Al-Mg (5xxx) alloys has been attached to the influence of loading conditions on SCC susceptibility in saline environments. Pickens et al. [57] studied how SCC susceptibility of an Al-Mg (5xxx) alloy, previously considered prone to embrittlement by proper heat treatment, changes from loading in tension (mode I) to loading in torsion (mode III). The loading modes are shown in Figure 2.22. Interesting is that only mode I creates a triaxial stress state, where accumulation of hydrogen can cause embrittlement according to the HEDE mechanism. Apparently, loading-mode testing could distinguish between AD and HE, with the former being unaffected by loading conditions [14]. Pickens et al. [57] found a significant reduction in crack velocity from mode I loading to mode III loading, and suggested HE to be the operating SCC mechanism in saline environments.

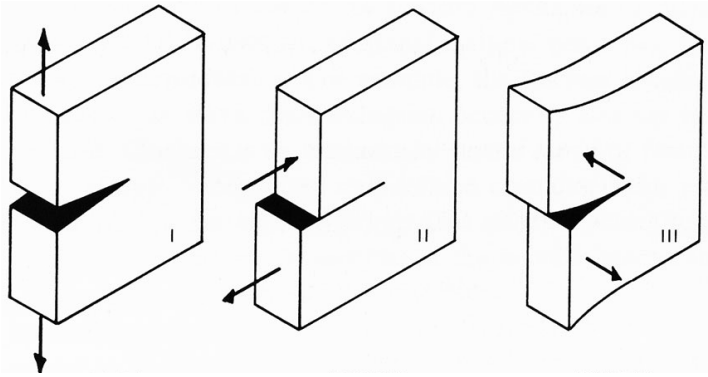

Figure 2.22: The three modes of loading; I: loading in tension, II: loading in shear, III: loading in torsion. Modified from [58].

Observations of hydrogen bubble formation in an Al-Zn-Mg (7xxx) alloy exposed to water at elevated temperatures were done by Christodoulou and Flower [59]. Unprotected samples, together with encapsulated samples (protected from the water vapour), were placed in an autoclave above distilled water. The pressure was increased to 2.06 bars, and the temperature was kept at 120 °C where both ageing and embrittlement occur simultaneously. Embrittlement was measured by ductility when the samples were strained. The results are presented in Figure 2.23 for both dry samples (filled circles) and exposed samples (open circles). For the exposed samples, recovery of ductility is observed after about 24h of exposure between stage 2 (blue circle) and stage 3 (red circle). At the same time, hydrogen bubble formation on η-phase ($MgZn_2$) precipitates was observed SEM images. Christodoulou and Flower [59] claimed that there was no way in which recovery of ductility could be explained in terms of an AD mechanism, and concluded that the most reasonable explanation involves a HE mechanism. As hydrogen bubbles previously are indicated to be less damaging than hydrogen in solution [60], recovery of ductility can

be understood from a reduced grain boundary concentration of hydrogen in solution as bubble formation commences.

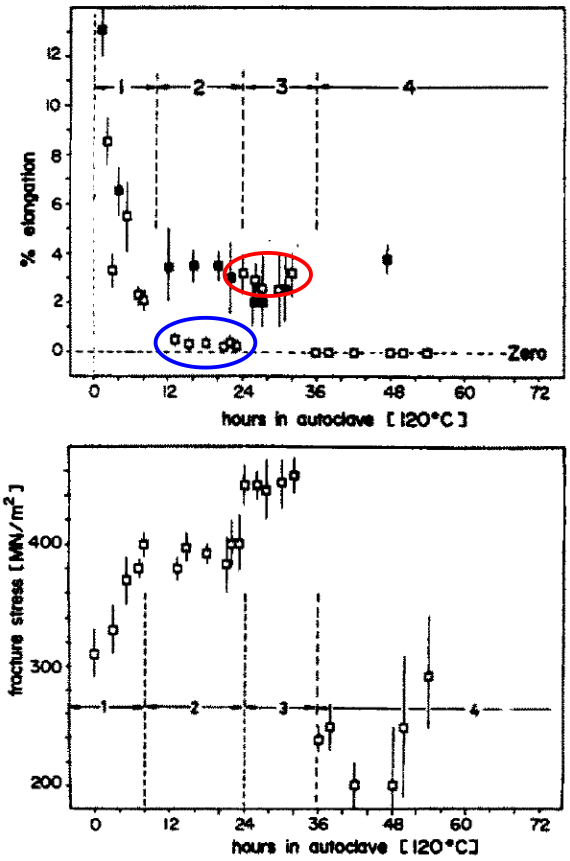

Figure 2.23: Results from embrittlement testing of an Al-Zn-Mg (7xxx) alloy for samples exposed to water vapour (open circles) and dry samples (filled circles). The upper diagram shows the variation in ductility as a function of exposure time and the lower diagram shows the variation in fracture stress as a function of exposure time. Recovery of ductility is observed between stage 2 (blue circle) and stage 3 (red circle). Modified from [59].

Further support for hydrogen assisted SCC of Al-Zn-Mg (7xxx) alloys have been provided from pre-exposure experiments performed by Scamans et al. (1975) [61]. Specimens were pre-exposed to water vapour saturated air (WVSA) and subsequently tensile tested in either air or vacuum. The results showed brittle intergranular failures, apparently due to deep intergranular penetration of hydrogen. Hydrogen was presumed to be formed during precharging from the reaction between water vapour and aluminium ions as previously shown in Equation 2.15. Moreover, recovery of ductility when stressed under vacuum was associated with hydrogen evolution. These findings indeed indicate hydrogen to be involved in the embrittlement mechanism.

Pre-exposure to WVSA with subsequent tensile testing in air is not a conventional SCC test, but rather a test on HE. However, HE testing has been very important for understanding the role of hydrogen in SCC. Experiments have shown a number of similarities between the mechanical behaviour of HE tested samples and samples tested under SCC conditions [14]. The greatest susceptibility to both HE and SCC is found for underaged microstructures [5–7, 9, 62, 63]. There is also a similarity in the v-K relationship [14]. Furthermore, both HE and SCC are observed to be reversible [14], and a discontinuous crack propagation is also observed for both [32].

The effect of cathodic polarization either prior to (precharging) or during SCC testing has also been studied [33, 38, 41]. Again, most studies involve testing at potentials more negative than what is normally provided from CP systems. Gest and Troiano [38] compared displacement to failure for DCB test specimens exposed to cathodic charging (from -1500mV$_{SCE}$ to -1700 mV$_{SCE}$) in a 3 % NaCl solution. A selection of samples were subjected to an outgassing treatment in the atmosphere for 7 days, and those showed a significant increase in displacement to failure compared to samples being kept under cathodic polarization. These results were related to a reversible loss in ductility due to hydrogen, and were confirmed by a reduction in the lattice parameter back to its original value during outgassing.

It is important to note that most of the aforementioned experiments have been performed on high-strength aluminium alloys within the 7xxx series. Because of the great variations in composition, microstructure and heat treatment procedures among the different alloys, the role of hydrogen in SCC may also be completely different. Even with all the experimental evidence indicating hydrogen to be involved in SCC of aluminium alloys, doubts still exist regarding the operating mechanism(s). Many investigators emphasize that it is just as easy to find an argument supporting an AD mechanism as it is for a HE mechanism [24]. Proposed SCC mechanisms for the aluminium alloys series investigated in this study will be given in the following, with the main focus on studies were a hydrogen assisted SCC mechanism have been suggested.

2.8 SCC of Al-Mg (5xxx), Al-Mg-Si (6xxx) and Al-Zn-Mg (7xxx) alloys

2.8.1 Al-Mg (5xxx) alloys

Magnesium is a very important strengthening provider in Al-Mg (5xxx) alloys (Section 2.1.2), and from strengthening considerations it appears convenient to develop Al-Mg (5xxx) alloys with higher strength by increasing the magnesium content. However, this ability has been restricted due to observations of SCC issues for alloys exceeding a magnesium content of 3.5 wt% [64]. These issues are associated with grain boundary precipitation of a β-phase (Al_3Mg_2) due to thermal exposure (also known as sensitization), which can be further enhanced by cold working [35]. Different procedures for β-phase precipitation have been found from sensitization studies of Al-Mg (5xxx) alloys. Pickens et al. [57] observed a semicontinuous β-layer in AA 5083 H131 by exposure at 150 °C for 72 h. Investigation of the same alloy performed by Goswami et al. [65] revealed β-phase precipitation along grain boundaries and on pre-existing manganese-rich particles by annealing at 175 °C for 10 days. Jones et al. (2004) [66] ascertained β-phase precipitation in AA 5083 H321 after 1 h of ageing at 175 °C.

Searles et al. [46] observed that the most severe conditions for SCC susceptibility were related to formation of a continuous grain boundary β-film, and that the ductility recovered with further heat treatment due to weakening of the continuous film. It is widely accepted that the β-phase is anodic to the matrix [36, 66, 67], and this strongly suggest that SCC of sensitized Al-Mg (5xxx) alloys occurs via AD of the β-phase while it cathodically protect the surrounding Al. However, what also has been observed is accelerated SCC in materials where the β-phase is discrete along grain boundaries and not continuous [36]. This has led to a discussion about the mechanism that causes crack propagation between particles. A study from Jones et al. (2001) [36] on sensitized AA 5083 H321 showed an open circuit potential (OCP) difference of over 0.4 V between the Al and the β-phase, from which a rapid corrosion of β-particles is expected. The question is whether these β-particles are completely dissolved before active corrosion of the β-free grain boundary areas occur. If the cracking mechanism is hydrogen assisted, a complete dissolution would not be necessary for crack propagation to commence. Jones et al. (2001) [36] claimed that both AD and HE could be justified as operating SCC mechanisms in AA 5083, and that even a combination of them may be suggested. The latter has also been suggested by Ai et al. [26], who

studied the hydrogen diffusion in AA 5083 H131 as a function of orientation and degree of sensitization. An AD mechanism alone was not supported because of the observed crack growth rates that would require unlikely high anodic current densities (20 A/cm^2). It was hypothesized that regions of AA 5083 solid solution between β-particles could be embrittled by hydrogen from the anodic dissolution mechanism, if the hydrogen diffusion rates were high enough for hydrogen to be present ahead of the β-phase dissolution. The hydrogen diffusion rates found by Ai et al. [26] support a combined AD-HE mechanism in SCC of Al-Mg (5xxx) alloys.

From the work done by Jones et al. (2001) [36], the following observations support a hydrogen assisted cracking mechanism:

(1) Cathodic potentials up to -1390 mV$_{SCE}$ proved to have no effect on the crack propagation rate. This was understood by a stable Al oxide film at cathodic potentials acting as a barrier to hydrogen uptake. In contrast, anodic potentials showed increased crack velocities. This was explained by an unstable oxide film, which promoted hydrogen uptake. These results are in accordance of what Gest and Troiano [38] observed with increased hydrogen permeability when applying potentials anodic to the OCP relative to cathodic potentials.

(2) A large hydrogen reduction rate ($1.4 \cdot 10^{-3}$ A/cm^2) was observed under corrosion of the β-phase.

2.8.2 Al-Mg-Si (6xxx) alloys

It is evident from the literature that limited information about both HE and SCC of Al-Mg-Si (6xxx) alloys exists, and service problems from these alloys have not been reported [35]. However, susceptibility to SCC may be promoted by inappropriate heat treatment associated with grain boundary precipitation. SCC have also been observed under laboratory experiments on Al-Mg-Si (6xxx) alloys containing more than about 1 wt% copper [39].

2.8.3 Al-Zn-Mg (7xxx) alloys

Copper additions may increase the strength of Al-Zn-Mg (7xxx) alloys considerably, but exploitation of their maximum strength has been restricted due to SCC susceptibility. In fact, SCC is assumed to be the major concern in technical applications of Al-Zn-Mg (7xxx) alloys [14]. SCC of Al-Zn-Mg (7xxx) alloys has been a topic for many studies, and hydrogen is certainly involved in SCC of these alloys based on the experimental evidence presented in Section 2.7.2.

It is of interest to note that a combined HE and AD mechanism has been suggested also for Al-Zn-Mg (7xxx) alloys. Najjar et al. [41] investigated SCC in AA 7050 of various tempers, and showed that an initiation period associated with formation of critical defects was necessary before HE characteristics appeared. Macroscopically, this was represented by a significant reduction in elongation to failure. Fractographic examination by use of SEM revealed regions of extensive metal consumption close to the surface, and these regions were followed by deeper areas of brittle cleavage-like fractures. Interestingly is that when the OCP was changed to an applied cathodic potential E_c = -1100 mV_{SCE} at 0.8 % strain, a significant reduction of elongation to failure was observed, even for overaged tempers. In contrast, comparable tests performed at OCP, E_c and in air showed negligible effects on reduction of elongation to failure. From the fractographic examination results as well as the macroscopic observations, it seems likely that critical defects are formed by AD at OCP, while crack propagation due to HE occurs at an applied cathodic potential, E_c. On the other hand, examination of pre-cracked specimens revealed only cleavage-like crack propagation. This study has shown that the formation of critical defects plays a major role in hydrogen uptake and subsequent embrittlement, whether they are caused by AD or by mechanical pre-craking. For studies of HE, it may thus be appropriate to use pre-cracked specimens.

A broad understanding regarding HE in aluminium alloys has been established from the literature review performed in this study. Moreover, the extensive investigation about hydrogen's role in SCC of aluminium alloys has gained information about how HE is related to SCC. Based on the available literature, it is understood that HE in SCC involves hydrogen as provided from a corrosion reaction. In contrast, cathodic polarization is used to prevent corrosion, and hence SCC. However, cathodic polarization entails hydrogen evolution in which may promote HE. As this study aims to investigate the effect of hydrogen as provided from cathodic polarization, there will be a less focus on HE related to SCC in the remaining part.

Chapter 3

Experimental procedure

3.1 Materials

In this study susceptibility to HE in Al-Mg (5xxx) alloys, Al-Mg-Si (6xxx) alloys and Al-Zn-Mg (7xxx) alloys was investigated. The alloys were provided from Hydro, and their chemical compositions are given in Table 3.1.

Table 3.1: Chemical composition of the alloys investigated in this study, given in wt% [68, 69].

	Si	**Fe**	**Cu**	**Mn**	**Mg**	**Cr**	**Zn**	**Ti**	**Zr**
5083B	0.15	0.30	0.021	0.61	4.38	0.11	0.018	0.019	-
6082B	0.93	0.18	0.008	0.55	0.60	0.011	0.002	0.011	-
6082C	1.00	0.19	0.20	0.53	0.66	-	-	-	-
6082Z	1.00	0.19	-	0.53	0.66	-	0.20	-	-
7108B	0.099	0.132	0.031	0.005	0.870	0.001	5.77	0.012	0.164

3.1.1 Development of alloy variants

The alloys had been subjected to a different number of processing steps when they were received from the supplier. Furthermore, several alloy variants were developed from the as-received alloys. A description of the different alloy variants together with the processing steps performed will be given in the following.

5083B, 6082B

Alloys of EN AW 5083 H321 and EN AW 6082 T6, received in extruded plates with a thickness of 20 mm and 10 mm, respectively.

5083BW

Alloy of EN AW 5083 H321. Two plates with a thickness of 20 mm had been welded together with a full penetration weld by using metal inert gas (MIG) welding. The welding consumable used was AA 5183.

5083BHT

Sensitized EN AW 5083 H321, 5083BHT, was developed with the purpose to investigate β-phase formation on the susceptibility to SCC. Sensitization was performed by a 72 hours hold at 150 °C, and finished by water quenching. This procedure was chosen based on work done by Pickens et al. [57], as previously discussed in Section 2.8.1. The sensitized microstructure was analyzed by using a JEOL JXA-8500F electron probe micro analyzer (EPMA), and this was done by Morten Peder Raanes at the Department of Materials Science and Engineering (DMSE).

6082C and 6082Z

Alloys with different chemical composition from the EN AW 6082 T6 base material (6082B) (see Table 3.1). The alloys were received in billets, and extruded into plates of 3 mm thickness at SINTEF Materials and Chemistry. The extruded profiles were then artificially aged by a 5 h hold at 185 °C followed by water quenching.

7108B

Alloy of AA 7108.50, received in an extruded profile with a thickness of 3 mm. First, the profile was solution heat treated at 480 °C for 15 minutes and quenched in water. After being kept one hour in room temperature (RT), the profile was artificially aged to T6 temper. This was done by first increasing the temperature from RT - 100 °C over 30 minutes. A 5 hours hold at 100 °C was followed by a 6 hours hold at 150 °C, and the profile was then quenched in water.

3.2 Tensile testing

Mechanical properties from the materials were required for HE testing, and a standard tensile test procedure was performed to determine values of yield strength ($R_{p0.2}$) and tensile strength (R_m). Only a few alloy variants were tensile tested, and those were 5083BHT, 6082C and 6082Z. Mechanical properties for 5083B, 5083BW, 6082B and 7108B were provided from the supplier. The tensile tests were conducted at the DMSE, with assistance

from Pål Christian Skaret. Further information about the specimen specifications can be found in Appendix A.

3.3 Hydrogen embrittlement testing

HE testing was conducted according to the stepwise loading tensile test procedure as previously reviewed in Section 2.4.2. This procedure has been qualified for 13 % Cr supermartensitic stainless steel (SMSS) and 22 % / 25 % Cr duplex stainless steel (DSS) under CP in seawater, and was assumed to be applicable for aluminium alloys as well. A similar method used to determine the threshold stress for onset of HE in steel is described in the ASTM International standard ASTM F1624-12 [70]. The purpose of the stepwise loading tensile test is to determine the stress under which fracture occurs for (1) hydrogen precharged samples and (2) not pre-charged tensile tested with in situ cathodic polarization, and (3) for reference samples tensile tested in air.

3.3.1 Sample preparation

Samples for tensile testing were machined by NOMEK AS and by staff at the Department of Engineering Design and Materials, according to the dimensions given in Figure 3.1. All samples were pre-cracked by introducing a 2 mm deep notch (yellow line). The tensile axis was made parallel to the longitudinal (L) direction for all samples except for the welded profile, 5083BW, which due to its longitudinal weld got the tensile axis parallel to the transverse (T) direction.

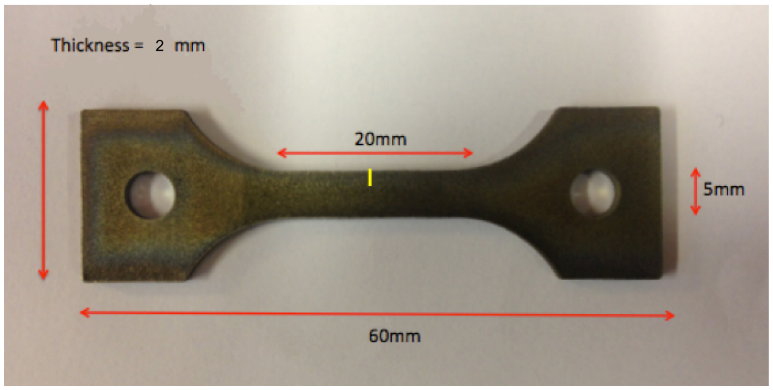

Figure 3.1: Dimensions of the tensile test samples. The 2 mm deep notch is indicated by the yellow line.

Grinding by use of gradually finer SiC paper was done to remove surface contamination and to achieve uniform surfaces. The samples were then polished by use of 3 μm and 1 μm diamond suspensions in order to obtain a smooth surface finish. Soap water and ethanol were used in between each step for cleaning purposes. An image showing a sample before and after grinding and polishing is given in Figure 3.2.

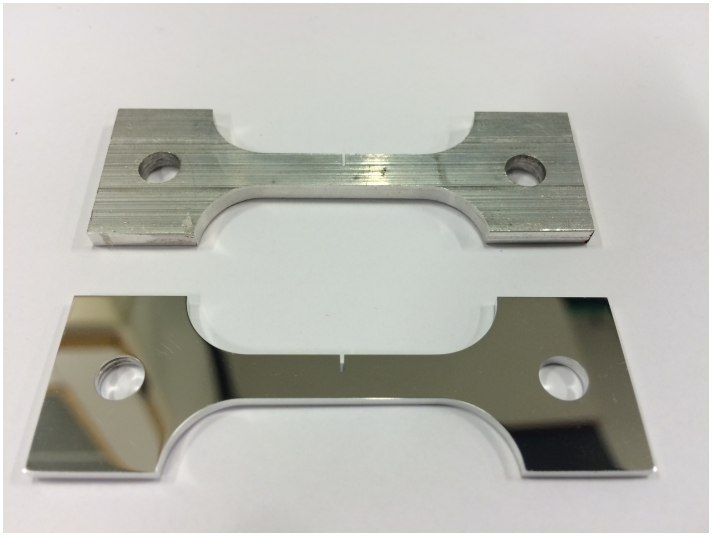

Figure 3.2: Image showing a sample before and after grinding and polishing.

3.3.2 Tensile test equipment

The tensile test equipment used were two ME-Meßsysteme GmbH load cells, each with a capasity equal to 1 Ton equivalent load. These were mounted to a desk by use of vices, and load was applied by hand using a wrench. Data was recorded by a connected computer with customized software. The test equipment used for tensile testing of samples in air is shown in Figure 3.3. Tensile testing with in situ cathodic polarization was performed by placing the samples in between a two-part electrolyte chamber as shown in Figure 3.4. The chamber was made of poly carbonate, and equipped with a glass window in front in order for images to be taken. Images were taken by the use of a Edmund Optics^{TM} color camera mounted to a Mitutoyo^{TM} video microscope. The microscope was equipped with a Mitutoyo^{TM} objective providing 16× magnification. An overview image of the experimental setup used for tensile testing with in situ cathodic polarization is given in Figure 3.5.

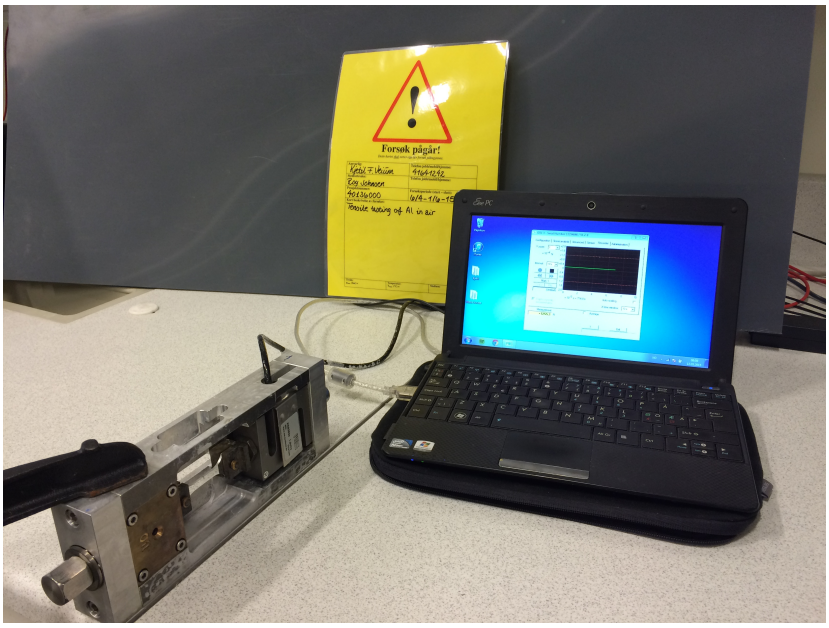

Figure 3.3: Experimental setup used for tensile testing of samples in air.

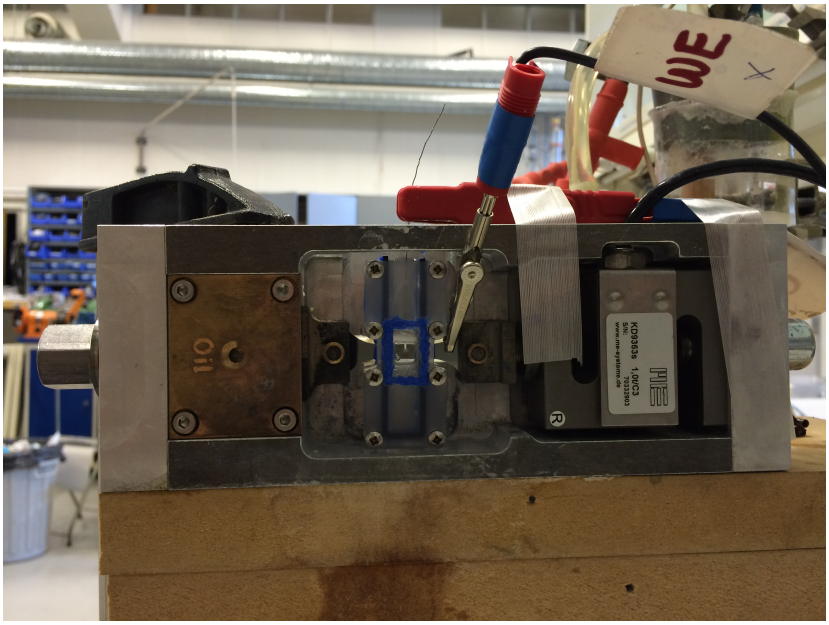

Figure 3.4: Image showing a load cell with a sample mounted in between a two-part electrolyte chamber.

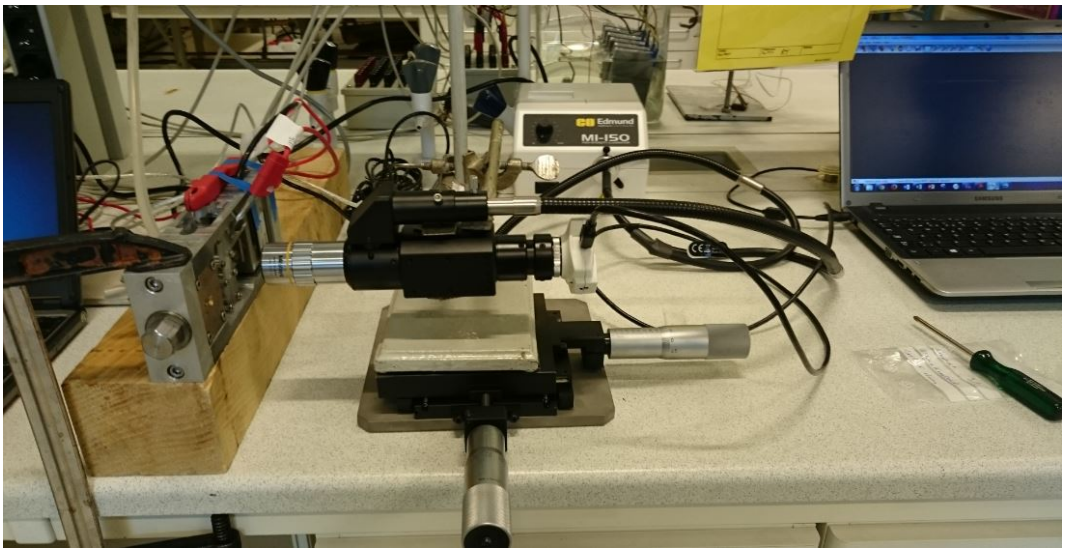

Figure 3.5: Experimental setup used for tensile testing with in situ cathodic polarization.

3.3.3 Tensile test procedure

Initial applied load was determined by the $R_{p0.2}/R_m$-ratio, and varied between the different alloy variants. The proper load expressed in newton (N) was calculated from Equation 3.1, where F is the load and A is the cross sectional area. A Leica^{TM} MEF4M optical microscope was to obtain an accurate value of the sample height at the notch, and the width was measured by using a Mitutoyo^{TM} caliper.

$$F\,[\mathrm{N}] = F\,[\mathrm{MPa}] \cdot A\,[\mathrm{mm}^2] \tag{3.1}$$

Load was increased by 4 % of $R_{p0.2}$ every hour until fracture occurred. An attempt was made to use an initial load such as each tensile test lasted for about 9 hours. As the alloys were subjected to cold creep, load adjustments were done in order to keep the load constant between each incremental increase. Pictures were taken after each incremental increase. The electrolyte used was a 3.5 % NaCl solution, and in situ cathodic polarization was performed under potensiostatic conditions with an applied potential of -1093 mV_{SCE}. This potential corresponds to -1050 $mV_{Ag/AgCl}$, which is the expected protection potential provided from CP systems. One of the samples was, however, polarized to -1500 mV_{SCE}. The exposed surface area was approximately 1.05 cm^2 for all samples. Applied potential was supplied from a Gamry^{TM} potentiostat, and the potential was measured against a saturated calomel reference electrode (SCE). A platinum wire was used as counter electrode,

and both potential and current were monitored while the experiments were running.

3.3.4 Precharging

A selection of samples was hydrogen pre-charged prior to tensile testing. Precharging was performed to promote hydrogen uptake into the materials, which also can simulate the effect of CP after several years in service. The samples were submerged in a beaker filled with a 3.5 % NaCl solution and cathodically charged under potentiostatic conditions with an applied potential of -1093 mV_{SCE}. A platinum wire was used as a counter electrode, and applied potential was supplied by a Bank Elektronik^{TM} potentiostat and measured against a SCE. An image of the experimental setup is given in Figure 3.6. The temperature was kept at 80 °C in order to increase the hydrogen diffusion rate, and precharging was conducted over six days to ensure adequate hydrogen uptake. The samples were stored in a freezer until testing to avoid hydrogen outgassing. Figure 3.7 shows an image of hydrogen pre-charged samples.

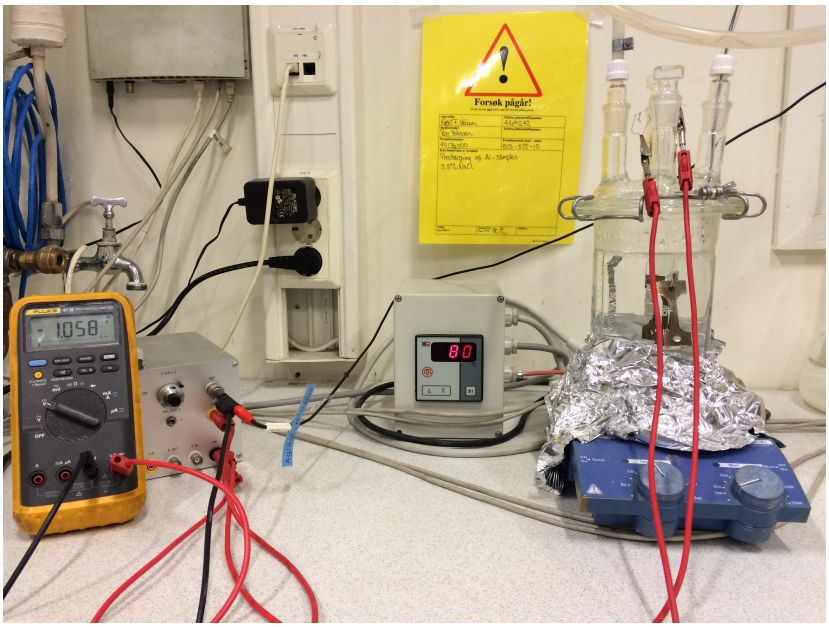

Figure 3.6: Experimental setup for precharging of samples.

Figure 3.7: Image showing hydrogen pre-charged samples.

3.3.5 Test matrix

Six samples from each of the seven alloy variants were subjected to the stepwise loading tensile test. From the six samples, two were tested with in situ cathodic polarization (not pre-charged samples) and two were hydrogen pre-charged prior to tensile testing with in situ cathodic polarization (pre-charged samples). These samples were tested at an applied potential of -1093 mV_{SCE}. Additionally, one not pre-charged samples from 7108B, 7108BLP, was tested at an applied potential of -1500 mV_{SCE}. The last two samples were tested in air (reference samples). A designation system was made similar for all samples, and is for 7108B shown in Table 3.2.

Table 3.2: Description of the designation system used for all samples, explained by the AA 7108.50 base material, 7108B.

Sample	Description
7108B1	Not pre-charged sample 1
7108B2	Not pre-charged sample 2
7108BH1	Pre-charged sample 1
7108BH2	Pre-charged sample 2
7108BA1	Reference sample 1
7108BA2	Reference sample 2
7108BLP*	Not pre-charged sample

*This sample was only included for 7108B

3.4 Fracture surface examination

Fracture surfaces from all samples were examined by use of a Zeiss Supra LVFESEM. A secondary electron detector was used to achieve topography contrast, and the SEM was operated with an accelerating voltage of 15-20 kV. The working distance varied within the range of 10-23 mm, and the aperture used was 30 μm.

The aim of the fractographic investigation was to characterize the fracture surface in order to reveal any effects of hydrogen on the fracture mode. Furthermore, the cross sectional areas were measured.

3.5 Potentiodynamic polarization measurements

Potentiodynamic polarization curves were recorded for two of the alloy variants, 5083B and 7108B, in a 3.5 % NaCl solution. A platinum wire was used as counter electrode, and applied potential was provided from a Gamry^{TM} potentiostat. Potential was measured against a SCE. An OCP measurement was conducted for 1 hour before the cathodic polarization curve was recorded from OCP and down to -1500 mV_{SCE}, with a sweep rate of 600 mV/h. Then, an OCP measurement was conducted for another hour in order for the system to get stabilized before the anodic polarization curve was recorded. The anodic polarization curve was recorded from OCP and 300 mV in anodic direction, by use of the same sweep rate.

3.6 Hardness measurements

An attempt was made to perform hardness measurements on the hydrogen pre-charged samples and the reference samples to reveal differences in microhardness due to hydrogen. A Vickers microhardness test was used, with an applied load of 0.15 N for 14 seconds. The intention was to perform five measurements on each sample, as illustrated in Figure 3.8. However, the surface finish for the hydrogen pre-charged samples was altered to a such extend (see Figure 3.7) that the microhardness measurements could not be conducted. It was also discussed to perform microhardness tests on the cross sections to reveal differences in microhardness due to time-dependent hydrogen diffusion. Watson et al. [37] revealed an increased microhardness close to the charged surface in 99.99 % pure

aluminium (Section 2.4.3). However, the time used on pre-preparations would probably be enough for hydrogen to escape from the samples, and the measurements would hence be wasted.

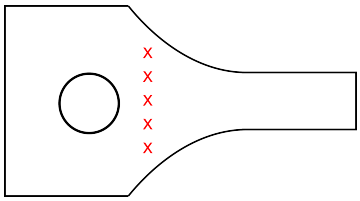

Figure 3.8: Location of the intended microhardness measurements.

3.7 Measurement of hydrogen concentration

In order to confirm hydrogen uptake in (1) the samples that were hydrogen pre-charged prior to tensile testing with in situ cathodic polarization, and (2) the not pre-charged samples being tensile tested with in situ cathodic polarization, efforts was made to get the hydrogen content measured. This was supposed to be done at Hydro Sunndalsøra by use of hydrogen melt extraction analysis. However, in the very end of the project period it turned out that the samples used were too small for the analysis to be conducted. As a result, several other companies were contacted, and these are listed below.

- SINTEF Materials and Chemistry
- Molab AS
- Exova
- YN NILAB
- Degerfors Laboratorium AB

From the abovementioned companies, only Degerfors Laboratorium AB could provide measurements of the hydrogen content in aluminium for the given sample geometry. Unfortunately, they had problems with the test equipment at the time, and measurements could not be conducted. Due to time limitations, further efforts was not made to get the hydrogen content determined.

Chapter 4

Results

4.1 Microstructure characterization

4.1.1 Optical microscope images

Prior to the HE testing a microstructure characterization was conducted for a selection of the alloy variants. The examinations of 5083B, 5083BW, 6082B, 6082C and 6082Z were done by use of a Leica^{TM} MEF4M optical microscope, and performed by Stoknes [71] and Sakshaug [72] as a part of their respective master's theses. In addition to these alloy variants, an optical micrograph of 7108B was obtained from work done by Furu [73]. Optical micrographs showing the microstructures of 6082C and 6082Z are presented in Figure 4.1. Both microstructures are characterized by fibrous middle regions, and with layers of recrystallized grains towards the extrusion surfaces.

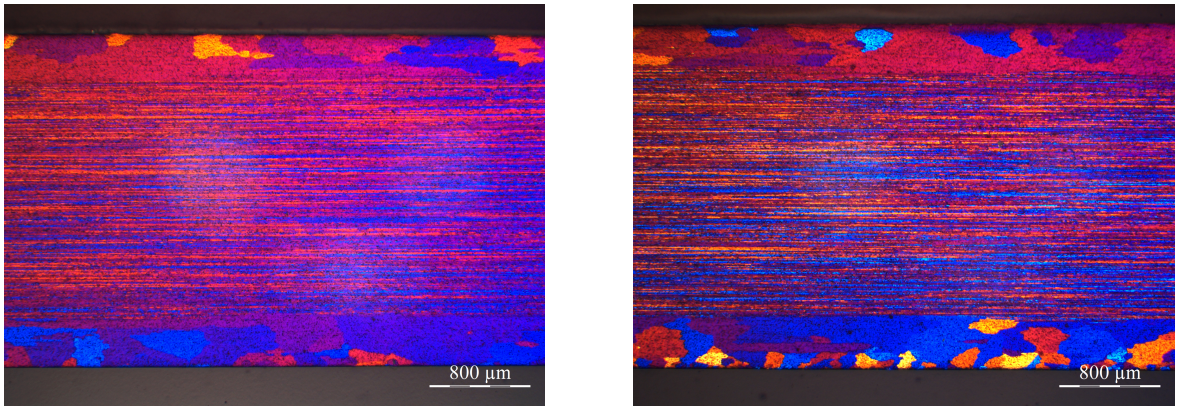

(a) **(b)**

Figure 4.1: Optical micrographs of two EN AW 6082 T6 alloy variants, **(a)** 6082C, and **(b)** 6082Z, perpendicular to the direction of extrusion [71].

Optical micrographs from examination of 5083B and 6082B are presented in Figure 4.2. 5083B was cold worked and stabilized by annealing, and there is no clear fibrous structure observed from the micrograph in Figure 4.2a. On the other hand, the micrograph from 6082B in Figure 4.2b shows a fibrous bulk structure with recrystallized layers close to the external surfaces.

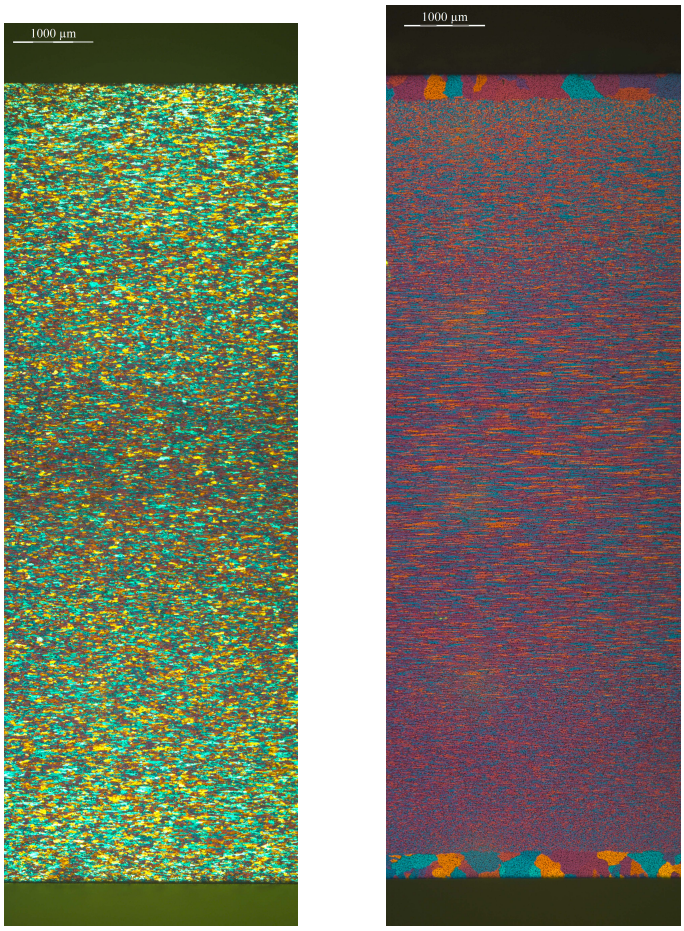

(a) **(b)**

Figure 4.2: Optical micrographs of **(a)** the EN AW 5083 H321 base material, 5083B, and **(b)** the EN AW 6082 T6 base material, 6082B, perpendicular to the direction of extrusion [72].

Optical micrographs showing the microstructures of 7108B and 5083BW are presented in Figure 4.3. The microstructure of 7108B from Figure 4.3a is characterized by a fibrous bulk structure and with thin layers of recrystallized grains close to the extruded surfaces. From the micrograph of 5083BW in Figure 4.3b, it is difficult to define the microstructure since the image is taken parallel to the direction of extrusion. Nevertheless, the fusion zone consists of somewhat larger grains than the heat affected zone (HAZ).

(a)

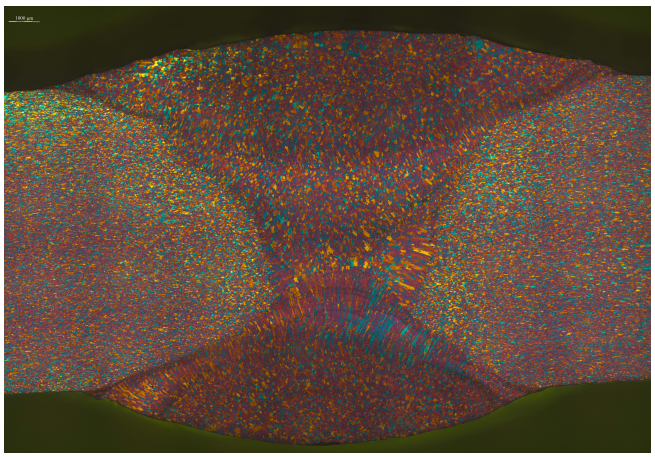

(b)

Figure 4.3: Optical micrographs showing **(a)** the microstructure of the AA 7108.50 base material, 7108B, perpendicular to direction of extrusion, and **(b)** the microstructure of a welded profile of EN AW 5083 H321, 5083BW, parallel to the direction of extrusion [72, 73].

4.1.2 Electron probe micro analysis

In order to detect β-phase formation on grain boundaries of sensitized EN AW 5083 H321, 5083BHT, an EPMA was used. The analysis was performed at 400× magnification, and the results are presented in Figure 4.4. Unfortunately, the resolution provided was not sufficient for the grain boundaries to be examined, and the β-phase could not be detected.

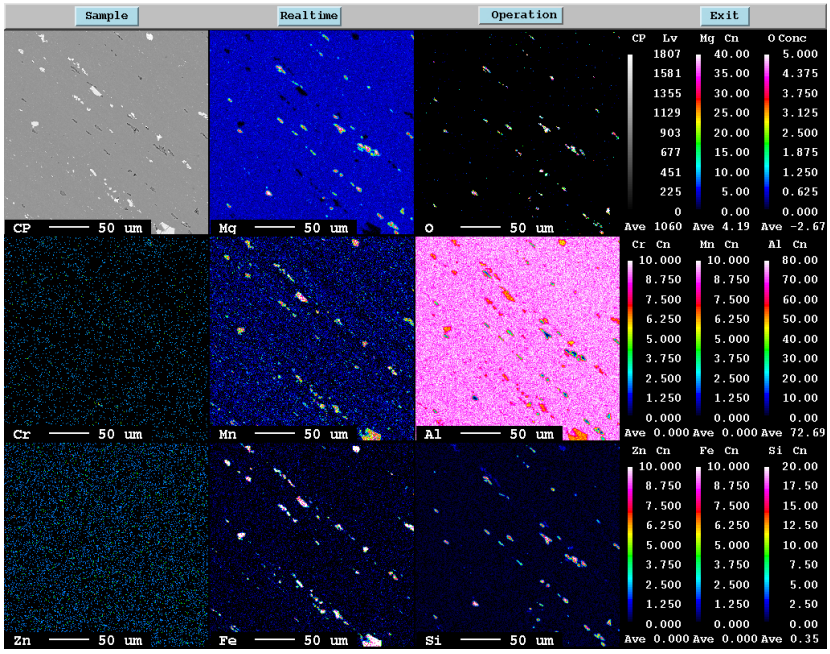

Figure 4.4: Results from analysis of sensitizied EN AW 5083 H321, 5083BHT, obtained by use of an electron probe micro analyzer (EPMA) (400× magnification). The color scale is used to imply the amount of each alloying element.

4.2 Tensile tests

The stress-strain curves obtained from tensile testing of 6082C, 6082Z and 5083BHT are given in Appendix A, Figure A.2-A.4. Three parallels were tested from each of the alloy variants, and average values of $R_{p0.2}$ and R_m were determined from the stress-strain curves. $R_{p0.2}$ and R_m for 5083B, 5083BW, 6082B and 7108B were provided from the supplier, and all values are presented in Table 4.1.

Table 4.1: Yield strength ($R_{p0.2}$) and tensile strength (R_m) for (1) the EN AW 5083 H321 base material, 5083B, (2) a welded profile of EN AW 5083 H321, 5083BW, (3) sensitized EN AW 5083 H321, 5083BHT, (4) the EN AW 6082 T6 base material, 6082B, (5-6) two alloy variants of EN AW 6082 T6, 6082C and 6082Z, and (7) the AA 7108.50 base material, 7108B.

Alloy variant	**$R_{p0.2}$ [MPa]**	**R_m [MPa]**
5083B	247.20	319.80
5083BW	169.50	297.10
5083BHT	182.04	313.26
6082B	323.90	383.20
6082C	323.61	341.38
6082Z	290.22	311.15
7108B	330.00	378.00

4.3 Hydrogen embrittlement tests

Data from the stepwise loading tensile tests are presented in stress-time plots in Figure 4.5-4.11, where applied stress (expressed as % of $R_{p0.2}$) is displayed as a function of time (hours). Each plot presents the results from all samples for the given alloy, and the samples are labeled according to the designation system as previously explained in Section 3.3.5. Initial applied load was determined from the $R_{p0.2}/R_m$-ratio, and varied from 82 % to 132 % of $R_{p0.2}$ for the different alloy variants. Adjustments in stress due to cold creep are reflected as stress fluctuations between the incremental increase every hour, more pronounced for certain alloy variants. Fracture strength (FS) is defined as the stress under which fracture occurs, and these values are presented in Table 4.2-4.8. Time-to-failure is

given in brackets, and average values as well as standard deviations (SD) are included for samples tested under the same conditions.

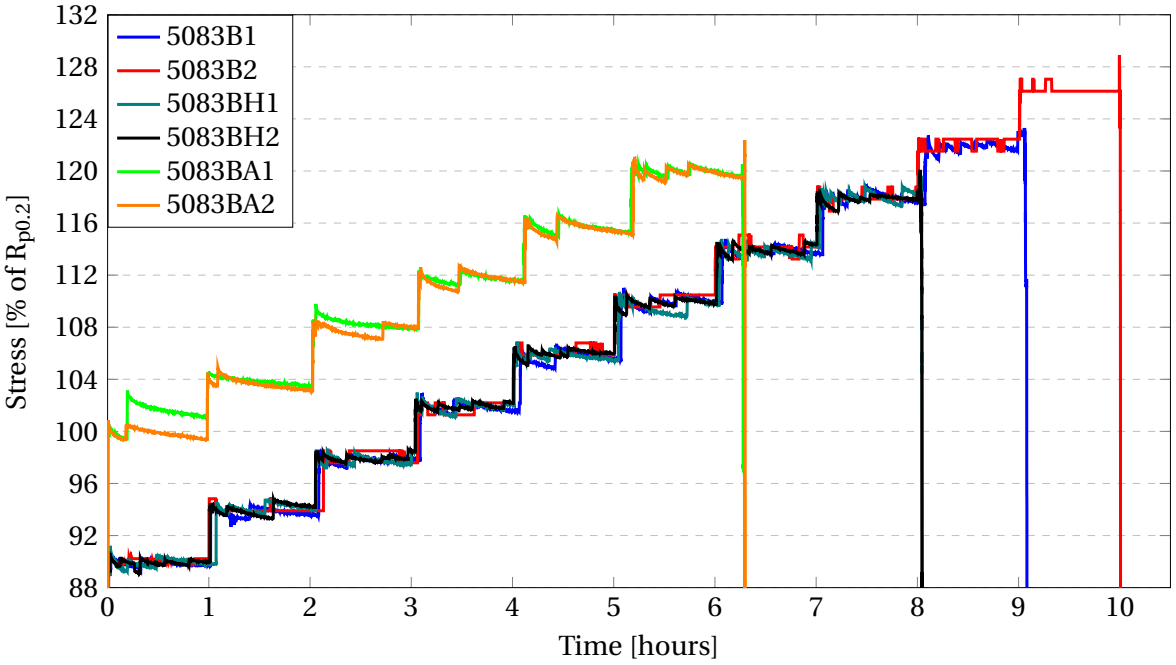

Figure 4.5: Plot showing tensile test results from the EN AW 5083 H321 base material, 5083B, for not pre-charged samples (5083B1-2), hydrogen pre-charged samples (5083BH1-2) and reference samples (5083BA1-2), respectively. Initial applied load was 100 % of $R_{p0.2}$ for 5083BA1 and 5083BA2, and 90 % of $R_{p0.2}$ for the other samples.

As can be seen from Figure 4.5, initial applied load was 100 % of $R_{p0.2}$ for 5083BA1 and 5083BA2. Due to early fractures (after about 6 hours), the initial load was modified to 90 % of $R_{p0.2}$ for the remaining tests. Furthermore, variations in time-to-failure are observed between not pre-charged samples, hydrogen pre-charged samples and reference samples, respectively. From the FS values given in Table 4.2, a decline in average FS between hydrogen pre-charged samples and reference samples of barely 2 % of $R_{p0.2}$ can be observed. The highest average FS and also the highest SD are found for the not pre-charged samples. These findings do not indicate any significant effect from the presence of hydrogen on the mechanical properties of 5083B.

Table 4.2: Fracture strength (FS) obtained from tensile testing of the EN AW 5083 H321 base material, 5083B, for not pre-charged samples (5083B1-2), hydrogen pre-charged samples (5083BH1-2) and reference samples (5083BA1-2), expressed as % of $R_{p0.2}$. Time-to-failure (tt:mm) is given in brackets, and average values (Avg. FS) together with standard deviations (SD) are included for samples tested under the same conditions.

Sample	FS [% of $R_{p0.2}$]	Avg. FS [% of $R_{p0.2}$]	SD
5083B1	123.3 (09:05)	126.1	4.0
5083B2	128.9 (10:01)		
5083BH1	119.6 (08:04)	119.9	0.3
5083BH2	120.1 (08:04)		
5083BA1	120.8 (06:18)	121.6	1.1
5083BA2	122.4 (06:18)		

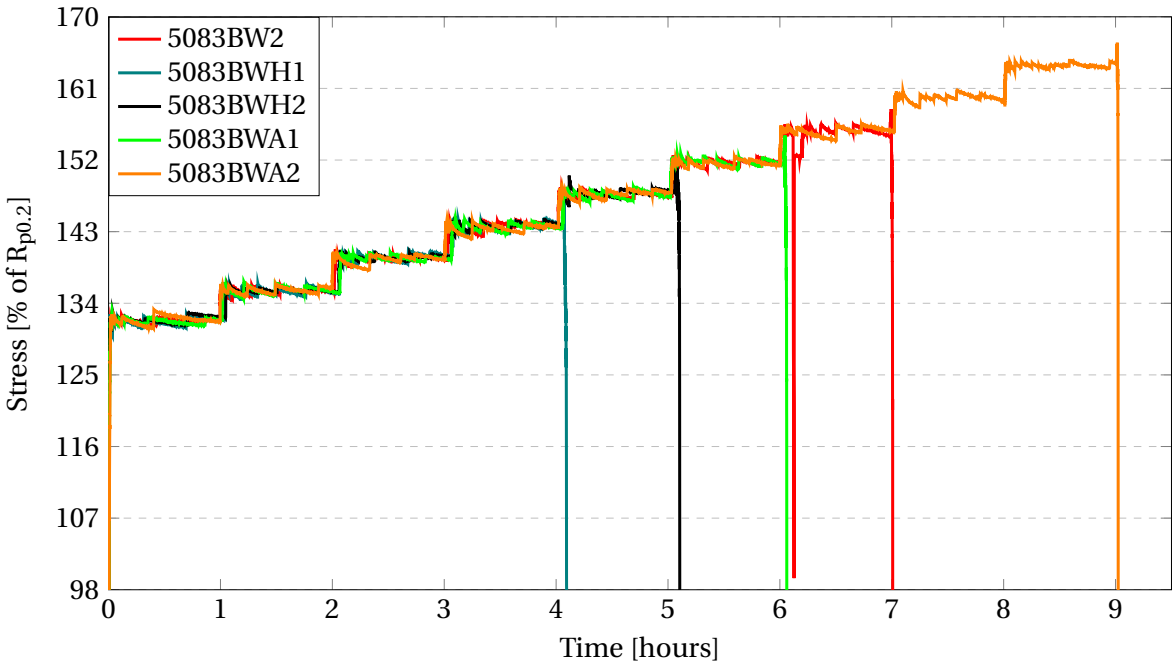

Figure 4.6: Plot showing tensile test results from the welded profile of EN AW 5083 H321, 5083BW, for one of the not pre-charged samples (5083BW2), hydrogen pre-charged samples (5083BWH1-2) and reference samples (5083BWA1-2), respectively. Initial applied load was 132 % of $R_{p0.2}$. The stress-time curve for 5083BW1 is not included in the plot due to the prolonged tensile test.

Due to a large gap between $R_{p0.2}$ and R_m for 5083BW (Table 4.1), the stepwise loading tensile test of 5083BW1 sample became very time consuming with an initial load of 100 % of $R_{p0.2}$. The stress-time curve of 5083BW1 is therefore not included in Figure 4.6. Initial applied load for the remaining samples was 132 % of $R_{p0.2}$. The sharp drop in applied stress for 5083BW2 after approximately 6 hours occurred accidentally as the load was adjusted in the wrong direction. The stress-time plots reveal significant variations in time-to-failure also for samples tested under the same conditions. Moreover, Table 4.3 shows a small decline in average FS for the hydrogen pre-charged samples. The highest average FS is found for the not pre-charged samples, and this value is almost equal to average FS for the reference samples. The relatively large SD should be noted, especially pronounced for the reference samples. These findings do not indicate any effect from the presence of hydrogen on the mechanical properties of 5083BW.

Table 4.3: Fracture strength (FS) obtained from tensile testing of the welded profile of EN AW 5083 H321, 5083BW, for not pre-charged samples (5083BW1-2), hydrogen pre-charged samples (5083BWH1-2) and reference samples (5083BWA1-2), expressed as % of $R_{p0.2}$. Time-to-failure (tt:mm) is given in brackets, and average values (Avg. FS) together with standard deviations (SD) are included for samples tested under the same conditions.

Sample	**FS [% of $R_{p0.2}$]**	**Avg. FS [% of $R_{p0.2}$]**	**SD**
5083BW1	165.3 (16:02)	161.9	4.9
5083BW2	158.4 (07:01)		
5083BWH1	147.5 (04:06)	149.7	3.2
5083BWH2	151.9 (05:07)		
5083BWA1	155.1 (06:04)	160.9	8.2
5083BWA2	166.7 (09:02)		

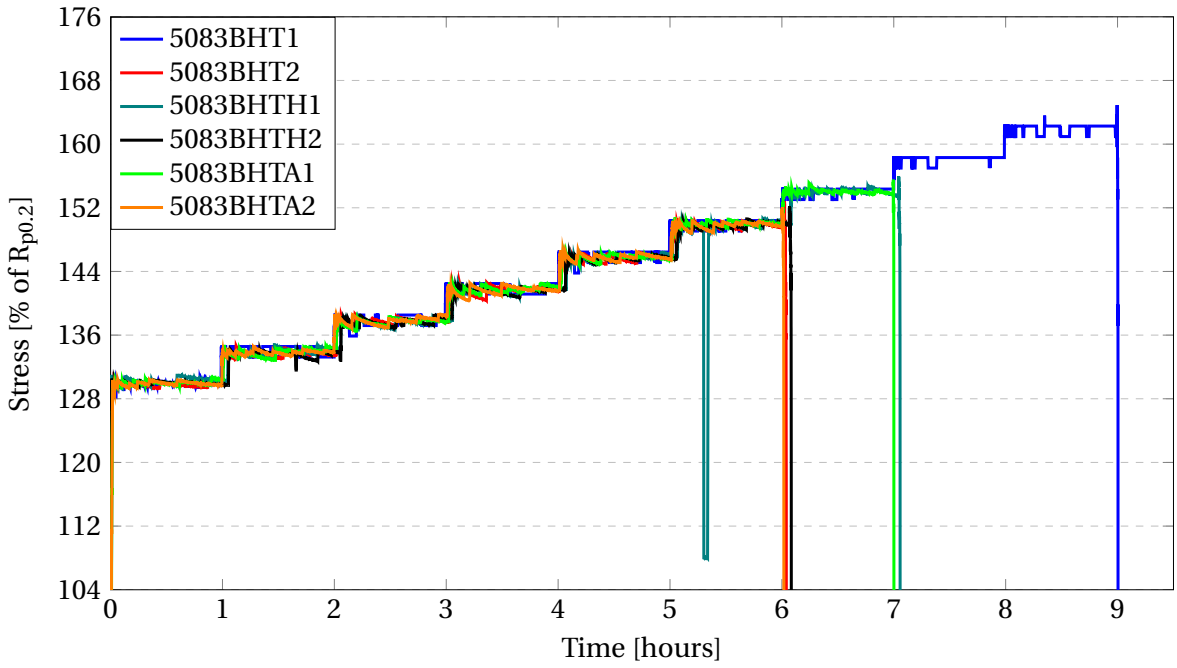

Figure 4.7: Plot showing tensile test results from sensitized EN AW 5083 H321, 5083BHT, for not pre-charged samples (5083BHT1-2), hydrogen pre-charged samples (5083BHTH1-2) and reference samples (5083BHTA1-2), respectively. Initial applied load was 130 % of $R_{p0.2}$.

From Figure 4.7, a sharp drop in applied stress is observed for the 5083BHTH1 sample after approximately 5.5 hours. This occurred accidentally as the load was adjusted in the wrong direction. Again, differences in time-to-failure are observed between samples being tested under the same conditions. The most pronounced differences were observed between the not pre-charged samples, and that is reflected in the large SD shown in Table 4.4. Average FS values for hydrogen pre-charged samples and reference samples are approximately similar, and the SD are almost identical. These findings do not indicate any effect of hydrogen on the FS of 5083BHT.

Table 4.4: Fracture strength (FS) obtained from tensile testing of sensitized EN AW 5083 H321, 5083BHT, for not pre-charged samples (5083BHT1-2), hydrogen pre-charged samples (5083BHTH1-2) and reference samples (5083BHTA1-2), expressed as % of $R_{p0.2}$. Time-to-failure (tt:mm) is given in brackets, and average values (Avg. FS) together with standard deviations (SD) are included for samples tested under the same conditions.

Sample	**FS [% of $R_{p0.2}$]**	**Avg. FS [% of $R_{p0.2}$]**	**SD**
5083BHT1	164.9 (09:00)	158.9	8.5
5083BHT2	152.9 (06:03)		
5083BHTH1	155.9 (07:04)	154.1	2.6
5083BHTH2	152.2 (06:05)		
5083BHTA1	155.5 (07:00)	153.8	2.5
5083BHTA2	152.1 (06:01)		

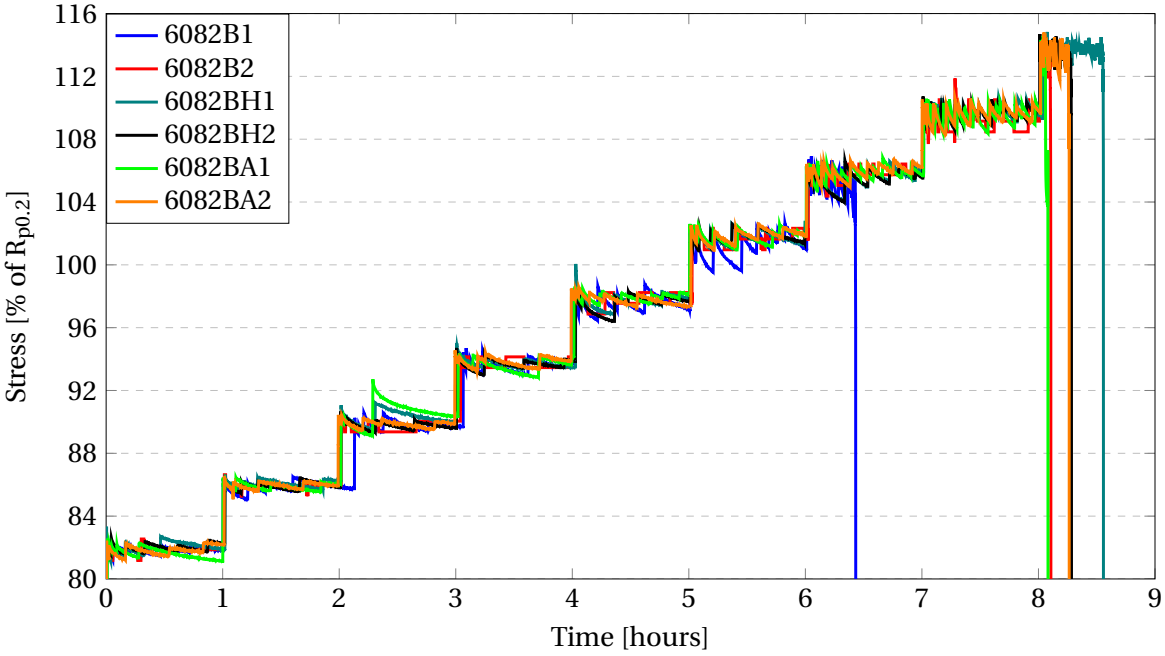

Figure 4.8: Plot showing tensile test results from the EN AW 6082 T6 base material, 6082B, for not pre-charged samples (6082B1-2), hydrogen pre-charged samples (6082BH1-2) and reference samples (6082BA1-2), respectively. Initial applied load was 82 % of $R_{p0.2}$.

It can be seen from Figure 4.8 that the stress-time plots obtained for 6082B are strikingly similar for all samples, except for 6082B1. Stress adjustments were necessary due to cold creep, and this is observed as stress fluctuations between each incremental increase every hour. The creep was especially pronounced for the last hours before fracture occurred. A large SD is observed for the not pre-charged samples in Table 4.5, whereas FS values for the other samples appear very similar. Again, there are no observed effects from the presence of hydrogen on the mechanical properties.

Table 4.5: Fracture strength (FS) obtained from tensile testing of the EN AW 6082 T6 base material, 6082B, for not pre-charged samples (6082B1-2), hydrogen pre-charged samples (6082BH1-2) and reference samples (6082BA1-2), expressed as % of $R_{p0.2}$. Time-to-failure (tt:mm) is given in brackets, and average values (Avg. FS) together with standard deviations (SD) are included for samples tested under the same conditions.

Sample	**FS [% of $R_{p0.2}$]**	**Avg. FS [% of $R_{p0.2}$]**	**SD**
6082B1	106.9 (06:26)	110.8	5.4
6082B2	114.6 (08:07)		
6082BH1	114.8 (08:34)	114.8	0.1
6082BH2	114.7 (08:17)		
6082BA1	114.6 (08:05)	114.8	0.2
6082BA2	114.8 (08:16)		

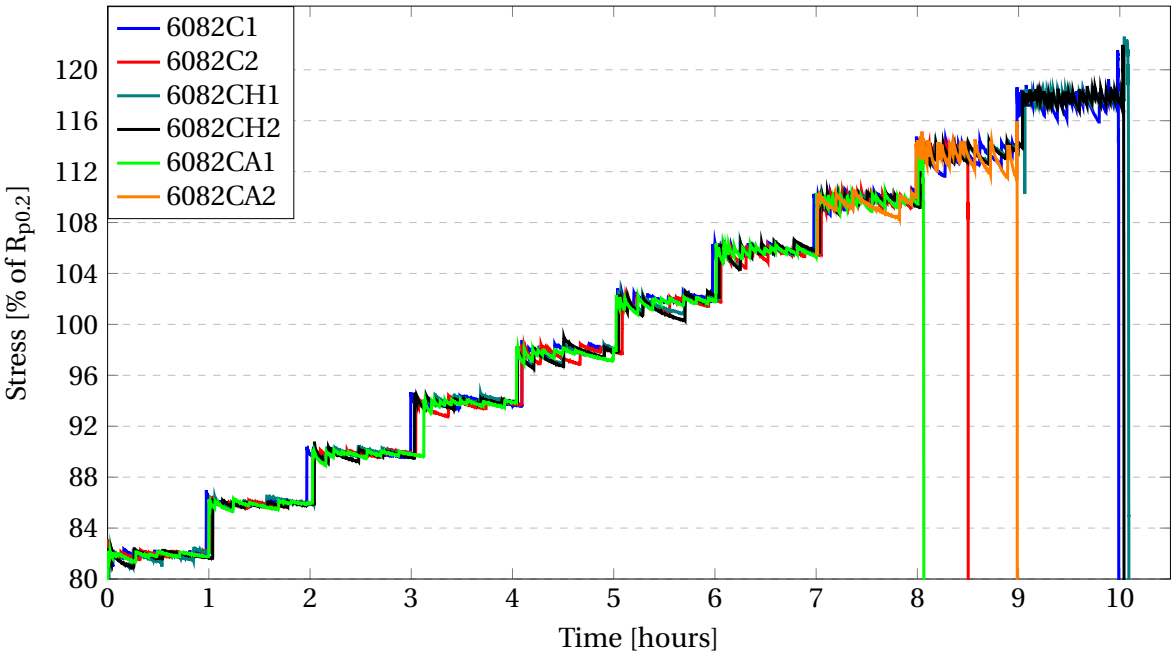

Figure 4.9: Plot showing tensile test results from the EN AW 6082 T6 alloy variant 6082C, for not pre-charged samples (6082C1-2), hydrogen pre-charged samples (6082CH1-2) and reference samples (6082CA1-2), respectively. Initial applied load was 82 % of $R_{p0.2}$.

The discontinuity in the stress-time plot for 6082CA2 in Figure 4.9 was due to a software breakdown after about 7 hours. Also for this alloy, applied stress was frequently adjusted due to cold creep. Furthermore, some differences in time-to-failure are observed, but these are most pronounced between samples tested under different conditions. Average FS values are presented in Table 4.6, and the highest average FS is found for the hydrogen pre-charged samples. Also for 6082C, the presence of hydrogen seems to have minor effects on the mechanical properties. The relatively high SD for the not pre-charged samples should, however, be noted.

Table 4.6: Fracture strength (FS) obtained from tensile testing of a EN AW 6082 T6 alloy variant, 6082C, for not pre-charged samples (6082C1-2), hydrogen pre-charged samples (6082CH1-2) and reference samples (6082CA1-2), expressed as % of $R_{p0.2}$. Time-to-failure (tt:mm) is given in brackets, and average values (Avg. FS) together with standard deviations (SD) are included for samples tested under the same conditions.

Sample	FS [% of $R_{p0.2}$]	Avg. FS [% of $R_{p0.2}$]	SD
6082C1	121.5 (10:00)	117.9	5.1
6082C2	114.4 (08:30)		
6082CH1	122.6 (10:05)	122.3	0.5
6082CH2	122.0 (10:03)		
6082CA1	114.3 (08:04)	115.1	1.2
6082CA2	115.9 (08:59)		

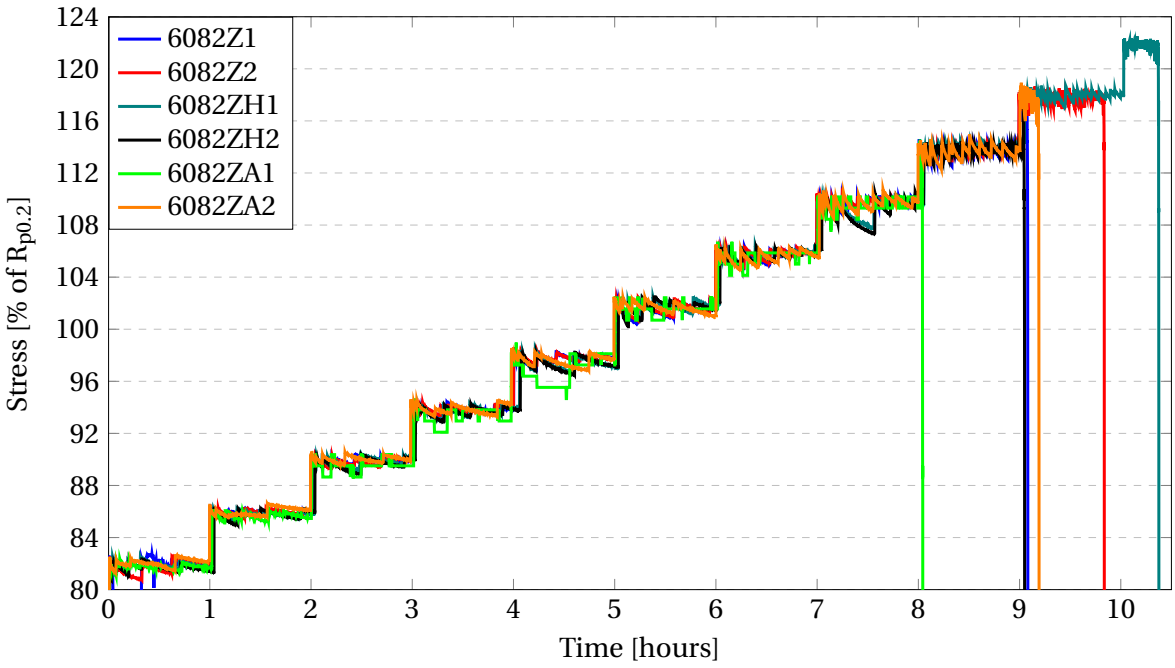

Figure 4.10: Plot showing tensile test results from the EN AW 6082 T6 alloy variant 6082Z, for not pre-charged samples (6082Z1-2), hydrogen pre-charged samples (6082ZH1-2) and reference samples (6082ZA1-2), respectively. Initial applied load was 82 % of $R_{p0.2}$.

It can be seen from Figure 4.10 that the majority of the fractures from tensile testing of 6082Z occurred after 9-10 hours. Again, stress adjustments were necessary due to cold creep, and these are reflected in stress fluctuations between each incremental increase every hour. FS values are given in Table 4.7, where the highest average FS is found for the hydrogen pre-charged samples. Also for 6082Z, average FS for the not pre-charged samples is higher than average FS for the reference samples. These findings do not indicate that the presence of hydrogen has any effects on the mechanical properties of 6082Z.

Table 4.7: Fracture strength (FS) obtained from tensile testing of the EN AW 6082 T6 alloy variant 6082Z, for not pre-charged samples (6082Z1-2), hydrogen pre-charged samples (6082ZH1-2) and reference samples (6082ZA1-2), expressed as % of $R_{p0.2}$. Time-to-failure (tt:mm) is given in brackets, and average values (Avg. FS) together with standard deviations (SD) are included for samples tested under the same conditions.

Sample	**FS [% of $R_{p0.2}$]**	**Avg. FS [% of $R_{p0.2}$]**	**SD**
6082Z1	118.2 (09:05)	118.4	0.3
6082Z2	118.7 (09:50)		
6082ZH1	122.5 (10:23)	120.0	3.5
6082ZH2	117.5 (09:03)		
6082ZA1	114.5 (08:03)	116.7	3.2
6082ZA2	118.9 (09:12)		

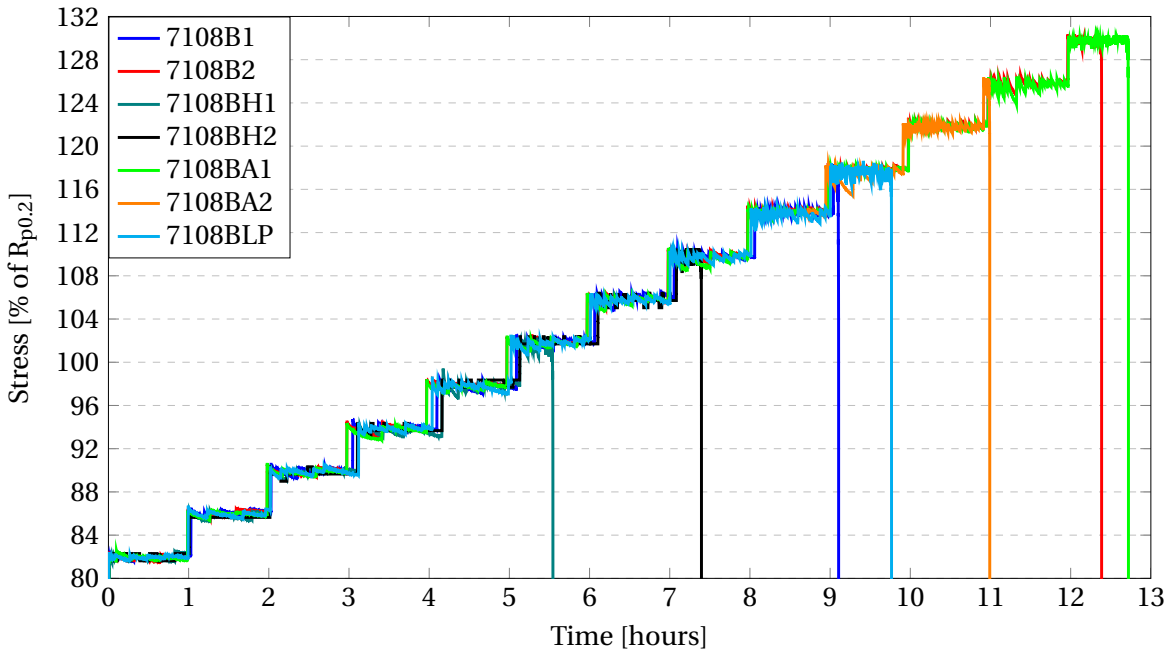

Figure 4.11: Plot showing tensile test results from the AA 7108.50 base material, 7108B, for not pre-charged samples (7108B1-2), hydrogen pre-charged samples (7108BH1-2), reference samples (7108BA1-2) and for the not pre-charged 7108BLP sample tested at -1500 mV_{SCE}. Initial applied load was 82 % of $R_{p0.2}$.

Figure 4.11 reveals considerable differences in time-to-failure for all of the samples from 7108B. Furthermore, data from the first 8.5 hours for the 7108BA2 sample is missing due to software breakdown. The large variations in time-to-failure are reflected in significant SD as shown in Table 4.8. Despite of the marked SD, there is a clear decline in FS for the hydrogen pre-charged samples. This was clearly not observed from the other alloy variants, and may hence indicate an effect of hydrogen on the mechanical properties of 7108B. An additional sample, 7108BLP was also included in the test matrix. This sample was not pre-charged, but tested at an applied potential of -1500 mV_{SCE} rather than -1093 mV_{SCE}. As can be seen from Table 4.8, the FS obtained for 7108BLP was similar to one of the not pre-charged samples (7108B1) that was tested under an applied potential of -1093 mV_{SCE}.

Table 4.8: Fracture strength (FS) obtained from tensile testing of the AA 7108.50 base material, 7108B, for not pre-charged samples (7108B1-2), hydrogen pre-charged samples (7108BH1-2), reference samples (7108BA1-2) and for the not pre-charged 7108BLP sample tested at -1500 mV_{SCE}, expressed as % of $R_{p0.2}$. Time-to-failure (tt:mm) is given in brackets, and average values (Avg. FS) together with standard deviations (SD) are included for samples tested under the same conditions.

Sample	**FS [% of $R_{p0.2}$]**	**Avg. FS [% of $R_{p0.2}$]**	**SD**
7108B1	118.3 (09:06)	124.3	8.5
7108B2	130.4 (12:23)		
7108BH1	102.4 (05:33)	106.4	5.7
7108BH2	110.4 (07:24)		
7108BA1	130.3 (12:43)	128.3	2.8
7108BA2	126.4 (10:59)		
7108BLP	118.6 (09:46)	-	-

Average FS values for not pre-charged samples, hydrogen pre-charged samples and reference samples from all the seven alloy variants are presented in a scatterplot in Figure 4.12. The marked decline in average FS for the hydrogen pre-charged samples of 7108B should be noted.

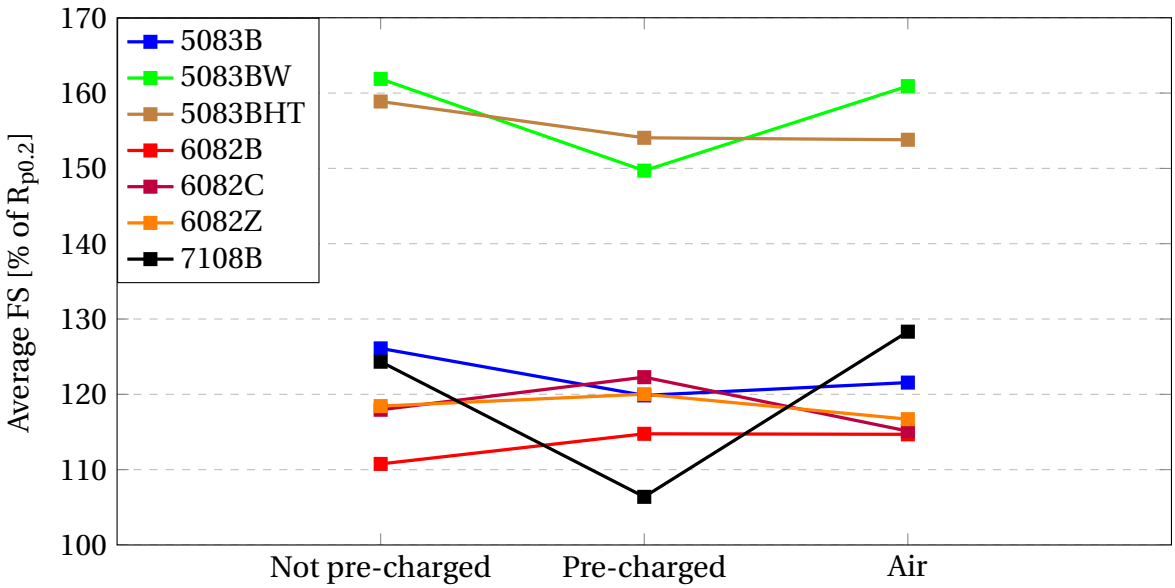

Figure 4.12: Scatterplot showing average fracture strength (FS) values for not pre-charged samples, hydrogen pre-charged samples and reference samples from the seven alloy variants.

4.4 Current monitoring

Applied potential was kept constant during the stepwise loading tensile tests, while the varying current was monitored and logged every five seconds by the Gamry^{TM} software. The current-time curves from all the tensile tests performed with in situ cathodic polarization are presented in Appendix B, Figure B.1-B.8. Interesting to note from these curves is the large variations in current necessary to keep a constant potential. A general trend was that the current requirements were smaller for the hydrogen pre-charged samples compared to the samples not being pre-charged.

4.5 In situ optical microscope images

Optical microscope images were taken from half of all samples in order to study crack initiation and/or propagation, and to monitor the amount of hydrogen evolved. Unfortunately, the microscope was very sensitive to any vibrations, and this made the imaging somewhat difficult. Furthermore, it was difficult to keep the entire sample in focus as topographical differences were introduced by increased amount of deformation. Three image series are included in the report, and these are selected on the basis of image quality.

The image serie in Figure 4.13 is obtained during tensile testing of the not pre-charged 7108B1 sample, and shows how the area close to the notch changes as a result of increased deformation. As can be seen from these images, certain regions became dark during tensile testing. This made it difficult to keep the images in focus, and hence also to notice crack initiation and/or propagation.

Figure 4.14 shows the image serie obtained during tensile testing of the hydrogen precharged 6082BH1 sample. From these images, only minor changes are observed between each stress level. Again, regions close to the notch became dark with increased deformation, however to a lesser extend than what was observed for the 7108B sample. Moreover, a number of small pits can be observed on the surface. Pitting was also observed for a few other samples, and further examination was performed by use of SEM. A SEM image showing the pitting occurrence is included in Appendix C, Figure C.1.

The image serie obtained during tensile testing of the 6082ZA1 reference sample, is presented in Figure 4.15. Dark regions are again observed with increased stress. Neither for this sample any crack initiation and/or propagation could be observed.

The optical microscope images also revealed the amount of hydrogen evolved during tensile testing. Extensive hydrogen evolution was only observed for two of the samples tested at an applied potential of -1093 mV_{SCE}, and those were 5083B1 and 6082Z2. In addition, the 7108BLP sample tested at -1500 mV_{SCE} showed extensive hydrogen evolution.

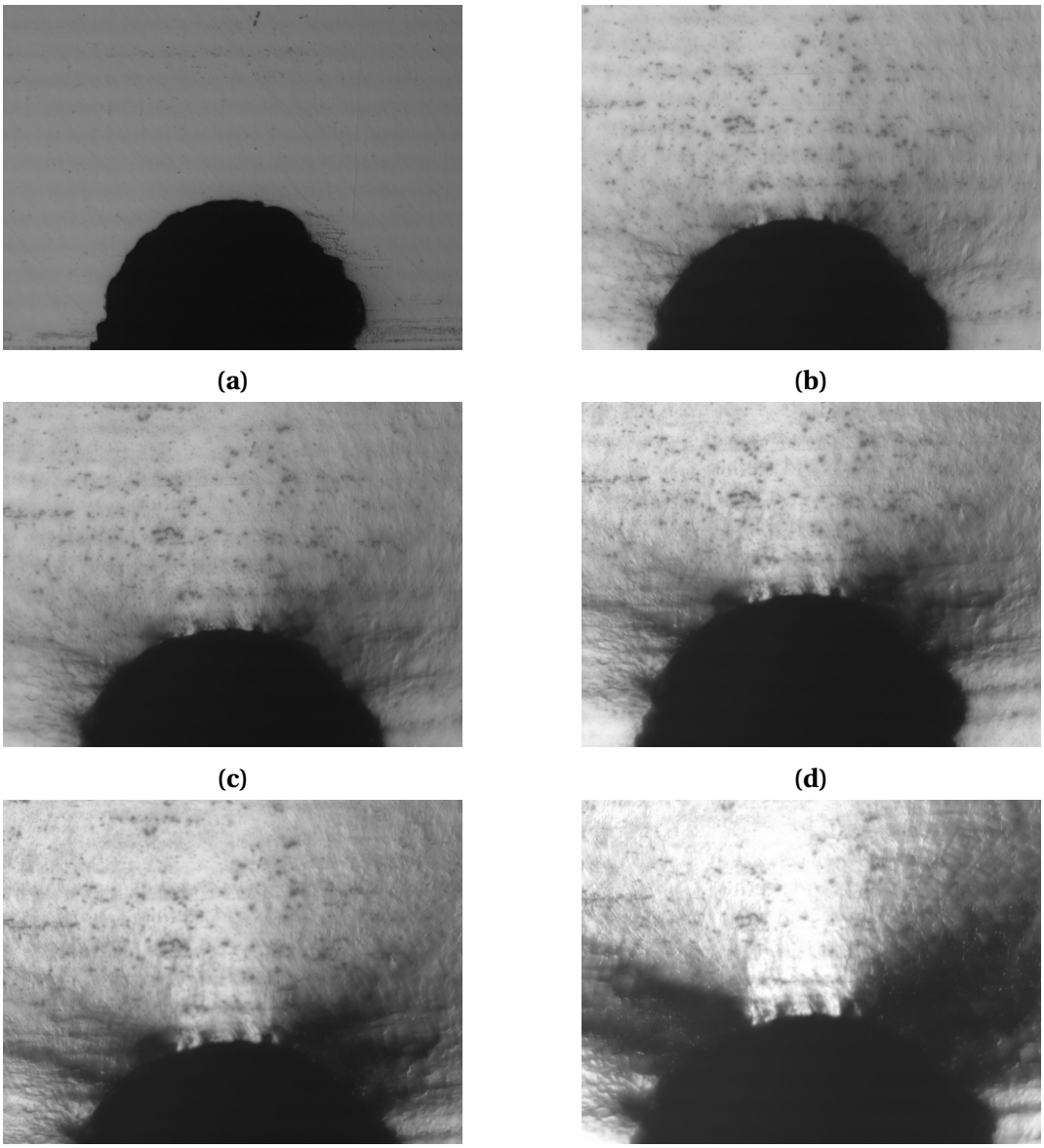

(a) **(b)** **(c)** **(d)** **(e)** **(f)**

Figure 4.13: Optical microscope images obtained during tensile testing of the AA7108.50 base material, 7108B, for the not pre-charged sample 7108B1 (16× magnification). The images were taken at different loads: **(a)** 82 % of $R_{p0.2}$, **(b)** 86 % of $R_{p0.2}$, **(c)** 94 % of $R_{p0.2}$, **(d)** 102 % of $R_{p0.2}$, **(e)** 106 % of $R_{p0.2}$, and **(f)** 114 % of $R_{p0.2}$. Fracture occurred at 118.3 % of $R_{p0.2}$.

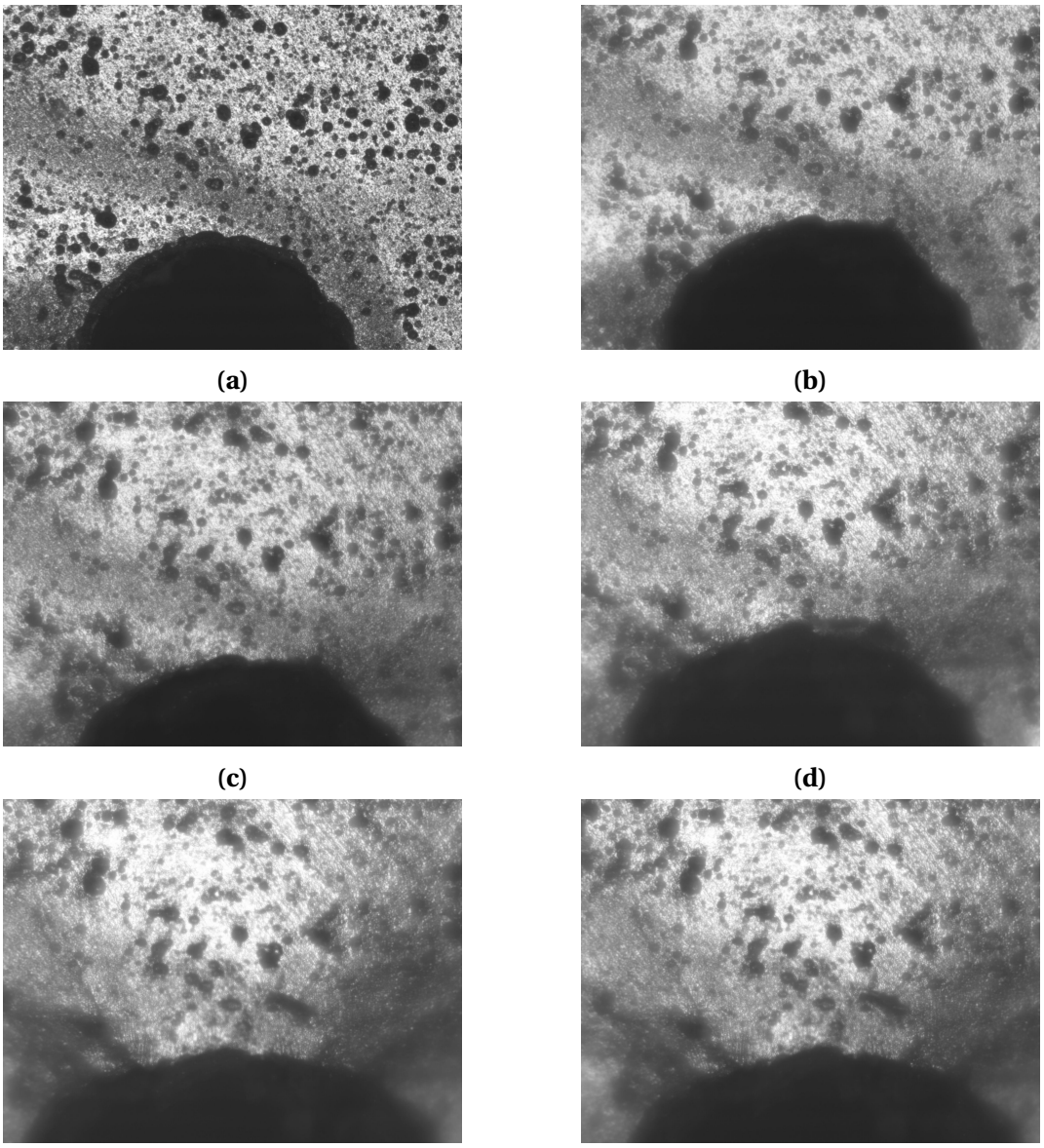

(a) **(b)** **(c)** **(d)** **(e)** **(f)**

Figure 4.14: Optical microscope images obtained during tensile testing of the EN AW 6082 T6 base material, 6082B, for the hydrogen pre-charged sample 6082BH1 (16× magnification). The images were taken at different loads: **(a)** 82 % of $R_{p0.2}$, **(b)** 91 % of $R_{p0.2}$, **(c)** 106 % of $R_{p0.2}$, **(d)** 109 % of $R_{p0.2}$, **(e)** 110 % of $R_{p0.2}$, and **(f)** 114 % of $R_{p0.2}$. Fracture occurred at 114.8 % of $R_{p0.2}$.

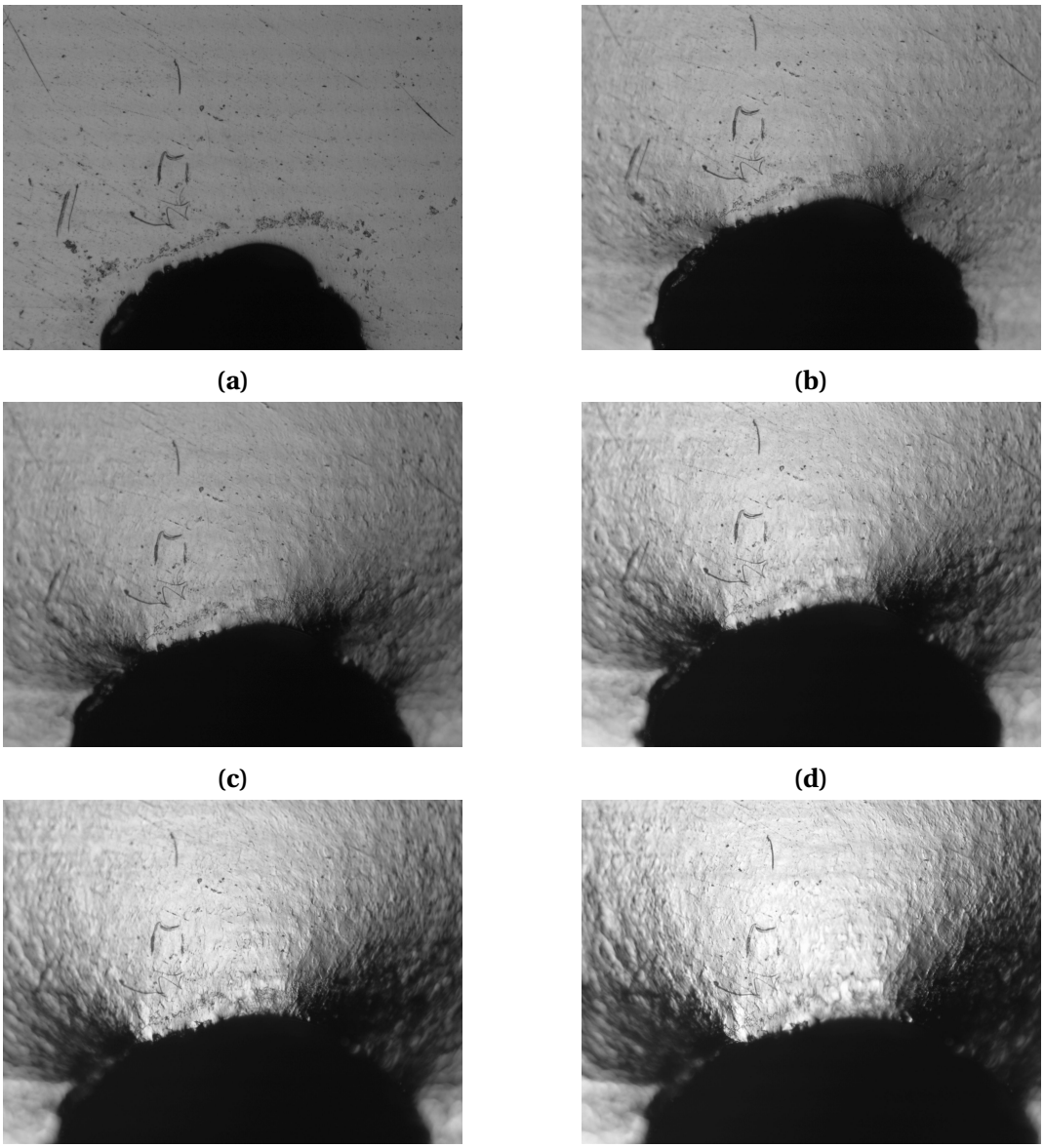

(a) **(b)** **(c)** **(d)** **(e)** **(f)**

Figure 4.15: Optical microscope images obtained during tensile testing of the EN AW 6082 T6 alloy variant 6082Z, for the 6082ZA1 reference sample (16× magnification). The images were taken at different loads: **(a)** 82 % of $R_{p0.2}$, **(b)** 86 % of $R_{p0.2}$, **(c)** 94 % of $R_{p0.2}$, **(d)** 98 % of $R_{p0.2}$, **(e)** 102 % of $R_{p0.2}$, and **(f)** 106 % of $R_{p0.2}$. Fracture occurred at 114.5 % of $R_{p0.2}$.

4.6 Fracture surface examination

The macroscopic appearances were strikingly similar for all samples, and characterized by shear fractures with fracture planes oriented 45° to applied tensile stress. The ductile fracture features were, however, not reflected in any significant amount of necking for none of the samples. In order to reveal any brittle features as a result of HE, all fracture surfaces were examined by use of SEM. Only a selection of the images from each alloy is included in the report, and these are taken from the same areas for all samples. An overview image of a fracture surface is given in Figure 4.16, where the mechanically induced notch is observed on the left side. The SEM images were taken from the middle region and from the left edge of the fracture surfaces, and these areas are indicated by white rectangles in Figure 4.16. The regions were chosen based on the assumption that any effects of hydrogen is believed to be most pronounced close to an external surface, and least pronounced in the middle. SEM images from all of the seven alloy variants will be presented in the following sections.

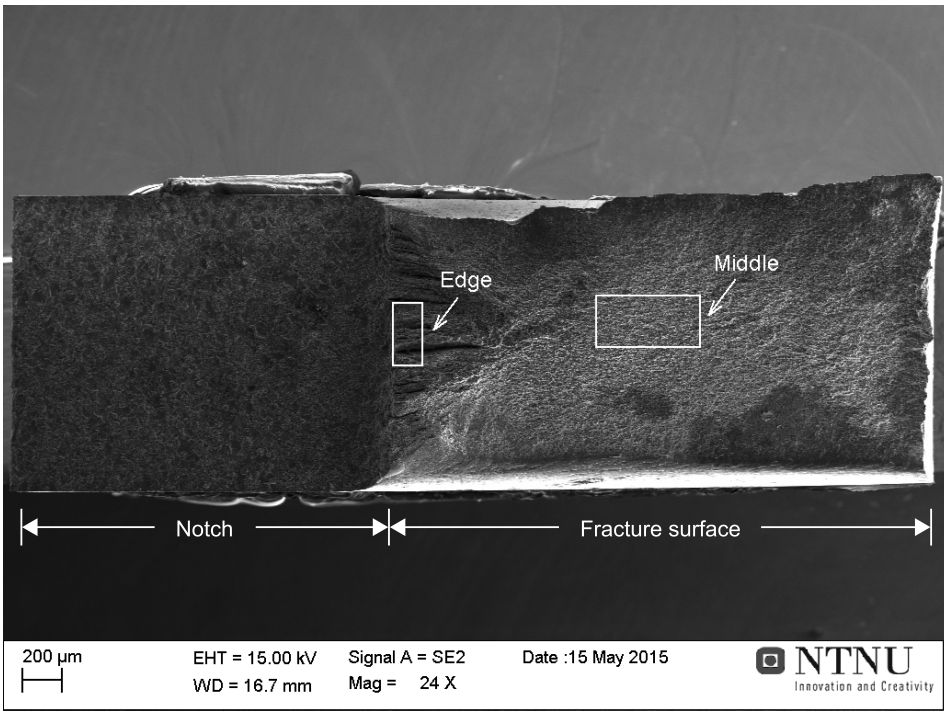

Figure 4.16: SEM image showing a fracture surfaces with the mechanically induced notch located on the left side. All SEM images were taken from the middle region and from the left edge, and these areas are indicated by white rectangles (24× magnification).

4.6.1 5083B

SEM images obtained from fracture surface examination of 5083B are for a not pre-charged sample, a hydrogen pre-charged sample and a reference sample presented in Figure 4.17-4.19. Ductile features are evident from all images, and dimples are observed both in the middle regions and in regions close to the left edge.

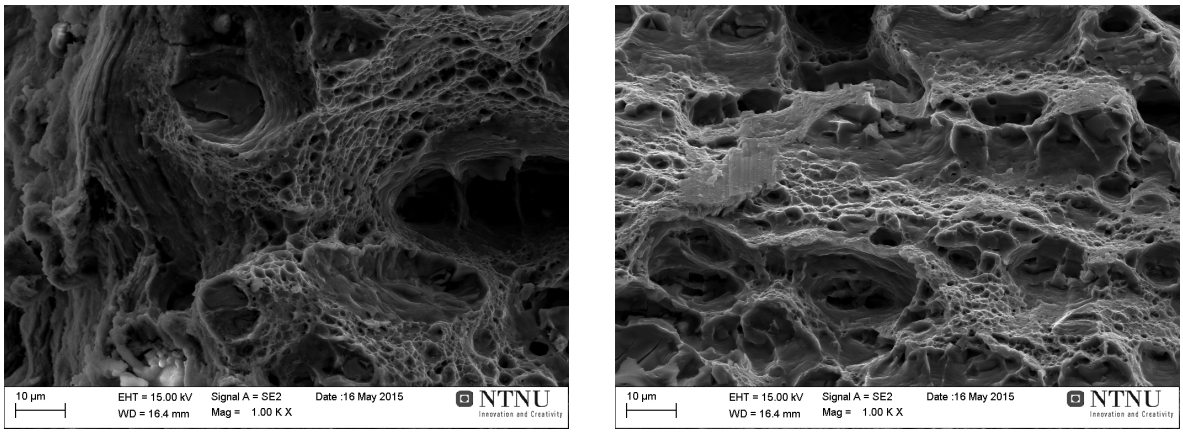

(a) **(b)**

Figure 4.17: SEM images showing **(a)** the left edge and **(b)** the middle region from the fracture surface of a not pre-charged sample from the EN AW 5083 H321 base material, 5083B (1000× magnification).

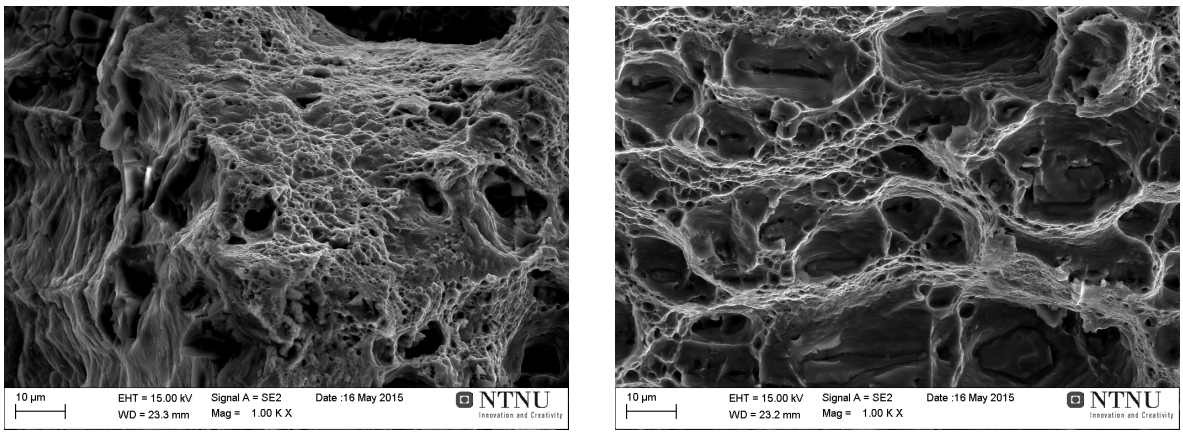

(a) **(b)**

Figure 4.18: SEM images showing **(a)** the left edge and **(b)** the middle region from the fracture surface of a hydrogen pre-charged sample from the EN AW 5083 H321 base material, 5083B (1000× magnification).

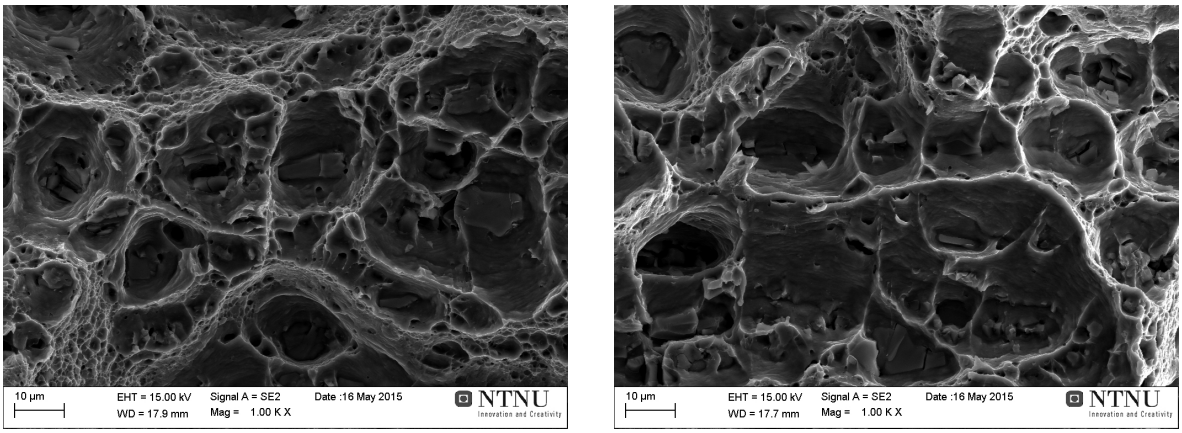

(a) **(b)**

Figure 4.19: SEM images showing **(a)** the left edge and **(b)** the middle region from the fracture surface of a reference sample from the EN AW 5083 H321 base material, 5083B (1000× magnification).

4.6.2 5083BW

SEM images from a not pre-charged sample, a hydrogen pre-charged sample and a reference sample of 5083BW are shown in Figure 4.20-4.22. The fracture surfaces are characterized by large proportions of small dimples, and some of the smaller microvoids seem to contain broken particles. These features are strong evidence indicating ductile fractures.

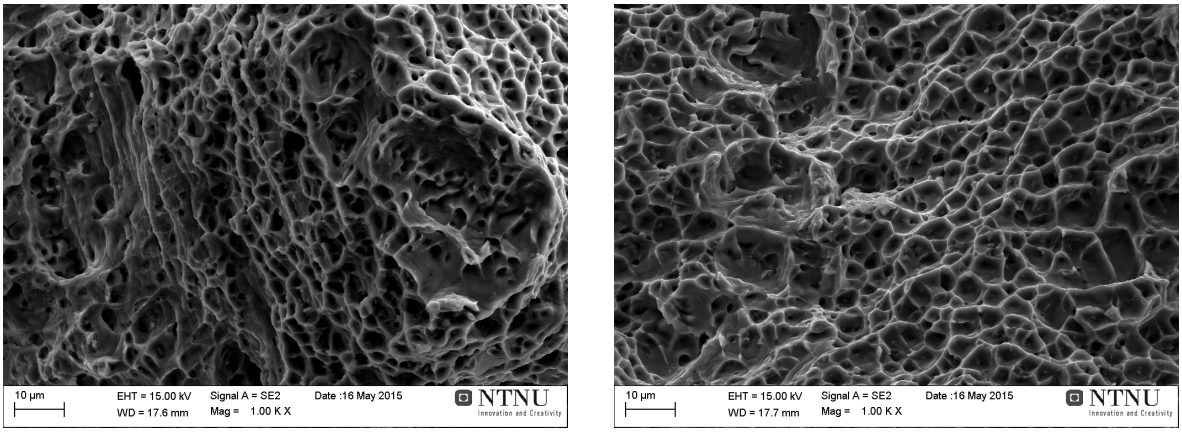

(a) **(b)**

Figure 4.20: SEM images showing **(a)** the left edge and **(b)** the middle region from the fracture surface of a not pre-charged sample from the welded profile of EN AW 5083 H321, 5083BW (1000× magnification).

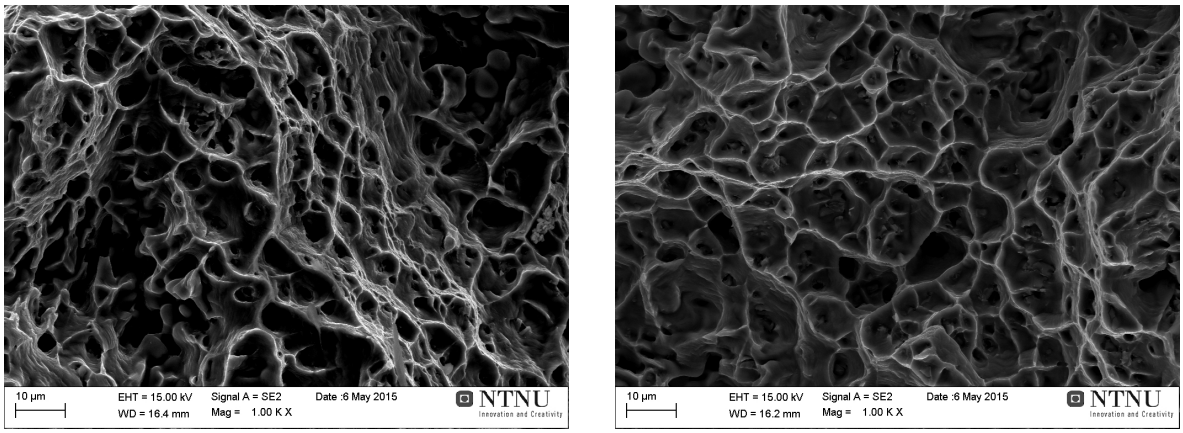

(a) **(b)**

Figure 4.21: SEM images showing **(a)** the left edge and **(b)** the middle region from the fracture surface of a hydrogen pre-charged sample from the welded profile of EN AW 5083 H321, 5083BW (1000× magnification).

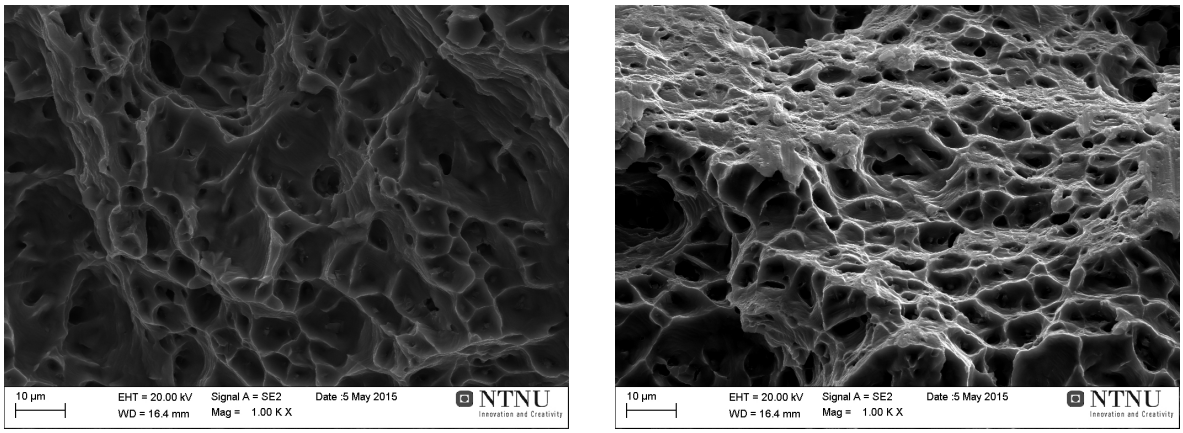

(a) **(b)**

Figure 4.22: SEM images showing **(a)** the left edge and **(b)** the middle region from the fracture surface of a reference sample from the welded profile of EN AW 5083 H321, 5083BW (1000× magnification).

4.6.3 5083BHT

Figure 4.23-4.25 shows the SEM images from a not pre-charged sample, a hydrogen pre-charged sample and a reference sample of 5083BHT. Also from these images, ductile features are dominating the fracture surfaces. There is a mix of smaller and larger dimples, and broken particles are observed within microvoids.

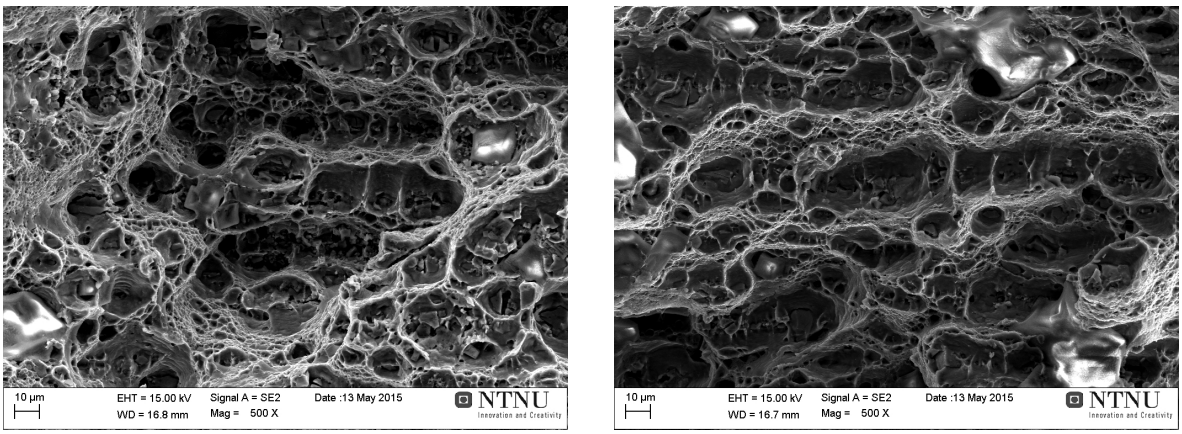

(a) **(b)**

Figure 4.23: SEM images showing **(a)** the left edge and **(b)** the middle region from the fracture surface of a not pre-charged sample from sensitized EN AW 5083 H321, 5083BHT (500× magnification).

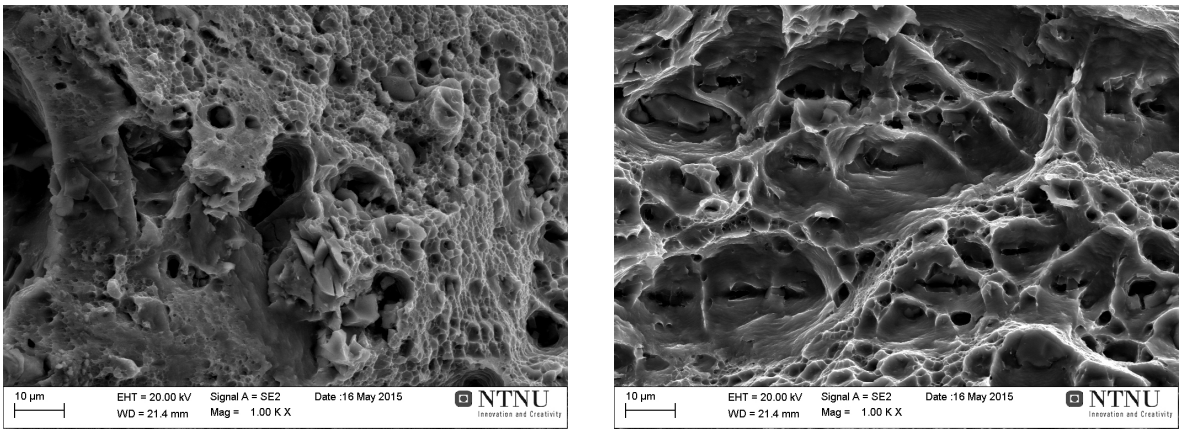

(a) **(b)**

Figure 4.24: SEM images showing **(a)** the left edge and **(b)** the middle region from the fracture surface of a hydrogen pre-charged sample from sensitized EN AW 5083 H321, 5083BHT (1000× magnification).

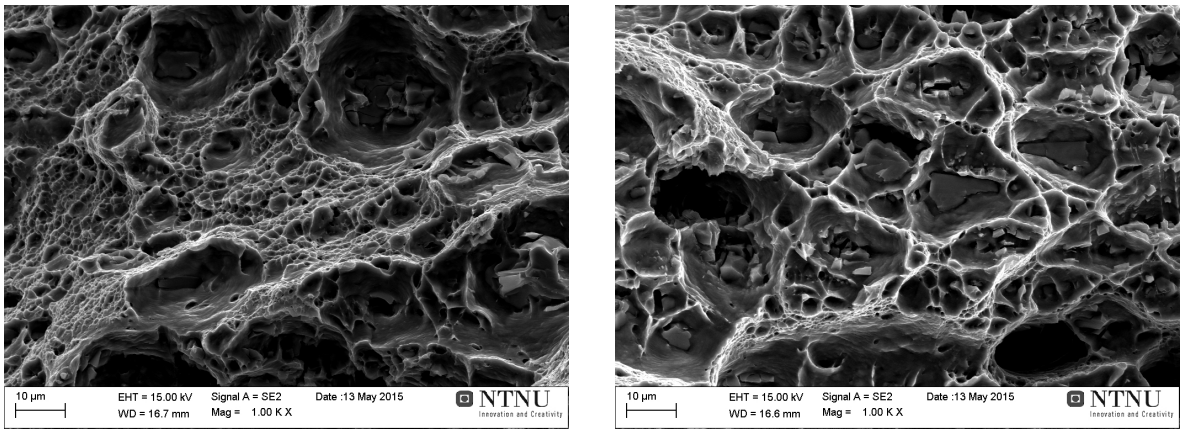

(a) **(b)**

Figure 4.25: SEM images showing **(a)** the left edge and **(b)** the middle region from the fracture surface of a reference sample from sensitized EN AW 5083 H321, 5083BHT (1000× magnification).

4.6.4 6082B

SEM images from fracture surface examination of 6082B are for a not pre-charged sample, a hydrogen pre-charged sample and a reference sample presented in Figure 4.26-4.28. Again, ductile features are dominating the fracture surfaces. Dimples are clearly visible on all surfaces, both in the middle regions and in regions close to the left edge.

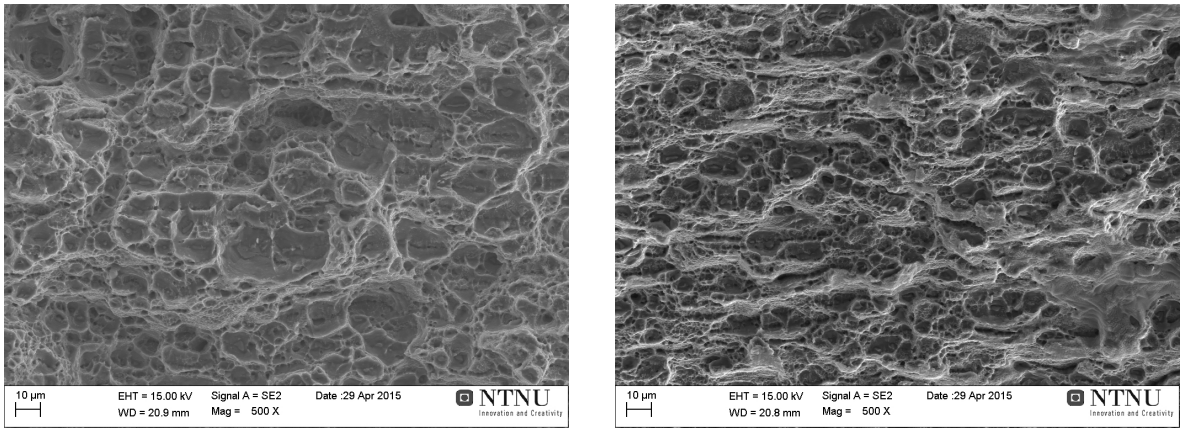

(a) **(b)**

Figure 4.26: SEM images showing **(a)** the left edge and **(b)** the middle region from the fracture surface of a not pre-charged sample from the EN AW 6082 T6 base material, 6082B (500× magnification).

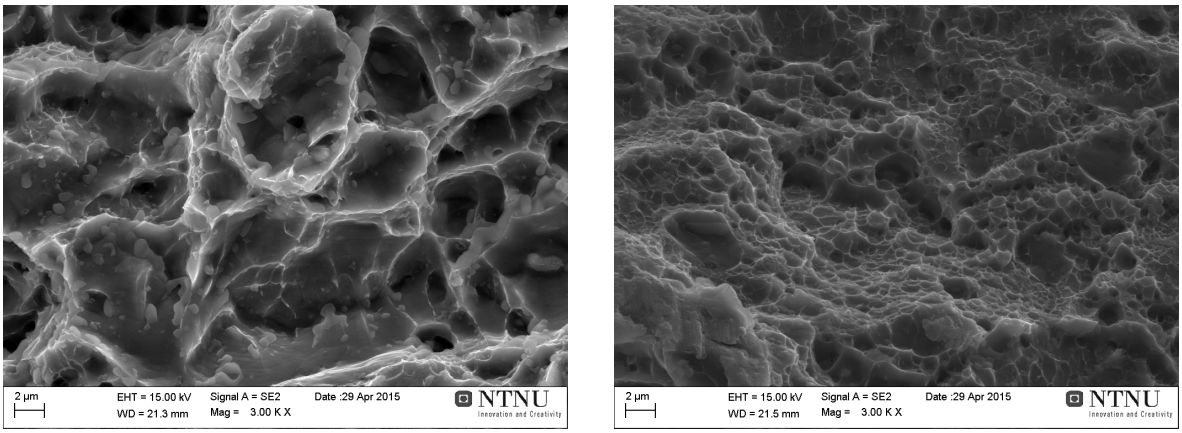

(a) **(b)**

Figure 4.27: SEM images showing **(a)** the left edge and **(b)** the middle region from the fracture surface of a hydrogen pre-charged sample from the EN AW 6082 T6 base material, 6082B (3000× magnification).

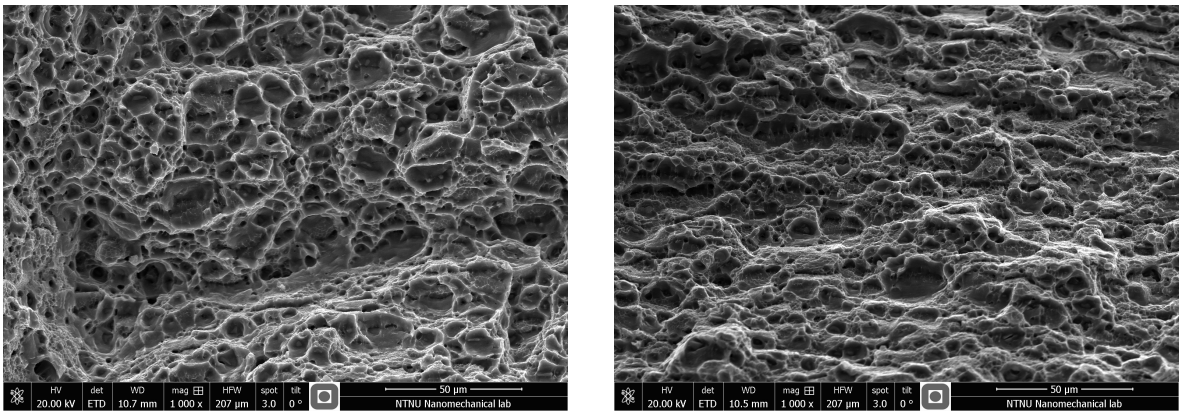

(a) **(b)**

Figure 4.28: SEM images showing **(a)** the left edge and **(b)** the middle region from the fracture surface of a reference sample from the EN AW 6082 T6 base material, 6082B (1000× magnification).

4.6.5 6082C

The SEM images in Figure 4.29-4.31 are obtained from fracture surface examination of a not pre-charged sample, a hydrogen pre-charged sample and a reference sample of 6082C. Ductile features are evident from all samples, both in the middle regions and in the regions towards the left edge.

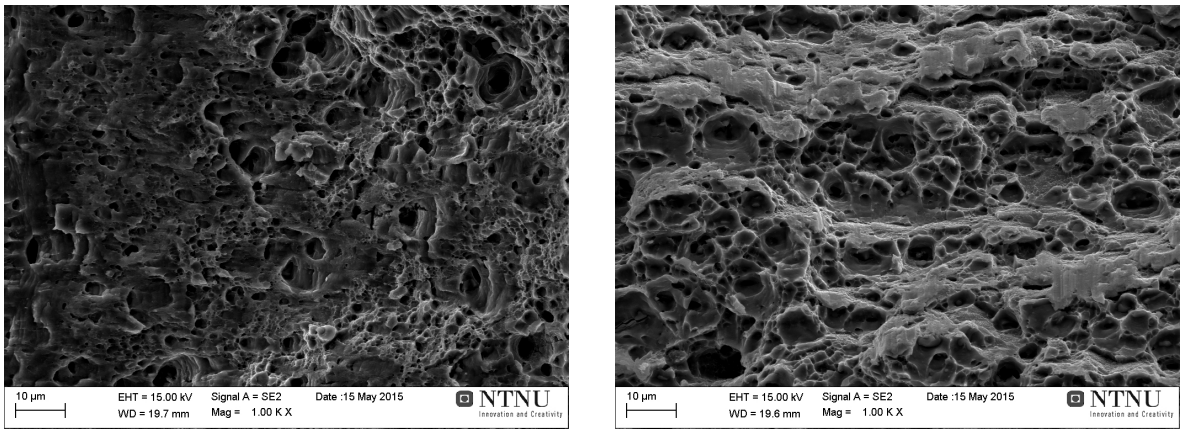

(a) **(b)**

Figure 4.29: SEM images showing **(a)** the left edge and **(b)** the middle region from the fracture surface of a not pre-charged sample from the EN AW 6082 T6 alloy variant 6082C (1000× magnification).

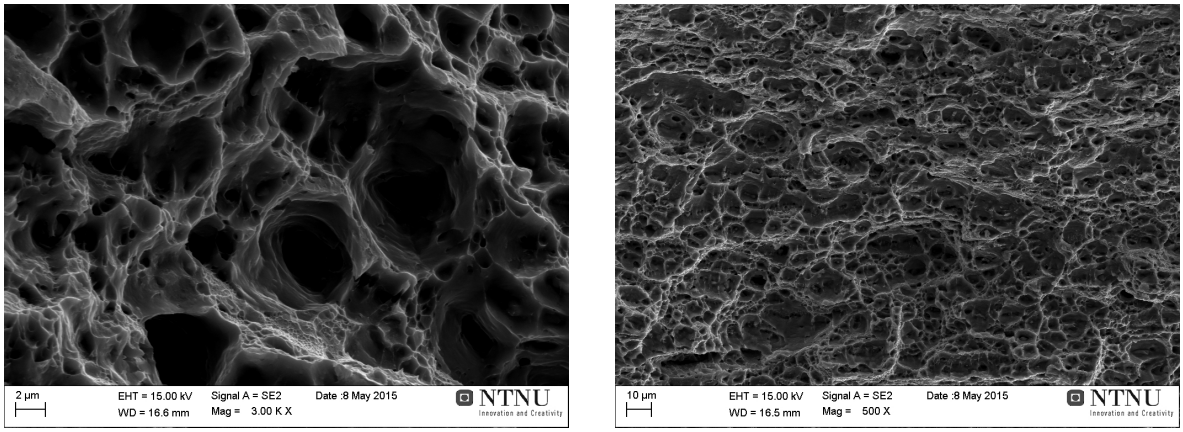

(a) **(b)**

Figure 4.30: SEM images showing **(a)** the left edge (3000× magnification) and **(b)** the middle region (500× magnification) from the fracture surface of a hydrogen pre-charged sample from the EN AW 6082 T6 alloy variant 6082C.

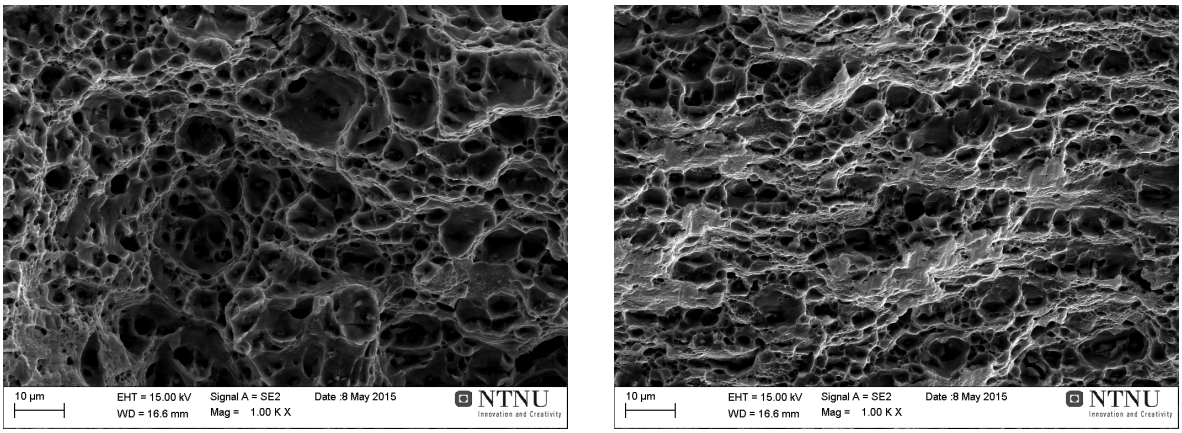

(a) **(b)**

Figure 4.31: SEM images showing **(a)** the left edge and **(b)** the middle region from the fracture surface of a reference sample from of the EN AW 6082 T6 alloy variant 6082C (1000× magnification).

4.6.6 6082Z

Figure 4.32-4.34 shows the SEM images obtained from a not pre-charged sample, a hydrogen pre-charged sample and a reference sample of 6082Z. Neither these images reveal any differences in fracture surface appearance. Ductile features are observed for all samples on the entire surfaces.

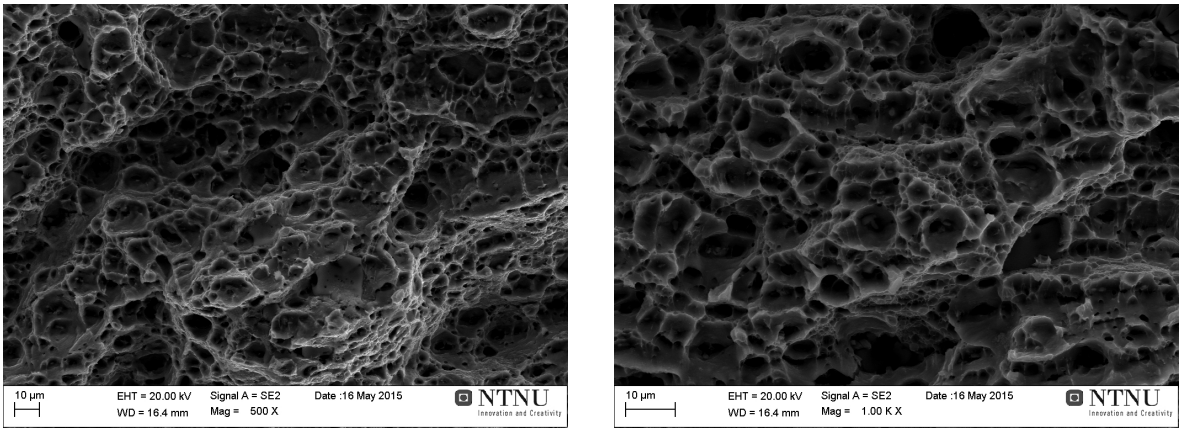

(a) **(b)**

Figure 4.32: SEM images showing **(a)** the left edge (500× magnification) and **(b)** the middle region (1000× magnification) from the fracture surface of a not pre-charged sample from the EN AW 6082 T6 alloy variant 6082Z.

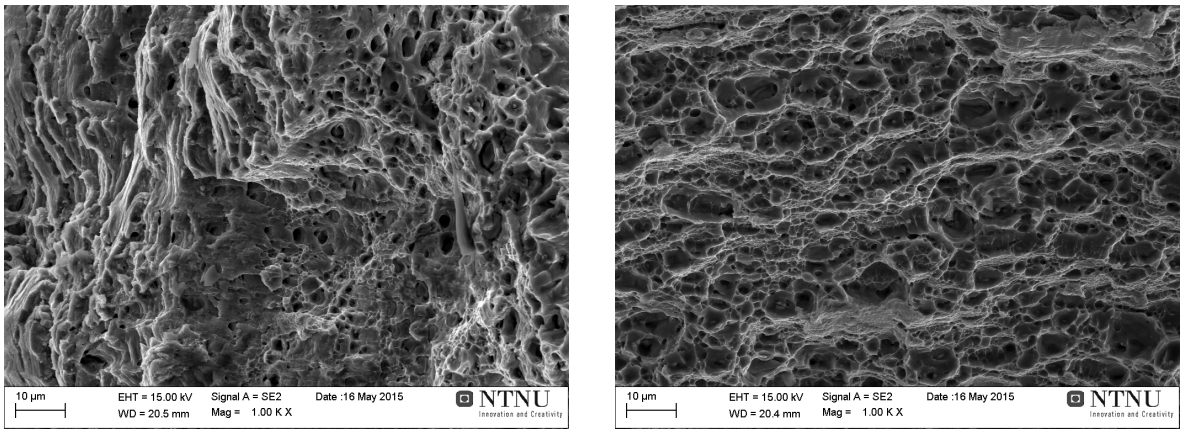

(a) **(b)**

Figure 4.33: SEM images showing **(a)** the left edge and **(b)** the middle region from the fracture surface of a hydrogen pre-charged sample from the EN AW 6082 T6 alloy variant 6082Z (1000× magnification).

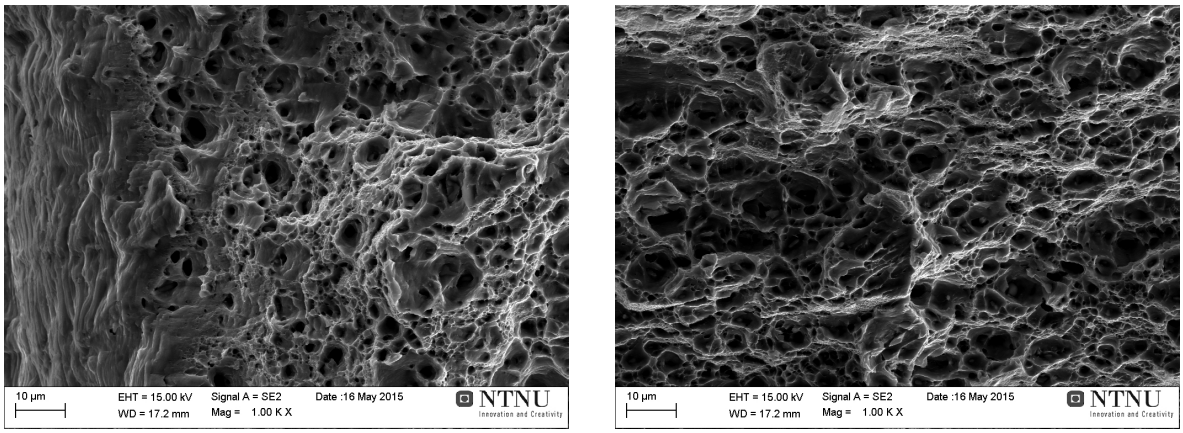

(a) **(b)**

Figure 4.34: SEM images showing **(a)** the left edge and **(b)** the middle region from the fracture surface of a reference sample from the EN AW 6082 T6 alloy variant 6082Z (1000× magnification).

4.6.7 7108B

Fracture surface examination of the 7108B samples revealed different features from what was observed from 5083B, 5083BW, 5083BHT, 6082B, 6082C and 6082Z. An overview image from the left edge of a not pre-charged 7108B sample is given in Figure 4.35. As can be seen from this image, a part of the fracture surface is still characterized by dimples. However, there is a region close to the notch that appears significantly different. The length of this area is varying from a few μm up to about 450 μm.

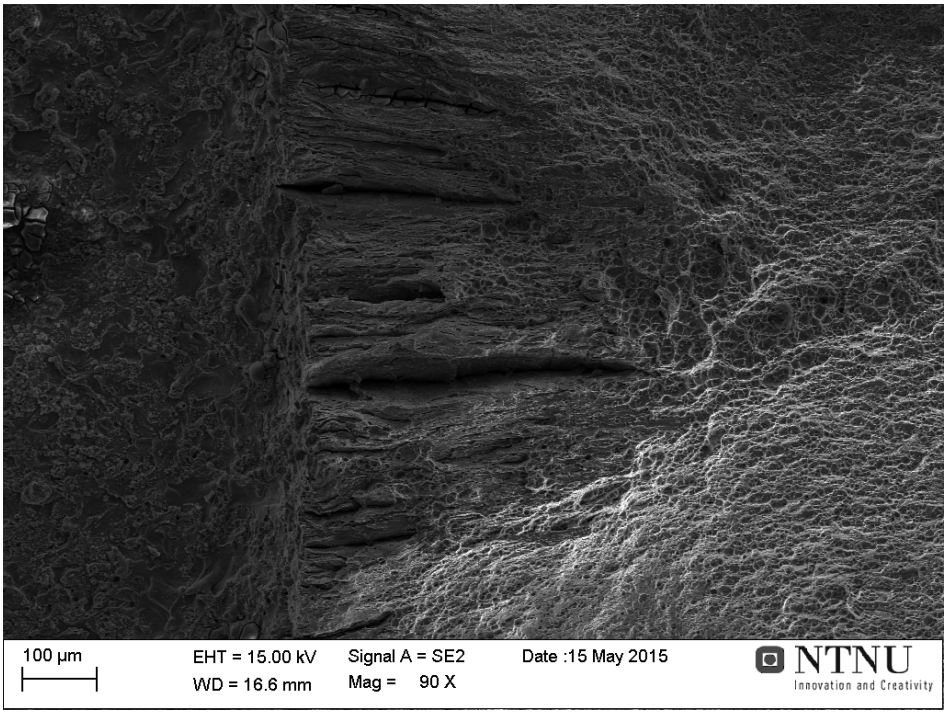

Figure 4.35: SEM image showing the region close to the notch for a not pre-charged sample from the AA 7108.50 base material, 7108B (90× magnification).

A closer look to the left area of a not pre-charged 7108B sample revealed a "terraced" fracture surface as shown in Figure 4.36a-4.36b. The images clearly demonstrate the absence of ductile features, and this may indicate an effect from the presence of hydrogen. In contrast, Figure 4.36c reveals completely ductile features from the middle region of the same sample. It should be noted that the images are obtained at very different magnifications, but the different appearances are anyway clear.

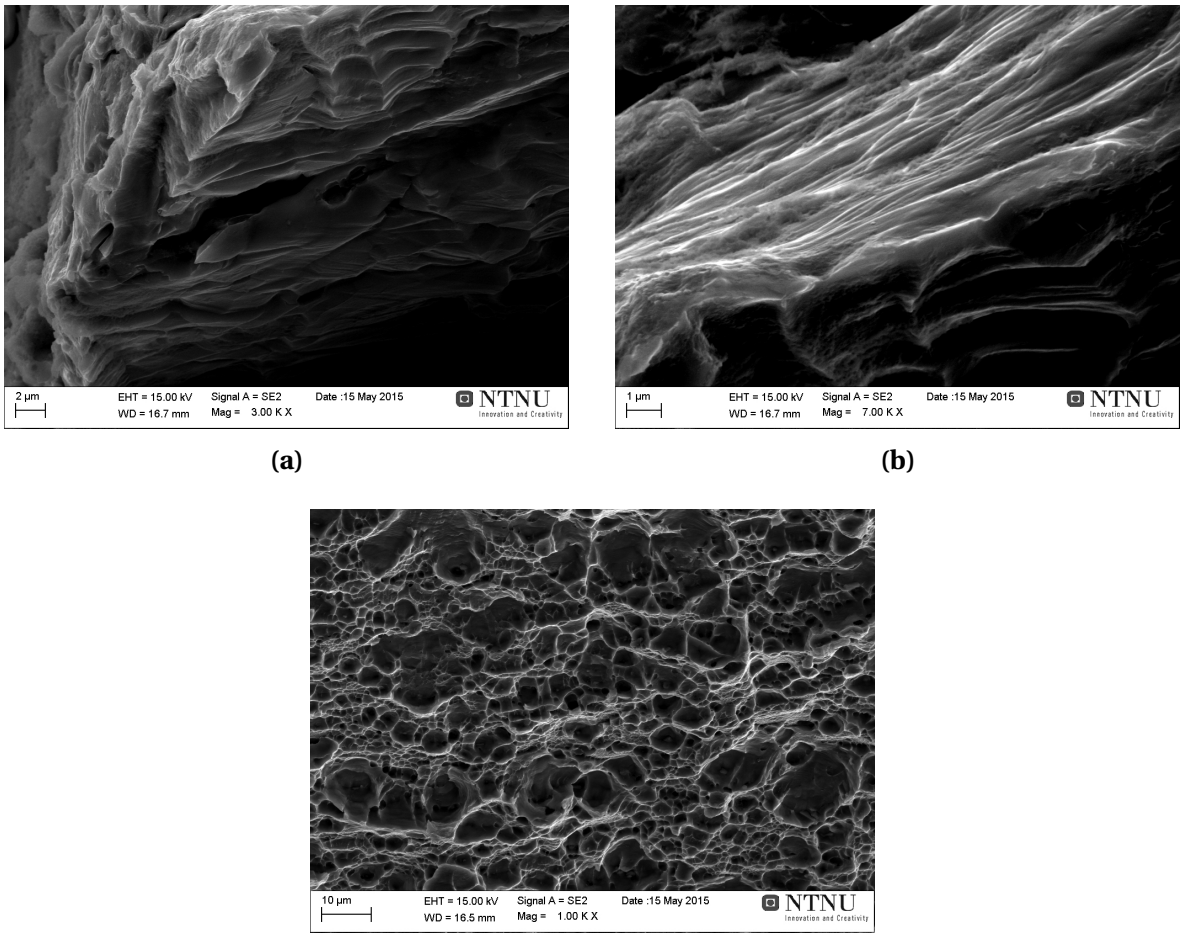

(a) **(b)**

(c)

Figure 4.36: SEM images showing the left edge at **(a)** 3000× magnification and **(b)** at 7000× magnification, and **(c)** the middle region (1000× magnification) from the fracture surface of a not pre-charged sample from the AA 7108.50 base material, 7108B.

An overview image from a hydrogen pre-charged 7108B sample taken close to the notch is shown in Figure 4.37a. The area marked with the white rectangular is magnified in Figure 4.37b. Again, a "terraced" structure is observed, and there are no indications of ductile features from these images.

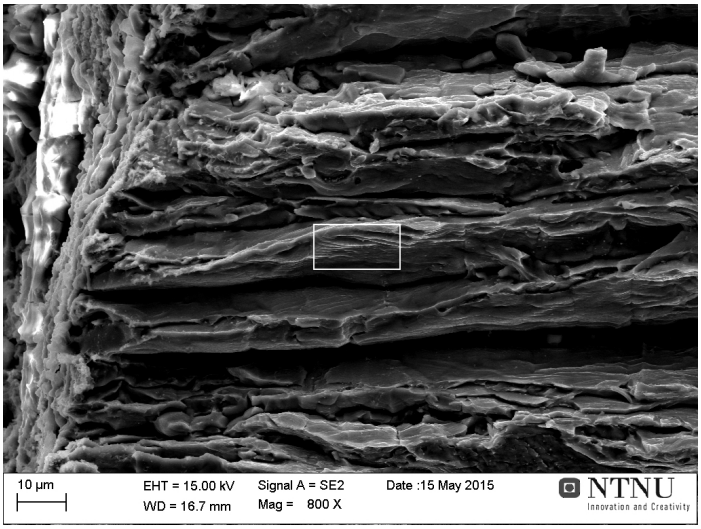

(a)

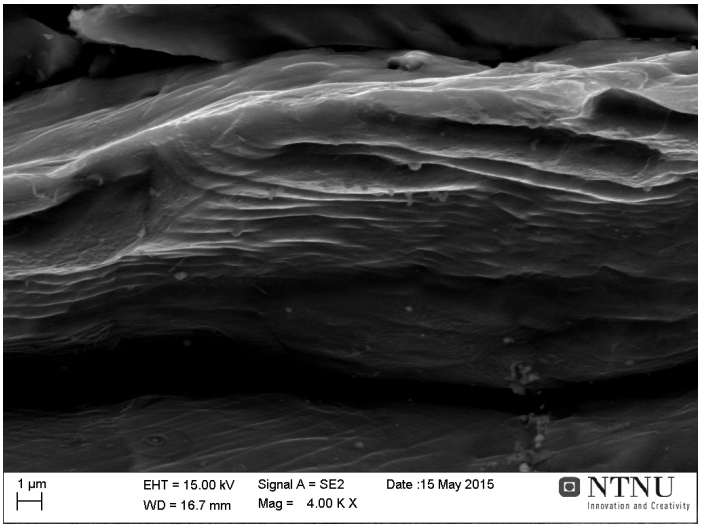

(b)

Figure 4.37: SEM images showing the fracture surface of a hydrogen pre-charged sample from the AA 7108.50 base material, 7108B, where **(a)** is a region close to the left edge (800× magnification), and **(b)**, is the same area at higher magnification (4000× magnification).

The SEM images in Figure 4.38 are also obtained from a hydrogen pre-charged sample of 7108B. These images reveal fine striations on almost flat faces. The flat faces are characteristic for transgranular cleavage fractures, and the crack arrest markings might be an indication of discontinuous crack propagation caused by time-dependent hydrogen diffusion. A SEM images from a reference sample of 7108B is shown in Figure 4.39, where the ductile features again are evident over the entire fracture surface.

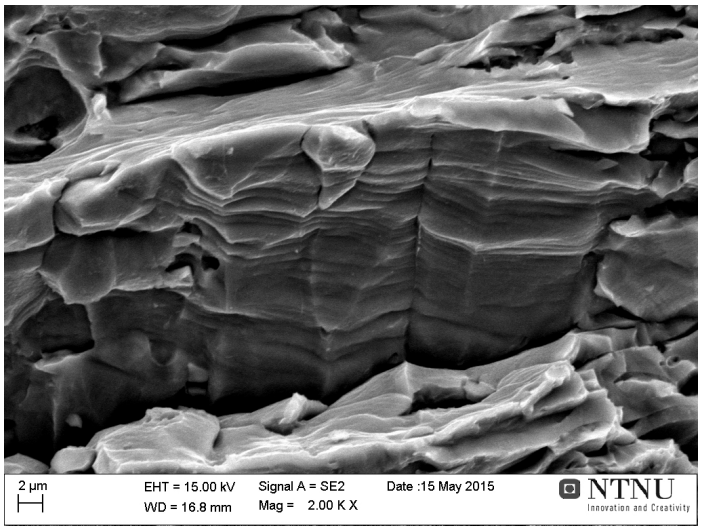

(a)

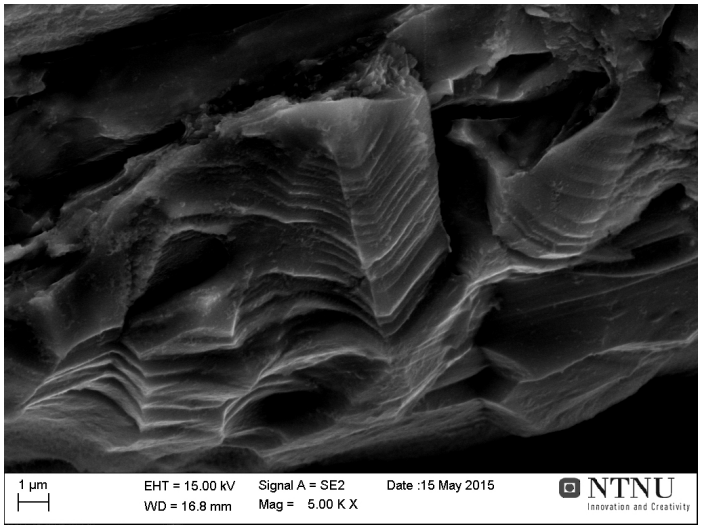

(b)

Figure 4.38: SEM images showing the left edge of the fracture surface for a hydrogen pre-charged sample from the AA 7108.50 base material, 7108B, at **(a)** 2000× magnification and **(b)**, at 5000× magnification.

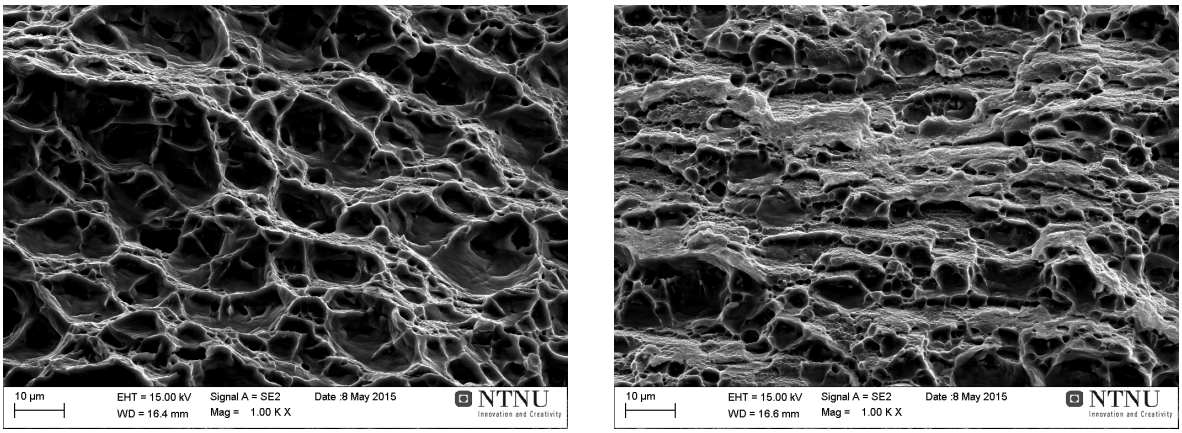

(a) **(b)**

Figure 4.39: SEM images showing **(a)** the left edge and **(b)** the middle region from the fracture surface of a reference sample from the AA 7108.50 base material, 7108B (1000× magnification).

One not pre-charged sample from 7108B, 7108BLP, was tensile tested at an applied potential of -1500 mV_{SCE}. The SEM images obtained from this sample are given in Figure 4.40. Figure 4.40a shows the left edge of the fracture surface, where the area to the right is characterized by ductile features. On the other hand, there is a region close to the notch with a completely different appearance. The region is magnified in Figure 4.40b, and from this image it seems to be cracking across the fracture surface. It is somewhat unclear why these cracks occur, but it might be cracking along subgrains. Again, the absence of ductile features can possibly be related to hydrogen effects. The middle region for the same sample revealed ductile features, and this is shown in Figure 4.40c.

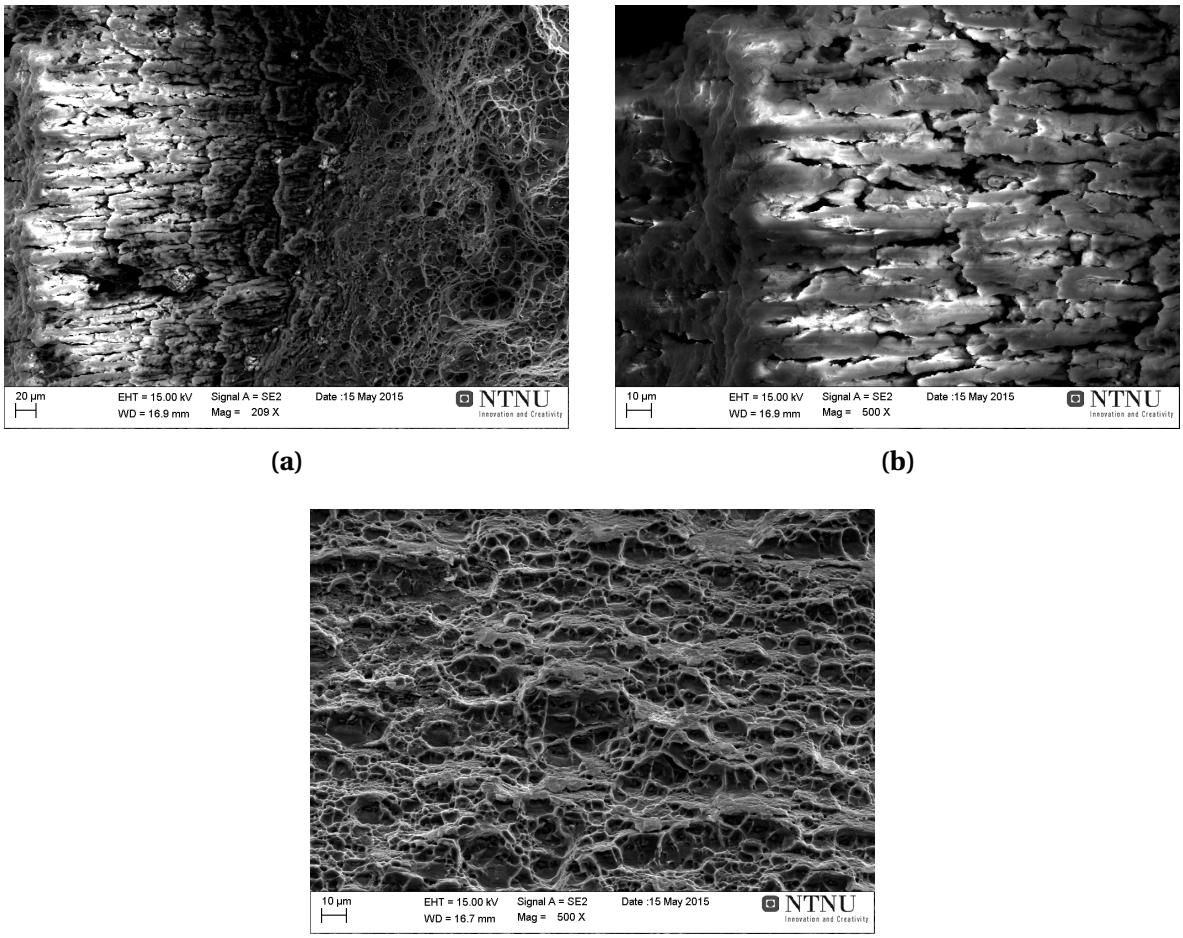

(a) **(b)**

(c)

Figure 4.40: SEM images showing the left edge at **(a)** 209× magnification and **(b)** at 500× magnification, and the middle region (500× magnification) from the fracture surface of a not pre-charged sample from the AA 7108.50 base material, 7108B. This sample was tensile tested at an applied potential of -1500 mV_{SCE}.

4.7 Reduction of area measurements

Reduction of area (RA) was measured as the difference in cross sectional area before and after tensile testing. Average RA values for hydrogen pre-charged samples, not pre-charged samples and reference samples together with their SD are given in Table 4.9-4.15 for each of the seven alloy variants. As mentioned in Section 2.4.2, loss in reduction of cross sectional area (RA_{loss}) is a frequently used measurement for reduction in ductility, and can hence be used to indicate HE susceptibility. The percentage loss in reduction of area (RA_{loss} [%]) was calculated between reference samples and hydrogen pre-charged samples according to Equation 2.10. These values are also included in Table 4.9-4.15.

Table 4.9: Average reduction of area (RA) values calculated for not pre-charged samples, hydrogen pre-charged samples and reference samples of the EN AW 5083 H321 base material, 5083B. Standard deviations (SD) are also included, and loss in reduction of area (RA_{loss}) is calculated between reference samples and hydrogen pre-charged samples.

	RA [%]	**SD**	**RA_{loss} [%]**
Air	20.8	0.1	30.8
Pre-charged	14.4	1.2	
Not pre-charged	14.9	3.6	-

Table 4.10: Average reduction of area (RA) values calculated for not pre-charged samples, hydrogen pre-charged samples and reference samples of the welded profile of EN AW 5083 H321, 5083BW. Standard deviations (SD) are also included, and loss in reduction of area (RA_{loss}) is calculated between reference samples and hydrogen pre-charged samples.

	RA [%]	**SD**	**RA_{loss} [%]**
Air	28.8	0.7	-9.8
Pre-charged	31.6	1.7	
Not pre-charged	32.3	1.2	-

Table 4.11: Average reduction of area (RA) values calculated for not pre-charged samples, hydrogen pre-charged samples and reference samples of sensitized EN AW 5083 H321, 5083BHT. Standard deviations (SD) are also included, and loss in reduction of area (RA_{loss}) is calculated between reference samples and hydrogen pre-charged samples.

	RA [%]	**SD**	**RA_{loss} [%]**
Air	21.2	4.6	-56.8
Pre-charged	33.2	4.0	
Not pre-charged	25.3	1.4	-

Table 4.12: Average reduction of area (RA) values calculated for not pre-charged samples, hydrogen pre-charged samples and reference samples of the EN AW 6082 T6 base material, 6082B. Standard deviations (SD) are also included, and loss in reduction of area (RA_{loss}) is calculated between reference samples and hydrogen pre-charged samples.

	RA [%]	**SD**	**RA_{loss} [%]**
Air	23.3	2.8	-11.9
Pre-charged	26.1	6.4	
Not pre-charged	21.3	7.3	-

Table 4.13: Average reduction of area (RA) values calculated for not pre-charged samples, hydrogen pre-charged samples and reference samples of the EN AW 6082 T6 alloy variant 6082C. Standard deviations (SD) are also included, and loss in reduction of area (RA_{loss}) is calculated between reference samples and hydrogen pre-charged samples.

	RA [%]	**SD**	**RA_{loss} [%]**
Air	32.0	2.8	-1.8
Pre-charged	32.5	1.8	
Not pre-charged	33.2	4.9	-

Table 4.14: Average reduction of area (RA) values calculated for not pre-charged samples, hydrogen pre-charged samples and reference samples of the EN AW 6082 T6 alloy variant 6082Z. Standard deviations (SD) are also included, and loss in reduction of area (RA_{loss}) is calculated between reference samples and hydrogen pre-charged samples.

	RA [%]	**SD**	**RA_{loss} [%]**
Air	35.6	2.2	1.6
Pre-charged	35.0	3.7	
Not pre-charged	38.0	8.3	-

Table 4.15: Average reduction of area (RA) values calculated for not pre-charged samples, hydrogen pre-charged samples and reference samples of the AA 7108.50 base material, 7108B. Standard deviations (SD) are also included, and loss in reduction of area (RA_{loss}) is calculated between reference samples and hydrogen pre-charged samples.

	RA [%]	**SD**	**RA_{loss} [%]**
Air	23.6	3.0	6.4
Pre-charged	22.1	0.8	
Not pre-charged	16.6	0.6	-

Great variations in RA_{loss} are observed for the different alloy variants in Table 4.9-4.15. While a RA_{loss} of -56.8 % was found for 5083BHT, the RA_{loss} for 5083B was determined to 30.8 %. It should be appreciated that the RA_{loss} calculations were based on the assumption of perfectly rectangular cross section areas when they were measured in SEM after tensile testing. Fracture surface examinations showed, however, that this assumption was not completely accurate for none of the samples.

Average RA values for hydrogen pre-charged samples and reference samples from all the alloy variants are presented in a scatterplot in Figure 4.41.

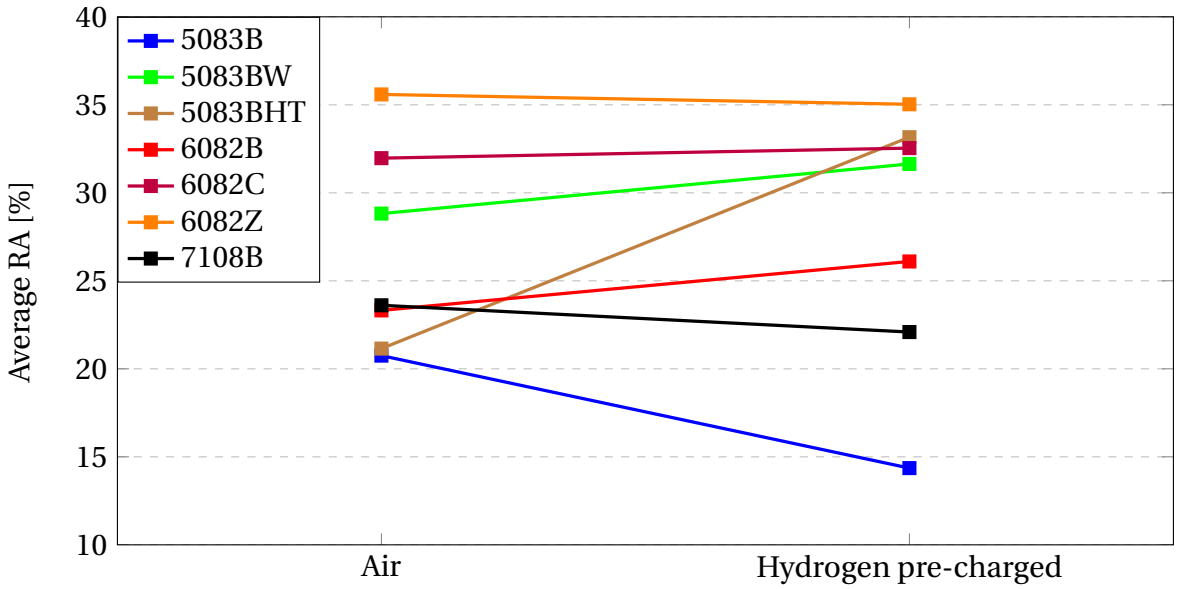

Figure 4.41: Scatterplot showing average reduction of area (RA) values for hydrogen pre-charged samples and reference samples from all the alloy variants.

4.8 Polarization curves

Potentiodynamic polarization curves were recorded for 5083B and 7108B, both with a sweep rate of 600 mV/h. The polarization curves are presented in Figure 4.42 and Figure 4.43, for 5083B and 7108B, respectively. Data from the OCP measurements are given in Appendix D.

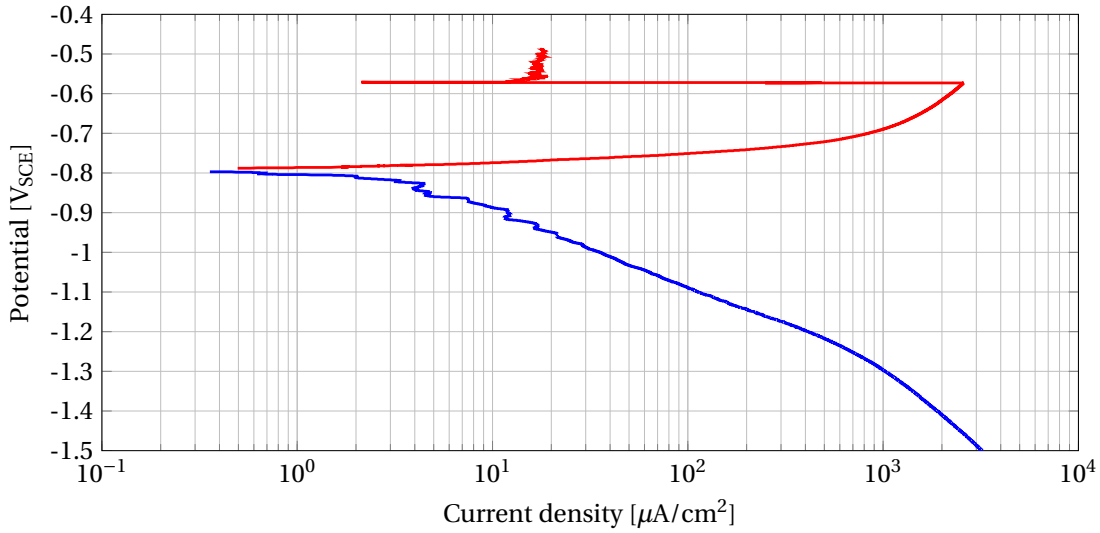

Figure 4.42: Polarization curve recorded for the EN AW 5083 H321 base material, 5083B, at a sweep rate of 600 mV/h.

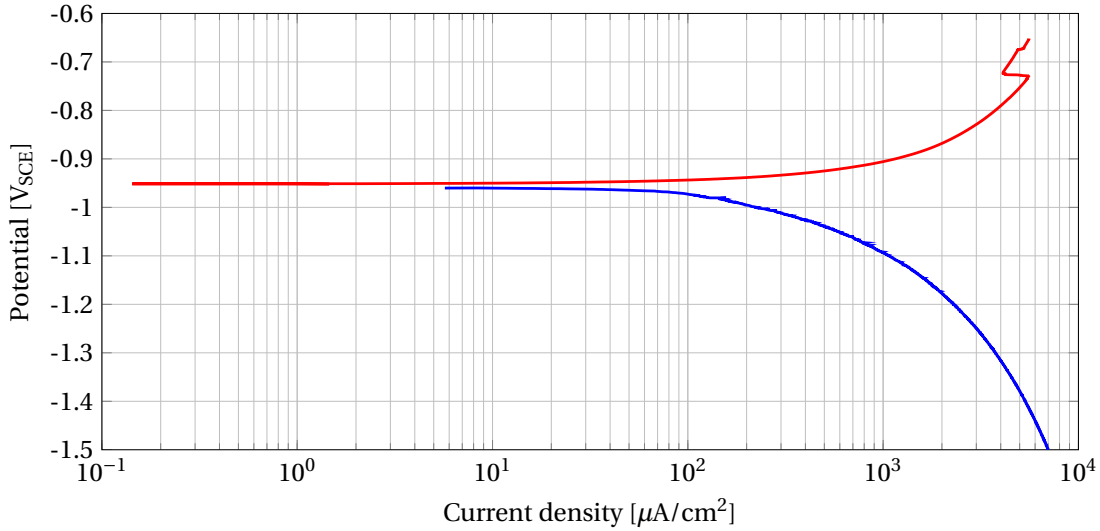

Figure 4.43: Polarization curve recorded for the AA7108.50 base material, 7108B, at a sweep rate of 600 mV/h.

The anodic Tafel constant, b_a, and the cathodic Tafel constant, b_c were found from the polarization curves in Figure 4.42 and Figure 4.43. The corrosion potential, E_{corr}, and the corrosion current density, i_{corr}, were also determined. Calculations are given in Appendix D, and the values are presented in Table 4.16.

Table 4.16: Table showing the anodic Tafel constant, b_a, the cathodic Tafel constant, b_k, the corrosion potential, E_{corr}, and the corrosion current density, i_{corr}, for the EN AW 5083 H321 base material, 5083B, and the AA 7108.50 base material, 7108B.

	b_a [mV/dec]	b_c [mV/dec]	E_{corr} [mV_{SCE}]	$\lvert i_{corr}\rvert$ [$\mu A/cm^2$]
5083B	23	-185	-800	3
7108B	31	-100	-950	80

Chapter 5

Discussion

In this study stepwise loading tensile tests, fracture surface examinations and reduction of area (RA) measurements were included in an effort to identify HE susceptibility for selected aluminium alloys. Firstly, some considerations about the choice of materials will be discussed. Secondly, the overall results will be briefly reviewed and related to existing literature. Thirdly, some factors that may have affected the susceptibility will be suggested and finally an evaluation of the testing methods will be given.

5.1 Materials

The EN AW 5083 H321 base material (hereinafter called 5083B) and the EN AW 6082 T6 base material (hereinafter called 6082B) were included in this study due to their combination of low weight, high strength and good corrosion resistance. This makes them suitable and recommended for use in seawater applications [2].

Welding is important in many applications including subsea structures and components, and a welded profile of EN AW 5083 H321 (hereby called 5083BW) was therefore also included. Welding includes high temperatures and subsequent alterations in composition and microstructure, and it is hence interesting to investigate whether these changes affect HE susceptibility. Furthermore, a sensitized variant of EN AW 5083 H321 (hereinafter called 5083BHT) was included with the purpose to investigate the effect of β-phase (Al_3Mg_2) formation on susceptibility to HE related to SCC. A number of investigators [26, 57, 66] have argued for a coupled AD and HE mechanism in SCC of AA 5083, and the idea was that the susceptibility to HE could be indicated. However, since CP is used to prevent corrosion, it is questionable whether the β-phase can affect HE susceptibility in absence of the AD reaction. Nevertheless, 5083BHT was implemented in all tests.

Two different alloy variants of EN AW 6082 T6 (hereinafter called 6082C and 6082Z) were also included to investigate whether variations in composition could alter the HE suscep-

tibility.

Lastly, it was decided to include an Al-Zn-Mg (7xxx) alloy, where susceptibility to HE has been widely studied and proven among researchers [5–10]. The choice of AA 7108.50 (hereinafter called 7108B) was based on its availability from the supplier.

5.2 Overall results

The overall test results indicate that cathodic polarization at an applied potential of -1093 mV_{SCE} affects the susceptibility to HE in the Al-Zn-Mg (7xxx) alloy variant 7108B, while the Al-Mg (5xxx) and Al-Mg-Si (6xxx) alloy variants are less affected.

Results from the stepwise loading tests of 7108B indicate that there might be an adverse effect from the presence of hydrogen on the mechanical properties of 7108B. This is claimed on the basis of significant differences in fracture strength (FS) between hydrogen pre-charged samples and reference samples, respectively. There was also a decline in FS for one of the not pre-charged samples compared to the reference samples. Average FS of the hydrogen pre-charged samples was reduced by almost 22 % of $R_{p0.2}$ from the reference samples, and a decline of approximately 4 % was also observed between the not pre-charged samples and the reference samples. Furthermore, the reduction in FS for the not pre-charged sample tensile tested at -1500 mV_{SCE} (7108BLP) was in between the hydrogen pre-charged samples and not pre-charged samples tensile tested at -1093 mV_{SCE}. Although the SD are relatively high for these values, and especially for the not pre-charged samples, the reduction in average FS for hydrogen pre-charged samples is significant. Moreover, since 7108B was the only sample tested at -1500 mV_{SCE}, it is somewhat difficult to assess the susceptibility to HE for this sample due to the high SD for the other samples. In accordance with results from the stepwise loading tensile tests, the fracture surface examinations revealed features supporting the involvement of hydrogen. These feature are related to the hydrogen pre-charged samples as well as the not pre-charged samples as seen from the SEM images in Figure 4.36a-4.36b, Figure 4.37 and Figure 4.38, where regions close to the notch shows brittle appearances. These images clearly demonstrate the absence of ductile features, where the surfaces are characterized by "terraced" structures with fine striations. When pre-cracked specimens are exposed to increased tension, triaxial stress states are created in the root of the notches [39]. It is therefore not surprising that the brittle features appear close to the notches, since hydrogen tends to accumulate into areas of high stresses [27]. In contrast, SEM images from the middle regions as shown

in Figure 4.39 provide clear evidence of ductile features. A reason for this may be that hydrogen had not reached these regions because of the low diffusivity.

Loss in ductility was also confirmed from the reduction of area (RA) measurements. A loss in reduction of area (RA_{loss}) of approximately 6 % was found between reference samples and hydrogen pre-charged samples, respectively. The RA measurements from this study should, however, be used carefully, and this will be further discussed later.

The stepwise loading tensile test results from the Al-Mg (5xxx) and Al-Mg-Si (6xxx) alloy variants do not indicate any effects from the presence of hydrogen. These findings were consistent for all alloy variants, regardless of both composition and heat treatment applied. Two of the alloy variants, 5083B and 5083BW, showed a decline in average FS between hydrogen pre-charged samples and reference samples of about 2 % and 11 % of $R_{p0.2}$, respectively. However, the same alloy variants exhibited the highest average FS for the not pre-charged samples. In fact, that was the case for all the alloy variants except for 6082B. It is difficult to explain this behaviour, but it nevertheless indicates any effect of hydrogen. Again, the SD associated with these values should be noted. There were some difficulties to keep a constant load between each incremental increase every hour for these alloy variants. This can be observed as stress fluctuations in the stress-time plots (Figure 4.5-4.10), and was due to cold creep. The most pronounced effect was experienced for the Al-Mg-Si (6xxx) alloy variants, likely because of the high Si content [16].

The stepwise loading tensile test results were also in accordance with findings from the fracture surface examinations. From the SEM images in Figure 4.17-4.34, ductile features are evident on all of the fracture surfaces. The dimples varied in amount, shape and size, and this is likely due to the microstructural variations as shown from the optical micrographs in Figure 4.1-4.3. Furthermore, the large proportion of dimples observed for 5083BW (Figure 4.20-4.22) can possibly be connected to a large amount of particles on the fracture surfaces. This is strong evidence indicating ductile fractures, where nucleation and growth of microvoids originates from cracking of particles.

Surprisingly, the RA measurements revealed both significant losses and unlikely high increases in ductility for the hydrogen pre-charged samples compared to the reference samples. The RA_{loss} values obtained from the Al-Mg (5xxx) and Al-Mg-Si (6xxx) alloy variants are summarized in Table 5.1. These findings are certainly not justified from neither the stepwise loading tensile test results or the fractographic examinations. It is suspected that this can be related to inaccurracy in measurements of the cross sectional areas. This will be further discussed later on.

Table 5.1: Loss in reduction of area (RA_{loss} [%]) between reference samples and hydrogen precharged samples from the Al-Mg (5xxx) and Al-Mg-Si (6xxx) alloy variants.

Alloy variant	RA_{loss} [%]
5083B	30.8
5083BW	-9.8
5083BHT	-56.8
6082B	-11.9
6082C	-1.8
6082Z	1.6

5.3 Comparing results with literature

There is lacking information in the literature when it comes to susceptibility to HE in Al-Mg (5xxx) and Al-Mg-Si (6xxx) aluminium alloys, and it is hence difficult to compare findings from this study with previous work. Based on the literature review, it is not surprising that the present study indicates a susceptibility to HE in 7108B. In fact, most studies regarding susceptibility to HE in aluminium alloys are related to high-strength aluminium alloys within the 7xxx series [6, 7, 9]. Hardwick et al. [6], Albrecht et al. (1982) [7] and Albrecht et al. (1978) [9] showed that the susceptibility to HE is a function of microstructure, where the greatest susceptibility was found for underaged microstructures. 7108B was artificially aged to the T6 temper, and this should hence indicate an intermediate susceptibility. Because this was the only microstructure investigated, the degree of susceptibility can hardly be assessed.

Important to note from the previous studies is that most experiments have been performed on alloys of considerably higher strength than 7108B. $R_{p0.2}$ in the range of 489-561 MPa has been reported [6,9], whereas the $R_{p0.2}$ of 7108B was 330 MPa. There are, however, other possible explanations. Hardwick et al. [6] claimed that the susceptibility to HE is a function of composition, and more particular the copper content. While an AA 7075 aluminium alloy with a copper content of 2.10 wt% was embrittled only for underaged microstructures, a low-copper alloy with 0.01 wt% Cu was embrittled for all microstructures. The embrittlement was assessed from RA measurements, and the embrittled low-copper alloy in the T6 temper showed a RA_{loss} of about 20 %. From the fact that 7108B contained 0.031 wt% copper (Table 3.1), this may have contributed to embrittlement. By comparing the values of RA_{loss}, the reduction in ductility is significantly lower for 7108B, with a RA_{loss} of about 6 %. However, these values are not directly comparable due to different sam-

ple geometries, and also because of inaccuracy in cross sectional area measurements as previously mentioned. Nevertheless, further support for embrittlement of 7108B is found from fractography. Figure 5.1 shows the fracture surface from the embrittled low-copper AA 7075 alloy together with the fracture surface from a hydrogen pre-charged sample of 7108B. It can be seen from these images that the fracture surfaces are characterized by "terraced" structures, with fine parallel striations on flat faces. These features can probably be related to discontinuous crack propagation as caused by time-dependent hydrogen diffusion. Flat faces are also characteristic for transgranular cleavage fractures, which are brittle in nature. Similar appearances were also observed under SCC of AA 7075 T7351 as shown in Figure 2.21, where hydrogen was believed to be involved in the cracking mechanism.

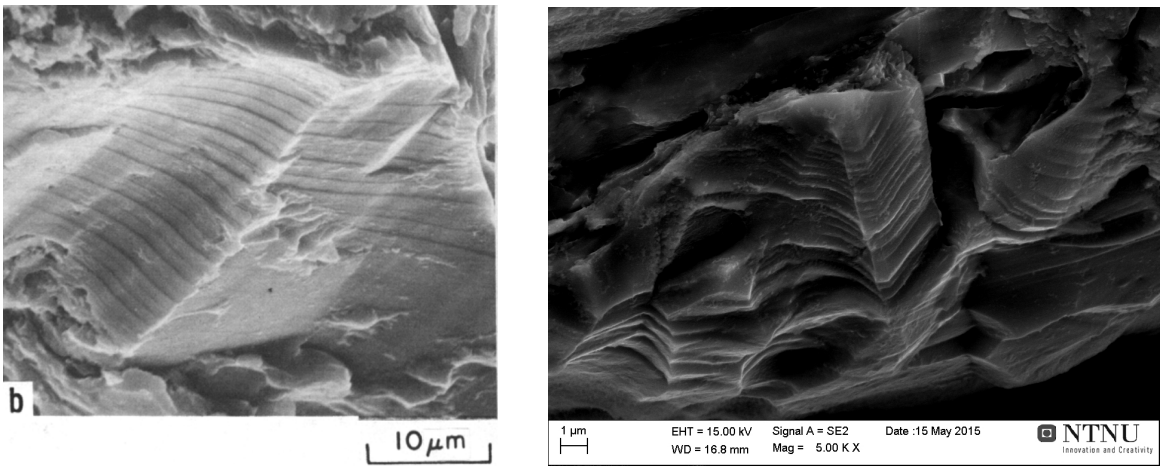

(a) **(b)**

Figure 5.1: SEM images from fracture surfaces of **(a)** a hydrogen pre-charged sample from the AA 7075 low-copper alloy [6] and **(b)** a hydrogen pre-charged sample from the AA 7108.50 base material, 7108B (5000× magnification). "Terraced" structures with fine parallel striations on flat faces are evident for both of the fracture surfaces.

5.4 Factors that may have affected the susceptibility to HE

This study has indicated that cathodic polarization has a different effect on susceptibility to HE in Al-Mg (5xxx) alloys/Al-Mg-Si (6xxx) and Al-Zn-Mg (7xxx) alloys. For that reason, it is interesting to discuss factors that may have affected the HE susceptibility.

It is reasonable to assume that composition play an important role regarding susceptibility to HE. The major differences in composition among the alloys investigated include (1) a high Zn content in 7108B (5.77 wt%), (2) a relatively high amount of Si in the Al-Mg-Si (6xxx) alloy variants (0.93-1.00 wt%) and (3) a high Mg content in the Al-Mg (5xxx) alloy variants (4.38 wt%). When it comes to Cu, the highest amount is found in 6082C (0.2 wt%), while 6082Z do not contain any Cu. The Cu content does not seems to affect the susceptibility to HE in Al-Mg-Si (6xxx) alloys based on the results obtained in this study. Al-Zn-Mg (7xxx) alloys generally contain large amounts of both Zn and Mg, and this may hence indicate that Zn has an adverse effect on susceptibility to HE. From strength considerations, there are only small variations between the alloys. In fact, the highest tensile strength (R_m) is found for 6082B (383.20 MPa).

The solubility of hydrogen in aluminium is very low (about $5.6 \cdot 10^{-8}$ wppm at 298 K [24]), and this may be a reason for increased resistance to HE in certain aluminium alloys. It is also possible that the critical amount of hydrogen necessary to provide HE is varying among the alloys. In this context, a measurement of the hydrogen content would have been useful. Moreover, trapping of hydrogen on lattice defects can significantly alter the solubility. For instance, increased solubility is found for decreasing grain sizes [30]. A more detailed examination of the microstructures could hence have been interesting. Because of the low hydrogen solubility, theories about hydrogen transport by dislocations have been proposed [25]. As cold creep also involves transport of dislocations, it might be expected that an increased amount of creep could enhance hydrogen transport eventually to promote embrittlement. However, this was certainly not the case for the Al-Mg-Si (6xxx) alloy variants where the creep occurrences were most pronounced.

Although these results have indicated an effect of cathodic polarization on the susceptibility to HE in 7108B, they need to be interpreted in conjunction with an evaluation of (1) the precharging method, (2) the stepwise loading tensile test, (3) the fractographic examinations and (4) the RA measurements.

5.5 Evaluation of experimental methods

5.5.1 Precharging

The applicability of the precharging procedure depends on whether or not hydrogen was introduced into the materials. From the fact that there is no experience by use of this

method for precharging of aluminium, it is somewhat difficult to predict the hydrogen content without having done measurements. However, this method has proven to be efficient in precharging of super duplex stainless steel (SDSS) by Andersen [19], where the same procedure revealed hydrogen contents in the range of 90-290 wppm. Although these findings should be used carefully, they might give an indication of what can be expected when using the same method for precharging of aluminium. It should also be appreciated that SDSS consists of both austenite and ferrite, from which the latter got a bcc structure where the hydrogen diffusivity will be higher. Nevertheless, from the diffusivities given in Table 2.6, the hydrogen diffusion rate is considerably higher in AA 5083 ($1.00 - 1.50 \cdot 10^{-10}$ cm^2/s at 298 K [26]) than in SDSS ($1.10 \cdot 10^{-15}$ cm^2/s at 295 K [27]). Also from the fact that the solubility of hydrogen in aluminium is very low, one might expect that saturation can be quickly achieved. However, there were no indications of HE for the hydrogen pre-charged samples from neither the Al-Mg (5xxx) alloy variants or the Al-Mg-Si (6xxx) alloy variants. This is likely a result of high resistance, and/or a low hydrogen uptake. The hydrogen pre-charged samples of 7108B showed brittle features close to the notch, and this can be explained by accumulation of hydrogen in areas of high stresses. It is also possible that the hydrogen diffusivity is too low to promote embrittlement further into the samples.

In previous work performed by the author [11] the samples were pre-charged by use of the same procedure, but with a constant applied current rather than a constant applied potential. However, experience with decreasing potential and increasing pH indicated pitting to occur according to the Pourbaix diagram in Figure 2.4, and it was therefore decided to use a constant applied potential in the present study. The current was not logged, but since the potential varied under a constant applied current, the opposite is also expected. Furthermore, because the current is directly related to the hydrogen evolution, the amount of hydrogen evolved was likely varying along the precharging period.

The presence of hydrogen was confirmed by observations of bubble formation on the sample surfaces. It should be noted, however, that the amount evolved seemed to be restricted. This can be connected to findings from Gundersen and Nisancioglu [22], who showed that the cathodic reactions during cathodic polarization of aluminium mainly occur on intermetallic particles. Since the proportion of intermetallic particles represents a small fraction of the total exposed surface area, the current requirements and hence the hydrogen evolution will be limited. Important to mention is that increased temperature also will increase the hydrogen evolution rate, and the precharging experiments were conducted at 80 °C.

Amount of hydrogen evolved also depends on other factors such as potential and pH. Both low potential and low pH are beneficial for increased hydrogen evolution, and this has been utilized in a number of studies where precharing has been conducted under more severe charging conditions. A widely used precharging method involves an electrolyte of HCl with pH 1, and an applied potential of -1500 mV_{SCE} [5–10]. Since this is a well-documented precharging procedure, it might questioned why the present precharging procedure was conducted under an applied potential of -1093 mV_{SCE} in a 3.5 % NaCl solution. Firstly, this study aims to simulate the actual conditions for subsea structures after several years of operation. Since the expected protection potential from CP is -1093 mV_{SCE} (-1050 $mV_{Ag/AgCl}$), this is the most appropriate potential to use. Secondly, by considering the Pourbaix diagram in Figure 2.4, a potential of -1500 mV_{SCE} in combination with pH 1 apparently leads to uniform corrosion. It should be appreciated that this Pourbaix diagram is based on the behaviour of AA 5086, and that different alloys are expected to behave different.

In order to provide a complete evaluation of the precharging method used, the hydrogen content should have been measured. Indeed, efforts were made to get these measurements carried out. Hydrogen measurements are not only important to validate this particular method as an applicable precharging procedure, but also in order to determine how vulnerable aluminium alloys are for hydrogen uptake. If it turns out that the hydrogen uptake is negligible, it may also be assumed that the threat regarding HE after several years in service is low.

5.5.2 Stepwise loading tensile test

The stepwise loading tensile test utilized in this study has become a useful method to assess the susceptibility to HE in various metals [23, 74]. Moreover, a similar testing procedure is described in the ASTM International standard F1624-12 [70]. In previous studies where susceptibility to HE in stainless steel (SS) and Incondel-718 has been investigated by using the same tensile test, significant reductions in FS have been found for hydrogen pre-charged samples. It is hence reasonable to assume that this method provides reliable information about susceptibility to HE, also for aluminium alloys.

The low cathodic current requirements for CP of aluminium as claimed by Gundersen and Nisancioglu [22] were confirmed from the current measurements shown in Appendix B, Figure B.1-B.8. However, there were great variations observed between the different alloy variants, and also between samples from the same alloy variant. Generally, lower

current requirements were observed for the hydrogen pre-charged samples compared to the samples not being pre-charged. According to Gundersen and Nisancioglu [22], the cathodic current requirements for CP of Al-Mg (5xxx) alloys (-1093 mV_{SCE}) is approximately 8.5 mA/m^2. The exposed surface area in the present study was about 1.05 cm^2, and this should result in a cathodic current of roughly 0.89 μA. As can be seen from the current time diagrams for Al-Mg (5xxx) alloy variants in Figure B.1-B.3, the current requirements were generally higher. A possible explanation is related to the increasing current requirements observed during leakages of electrolyte from the chambers. Leakages occurred because the glass windows in front of the chambers were attached by glue, in which disintegrated over time. However, these problems were solved by use of silicone, and can hence not explain the overall high cathodic current requirements observed. Moreover, it is important to note that the data from Gundersen and Nisancioglu [22] were recorded over a test period of 2 months, while the present experiments lasted for approximately 9 hours. Hence, the cathodic current requirements would probably have stabilized at a lower level over an extended period.

Another interesting finding is the varying amount of hydrogen evolution observed during tensile testing of the different samples. For the 7108BLP sample tested under an applied potential of -1500 mV_{SCE}, extensive hydrogen evolution was evident throughout the entire test. This observation is reasonable since a lower potential will increase the hydrogen evolution rate. This is also reflected in the current-time diagram shown in Figure B.8, where cathodic current requirements up to about 9 mA can be observed. In contrast, significant hydrogen evolution was only observed for a few of the samples tested at an applied potential of -1093 mV_{SCE}. Those were 5083B1 and 6082Z2, with current-time diagrams as shown in Figure B.1 and Figure B.6, respectively. Also for these samples the cathodic current requirements are high (up to 150 μA). Surprisingly is that the 5083BHTH2 sample (Figure B.3) and the 6082C1 sample (Figure B.5) did not reveal extensive hydrogen evolution, even with cathodic current requirements up to 200 μA. A possible explanation for this might be an increased atomic hydrogen absorption rate according to Equation 2.8, rather than recombination of atomic hydrogen to form gaseous hydrogen according to Equation 2.5 and Equation 2.6. Anyway, the general trend showing low hydrogen evolution can likely be understood from the low cathodic current requirements.

Localized corrosion in form of pitting was revealed on a few samples during the in situ optical microscope imaging. These observations were done both for samples with relatively low cathodic current requirements (*e.g* the 6082B1 sample in Figure B.4), and also for samples with higher cathodic current requirements (*e.g* the 5083B1 sample in Figure

B.1). A SEM image showing pitting on the 5083B1 sample is included in Appendix C, Figure C.1. A possible explanation for the pitting occurrence is that the oxide layer became unstable due to an alkalinization of the metal surface during hydrogen evolution. This is known as cathodic pitting [3]. The Pourbaix diagram in Figure 2.4 shows that pitting occurs at a pH of about 9 when the applied potential is -1093 mV_{SCE}. However, it is difficult to explain why pitting was observed only for a few samples, and regardless of the cathodic current requirements.

In order to verify the effect of in situ cathodic polarization on susceptibility to HE for both the hydrogen pre-charged samples and for the not pre-charged samples, measurements of hydrogen content should have been conducted. This is important in order to determine whether hydrogen supply during a short period of time can increase the hydrogen content in the pre-charged samples, but also in order to determine the hydrogen content in the not pre-charged samples. The latter is especially interesting since the highest FS values for most of the Al-Mg (5xxx) and Al-Mg-Si (6xxx) alloy variants were found for not pre-charged samples.

Sources of error

Although the implementation of the stepwise loading tensile test was quite straightforward, there are some uncertainties that need to be discussed.

In the present study seven alloy variants were included in order to gain information about susceptibility to HE. As a result, the number of parallels investigated was restricted due to time limitations, and only two samples from each of the alloy variants were tested under the same conditions. Anyway, these two samples are expected to give consistent results. The stepwise loading tensile tests showed, however, relatively large SD for all alloy variants. For the not pre-charged samples from the 7108B alloy variant, the high SD makes it difficult to assess the susceptibility to HE for these samples. Furthermore, there is no doubt that the generally high SD are challenging for the interpretations of the results obtained. A possible explanation for the high SD might be the presence of defects within the materials. Another explanation is related to the calculations of $R_{p0.2}$ [N], which were very sensitive to inaccuracy when the cross sectional areas were measured.

Due to great variations in $R_{p0.2}/R_m$-ratio between the different alloy variants, it was difficult to determine an appropriate initial load such that each test lasted for an acceptable amount of time. This led to some trial and error before a suitable initial load was deter-

mined, and hence variations in initial applied load both between the alloy variants and also between samples from the same alloy variant. However, it is uncertain to what extend these variations may have affected the FS obtained. Another remark regarding applied load is related to the notch effect. In this study, the presence of the notch was not taken into account when applied load was given in % of $R_{p0.2}$. The stress-strain behaviour adjacent to the notch is expected to be different from the bulk material due to stress concentrations, and this will probably affect the $R_{p0.2}$. Because the notch effect may influence the alloy variants differently, this may also have an impact of the results.

There will also be uncertainties related to the fact that load adjustments were done manually. For two of the samples (5083BW2 and 5083BHTH1), the load was accidently adjusted in the wrong direction. Moreover, there were difficulties regarding to keep an exact constant load between each incremental increase, due to some degree of creep for all the alloy variants.

5.5.3 Fractography

Fracture surface examination by use of SEM is often included in assessment of susceptibility to HE. This is an easy method to reveal effects of hydrogen as reflected by changes in the fracture surface morphology. Important to note is that changes between the alloy variants also are expected from their different microstructures, and that alterations in fracture surface appearances should not uncritically be related to hydrogen effects. Furthermore, there will be variations across the fracture surfaces due to high anisotropy in the materials. On the basis of indications of brittle features together with support from the literature, there is nevertheless reasonable to claim that the significant changes as observed between the Al-Mg (5xxx)/Al-Mg-Si (6xxx) alloy variants and 7108B can be attributed to hydrogen.

5.5.4 Reduction of area measurements

Loss in reduction of area (RA_{loss}) between reference samples and hydrogen pre-charged samples has frequently been used as a measurement for HE susceptibility [5–10]. The RA measurements in the present study showed, however, large inconsistency with both results from the stepwise loading tensile tests and with observations from the fracture surface examinations. The cross sectional area measurements performed in SEM may explain this inconsistency. Whereas the cross sectional areas were assumed to be perfectly rectangular, it turned out that the areas were highly irregular due to the presence of the

notch. The irregularity can be understood from non-uniform stresses across the fracture surfaces, with increased stress concentration in the root of the notch. In previous studies cylindrical samples were used, and they will probably exhibit a more uniform stress distribution.

The large inaccuracy in the cross sectional area measurements makes the RA_{loss} values highly unreliable, and these can hence not be included in the overall assessment regarding susceptibility to HE in this study.

5.6 Further work

Measuring the hydrogen content is essential for the reliability of the findings from this study, and should definitely be included in further work. This is also important in assessing the applicability of the precharging method used, which in turn is crucial to safely predict the long-term effects of CP on susceptibility to HE in aluminium alloys. It would also have been interesting to measure the hydrogen diffusivity in the alloy variants, in order to reveal differences that might have an affect on the susceptibility to HE.

Furthermore, it is strongly suggested that an increased number of parallels are included in the test matrix. This will make it much easier to identify extreme values and hence to draw conclusions. Also, the effect of increased stress concentration at the notch should be considered. The finite element simulation tool Abaqus can be used for an analysis of the stress distribution, and this may provide a more accurate value for $R_{p0.2}$. A more accurate measurement of the fracture surface area is also necessary in order to implement RA_{loss} as a reliable measurement of susceptibility to HE. This could probably be done in the SEM, by simply selecting the actual fracture area rather than assuming a perfectly rectangular fracture surface.

In the present study, it did not succeed to identify any crack initiation and/or propagation from the in situ optical microscope imaging. For future investigations, interrupted stepwise loading tensile tests before failure should therefore be considered. By stopping the tensile tests, crack initiation and propagation can be examined in the SEM. This may probably reveal microstructural features of importance for the susceptibility to HE. Moreover, the effect of microstructural features such as grain size, amount of precipitates etc. is a topic for further research, since the interactions between hydrogen and lattice defects significantly can alter the hydrogen solubility and, perhaps, the susceptibility to HE.

Finally, it would be interesting to perform stepwise loading tensile tests for extended periods in which will be more realistic for actual operating conditions. A combination of increased holding time at each stress level and more gradual load increases will hence be appropriate.

Chapter 6

Conclusion

In this master's thesis a stepwise loading tensile test with in situ cathodic polarization was performed on samples from several variants of Al-Mg (5xxx), Al-Mg-Si (6xxx) and Al-Zn-Mg (7xxx) aluminium alloys. Hydrogen pre-charged samples and samples not being pre-charged were tested, in addition to reference samples tensile tested in air. Fracture surface examinations and reduction of area (RA) measurements were also included in the effort to assess susceptibility to HE.

Results from this study indicate that cathodic polarization with an applied potential of -1093 mV_{SCE} affects the susceptibility to HE in AA 7108.50. In contrast, the EN AW 5083 H321 and EN AW 6082 T6 alloy variants appear to be less affected, regardless of both composition and thermal history. This is proposed on the basis of results from the stepwise loading tensile tests, where a decline in average fracture strength (FS) of almost 22 % of $R_{p0.2}$ was observed between reference samples and hydrogen pre-charged samples from AA 7108.50. Also the not pre-charged samples exhibited a reduction in FS compared to the reference samples, but these showed a significant standard deviation (SD). Furthermore, brittle features associated with transgranular cleavage fractures were revealed from the fracture surface examinations. These observations were also supported by findings from the literature. For the EN AW 5083 H321 and EN AW 6082 T6 alloy variants, only small variations in average FS were found between reference samples and hydrogen pre-charged samples, respectively. In fact, most of the alloy variants showed highest average FS for the not pre-charged samples. The fracture surface examinations revealed ductile features for all samples which confirm the negligible effect of the presence of hydrogen.

It should be noted that the reduction of area (RA) measurements were not included in the overall assessment of susceptibility to HE due to large inconsistency with the other test results. Moreover, measurement of hydrogen content and execution of experiments in which several parallel samples are tested are crucial for verification of the findings from this study.

Bibliography

[1] C. Knutsen, I. Kvale, and J. H. Nordlien. Aluminium Applied for Subsea Structures: Possibilities and Challenges. In *The Eleventh International Offshore and Polar Engineering Conference*. International Society of Offshore and Polar Engineers, 2001.

[2] Norwegian Peteroleum Industry. Aluminium Structural Design. Technical Report NORSOK M-121, September 1997.

[3] K. Nisancioglu. Corrosion and protection of aluminium alloys in seawater. In *Corrosion behaviour and protection of copper and aluminium alloys in seawater*, pages 145–155. Woodhead Publishing Ltd, 2007.

[4] International Organization for Standardization (ISO). Petroleum, petrochemical and natural gas industries - Materials selecetion and corrosion control for oil and gas production systems. Technical Report ISO 21457, September 2010.

[5] D. A. Hardwick, M. Taheri, A. W. Thompson, and I. M. Bernstein. Hydrogen Embrittlement in a 2000-Series Aluminum Alloy. *Metallurgical Transactions A*, 13(2):235–239, 1982.

[6] D. A. Hardwick, A. W. Thompson, and I. M. Bernstein. The Effect of Copper Content and Microstructure on the Hydrogen Embrittlement of Al-6Zn-2Mg Alloys. *Metallurgical Transactions A*, 14(12):2517–2526, 1983.

[7] J. Albrecht, I. M. Bernstein, and A. W. Thompson. Evidence for Dislocation Transport of Hydrogen in Aluminum. *Metallurgical Transactions A*, 13(5):811–820, 1982.

[8] J. Albrecht, B. J. McTiernan, I. M. Bernstein, and A. W. Thompson. Hydrogen Embrittlement in a High-Strength Aluminum Alloy. *Scripta Metallurgica*, 11(10):893–897, 1977.

[9] J. Albrecht, A. W. Thompson, and I. M. Bernstein. The Role of Microstructure in Hydrogen-Assisted Fracture of 7075 Aluminum. *Metallurgical Transactions A*, 10(11):1759–1766, 1979.

[10] M. Taheri, J. Albrecht, I. M. Bernstein, and A. W. Thompson. Strain-Rate Effects on Hydrogen Embrittlement of 7075 Aluminum. *Scripta Metallurgica*, 13(9):871 – 875, 1979.

[11] K. F. Veium. Hydrogen embrittlement of aluminium alloys for use subsea. Technical report, Norwegian University of Science and Technology, 2014.

[12] Hydro Aluminium. Aluminium, environment and society. http://www.hydro.com/upload/Subsites/Norge/Nedlastingssenter/Om%20Aluminium/Aluminium_environment-and-society.pdf. Accessed: 2015-03-21.

[13] European Aluminium Association and MATTER. http://http://aluminium.matter.org.uk. Accessed: 2015-03-21.

[14] R. D. Doherty and A. K. Vasudevan. *Aluminium Alloys - Contemporary Research and Applications*, volume 31. Academic Press, Inc., 1989.

[15] I. Polmear. *Light Alloys*. Butterworth-Heinemann, 4 edition, 2006.

[16] L. F. Mondolfo. *Aluminium alloys: Structure and Properties*. Butterworth & Co, Ltd., 1976.

[17] Ph. Gimenez, J. J. Rameau, and M. C. Reboul. Experimental pH Potential Diagram of Aluminum for Sea Water. *Corrosion*, 37(12):673–682, 1981.

[18] H. Ezuber, A. El-Houd, and F. El-Shawesh. A study on the corrosion behavior of aluminum alloys in seawater. *Materials & Design*, 29(4):801 – 805, 2008. Advances in Production and Processing of Aluminium 2nd International Conference on Advances in Production and Processing of Aluminium.

[19] K. Andersen. HISC in Super Duplex Stainless Steels. Master's thesis, Norwegian University of Science and Technology (NTNU), June 2013.

[20] Det Norske Veritas (DNV). Cathodic Protection Design. Technical Report DNV-RP-B401, October 2010.

[21] A. Barnoush. Hydrogen embrittlement. http://www.uni-saarland.de/fak8/wwm/research/phd_barnoush/hydrogen.pdf. Accessed: 2015-02-22.

[22] R. Gundersen and K. Nisancioglu. Cathodic Protection of Aluminum in Seawater. *Corrosion*, 46(4):279–285, 1990.

[23] R. Johnsen, B. Nyhus, S. Wästberg, and G. Ø. Lauvstad. New Improved Method For Hisc Testing Of Stainless Steels Under Cathodic Protection. 2007.

[24] R. Ambat and E.S. Dwarakadasa. Effect of hydrogen in aluminium and aluminium alloys: A review. *Bulletin of Materials Science*, 19(1):103–114, 1996.

[25] T. Ishikawa and R. B. McLellan. The diffusivity of hydrogen in aluminum. *Acta Metallurgica*, 34(6):1091–1095, June 1986.

[26] J. H. Ai, M. L. C. Lim, and J. R. Scully. Effective Hydrogen Diffusion in Aluminum Alloy 5083-H131 as a Function of Orientation and Degree of Sensitization. *Corrosion*, 69(12):1225–1239, 2013.

[27] V. Olden, C. Thaulow, and R. Johnsen. Modelling of hydrogen diffusion and hydrogen induced cracking in supermartensitic and duplex stainless steels. *Materials and Design*, 29(10):1934 – 1948, 2008.

[28] G. Stenerud. The Susceptibility to Hydrogen Induced Stress Cracking for Alloy 718 and Alloy 725. Master's thesis, Norwegian University of Science and Technology (NTNU), June 2014.

[29] G. Lu and E. Kaxiras. Hydrogen embrittlement of aluminum: The crucial role of vacancies. *Physical Review Letters*, 94(15):4, 2005.

[30] R. A. H. Edwards and W. Eichenauer. Reversible hydrogen trapping at grain boundaries in superpure aluminium. *Scripta Metallurgica*, 14(9):971 – 973, 1980.

[31] G. M. Scamans, N. J. H. Holroyd, and C. D. S. Tuck. The Role of Magnesium Segregation in the Intergranular Stress Corrosion Cracking of Aluminium Alloys. *Corrosion Science*, 27(4):329 – 347, 1987.

[32] R. Gibala and R. F. Hehemann. *Hydrogen Embrittlement and Stress Corrosion Cracking*. American Society for Metals, Metals Park, Ohio, 1984.

[33] R. G. Song, W. Dietzel, B. J. Zhang, W. J. Liu, M. K. Tseng, and A. Atrens. Stress corrosion cracking and hydrogen embrittlement of an Al–Zn–Mg–Cu alloy. *Acta Materialia*, 52(16):4727 – 4743, 2004.

[34] K. Ishikawa, H. Okuda, and Y. Kobayashi. Creep behaviors of highly pure aluminum at lower temperatures. *Materials Science and Engineering*, A234-236(0):154 – 156, 1997.

[35] R. Braun. Environmentally assisted cracking of aluminium alloys. *Materialwissenschaft und Werkstofftechnik*, 38(9):674–689, 2007.

[36] R. H. Jones, D. R. Baer, M. J. Danielson, and J. S. Vetrano. Role of Mg in the Stress Corrosion Cracking of an Al-Mg Alloy. *Metallurgical and Materials Transactions A*, 32(7):1699–1711, 2001.

[37] J. W. Watson, Y. Z. Shen, and M. Meshii. Effect of Cathodic Charging on the Mechanical Properties of Aluminium. *Metallurgical Transactions A-Physical Metallurgy and Materials Science*, 19(9):2299–2304, SEP 1988.

[38] R. J. Gest and A. R. Troiano. Stress Corrosion and Hydrogen Embrittlement in an Aluminum Alloy. *Corrosion*, 30(8):274–279, August 1974.

[39] J. R. Davis. *Corrosion of Aluminium and Aluminium Alloys*. Materials Park, OH: ASM International, 1999.

[40] M. O. Speidel. Stress corrosion cracking of aluminum alloys. *Metallurgical Transactions A*, 6(4):631–651, 1975.

[41] D. Najjar, T. Magnin, and T. J. Warner. Influence of critical surface defects and localized competition between anodic dissolution and hydrogen effects during stress corrosion cracking of a 7050 aluminium alloy. *Materials Science and Engineering: A*, 238(2):293 – 302, 1997.

[42] S-M. Lee, S-I. Pyun, and Y-G. Chun. A critical evaluation of the stress-corrosion cracking mechanism in high-strength aluminum alloys. *Metallurgical Transactions A*, 22(10):2407–2414, 1991.

[43] T. D. Burleigh. The Postulated Mechanisms for Stress Corrosion Cracking of Aluminum Alloys: A Review of the Literature 1980-1989. *Corrosion*, 47(2):89–98, February 1991.

[44] M. V. Hyatt. Use of Precracked Specimens in Stress Corrosion Testing of High Strength Aluminum Alloys. *Corrosion*, 26(11):487–503, 1970.

[45] ASTM International. Standard Test Method for Linear-Elastic Plane-Strain Fracture Toughness K_{IC} of Metallic Materials. Technical Report ASTM E 399, January 2013.

[46] J. L. Searles, P. I. Gouma, and R. G. Buchheit. Stress Corrosion Cracking of Sensitized AA5083 (Al-4.5 Mg-1.0 Mn). *Metallurgical and Materials Transactions A*, 32(11):2859–2867, 2001.

[47] R. Pathania and D. Tromans. Initiation of stress corrosion cracks in aluminum alloys. *Metallurgical Transactions A*, 12(4):607–612, 1981.

[48] N. J. H. Holroyd and G. M. Scamans. Stress Corrosion Cracking in Al-Zn-Mg-Cu Aluminum Alloys in Saline Environments. *Metallurgical and Materials Transactions A*, 44(3):1230–1253, 2013.

[49] M. Puiggali, A. Zieliński, J. M. Olive, E. Renauld, D. Desjardins, and M. Cid. Effect of microstructure on stress corrosion cracking of an Al-Zn-Mg-Cu alloy. *Corrosion science*, 40(4):805–819, 1998.

[50] K. Rajan, W. Wallace, and J. C. Beddoes. Microstructural study of a high-strength stress-corrosion resistant 7075 aluminium alloy. *Journal of Materials Science*, 17(10):2817–2824, 1982.

[51] B. Sarkar, M. Marek, and E. A. Starke. The Effect of Copper Content and Heat Treatment on the Stress Corrosion Characteristics of Ai-6Zn-2Mg-X Cu Alloys. *Metallurgical Transactions A*, 12(11):1939–1943, 1981.

[52] A. Zieliński. Hydrogen-enhanced stress-corrosion cracking of aluminum alloys. *Materials Science*, 34(4):469–475, 1998.

[53] ASTM International. Standard Practice for Slow Strain Rate Testing to Evaluate the Susceptibility of Metallic Materials to Environmentally Assisted Cracking. Technical Report ASTM G 129, November 2000.

[54] L. Ratke and W. Gruhl. Model Experiments Concerning The Mechanism of Stress-Corrosion Cracking of AlZnMg Alloys. *Werkstoffe und Korrosion-Materials and Corrosion*, 31(10):768–773, 1980.

[55] M. Helbæk and S. Kjelstrup. *Fysikalsk kjemi*. Fagbokforlaget Vigmostad & Bjerke AS, 2 edition, 2009.

[56] G. M. Scamans. Discontinuous Propagation of Stress-Corrosion Cracks in Al-Zn-Mg Alloys. *Scripta Metallurgica*, 13(4):245–250, 1979.

[57] J. R. Pickens, J. R. Gordon, and J. A. S. Green. The effect of loading mode on the stress-corrosion cracking of aluminum alloy 5083. *Metallurgical Transactions A*, 14(4):925–930, 1983.

[58] N. H. L. Ewalds and R. J. H. Wanhill. The Three Modes of Loading. `http://thediagram.com/12_3/thethreemodes.html`. Accessed: 2015-02-11.

[59] L. Christodoulou and H. M. Flower. Hydrogen Embrittlement and Trapping in Al-6 %-Zn-3 %-Mg. *Acta Metallurgica*, 28(4):481–487, 1980.

[60] G. M. Scamans. Hydrogen bubbles in embrittled Al-Zn-Mg alloys. *Journal of Materials Science*, 13(1):27–36, 1978.

[61] G. M. Scamans, R. Alani, and P. R. Swann. Pre-Exposure Embrittlement and Stress Corrosion Failure in Al-Zn-Mg Alloys. *Corrosion Science*, 16(7):443 – 459, 1976.

[62] S. Maitra. Determination of Stress Corrosion Cracking Resistance of Al-Cu-Mg Alloys by Slow Strain Rate and Alternate Immersion Testing. *Corrosion*, 37(2):98–103, 1981.

[63] M. P. Mueller, A. W. Thompson, and I. M. Bernstein. Stress Corrosion Behavior of 7075 Aluminum in 1N Aluminum Chloride Solutions. *Corrosion*, 41(3):127–136, 1985.

[64] M. G. Fontana and R. W. Staehle. *Advances in Corrosion Science and Technology*, volume 2. Plenum Press, New York-London, 1972.

[65] R. Goswami, G. Spanos, P. S. Pao, and R. L. Holtz. Precipitation behavior of the ß phase in Al-5083. *Materials Science and Engineering: A*, 527(4–5):1089 – 1095, 2010.

[66] R. H. Jones, J. S. Vetrano, and C. F. Windisch Jr. Stress Corrosion Cracking of Al-Mg and Mg-Al Alloys. *Corrosion*, 60(12):1144–1154, 2004.

[67] J. A. Lyndon, R. K. Gupta, M. A. Gibson, and N. Birbilis. Electrochemical behaviour of the β-phase intermetallic (Mg_2Al_3) as a function of pH as relevant to corrosion of aluminium–magnesium alloys. *Corrosion Science*, 70(0):290 – 293, 2013.

[68] Hydro. Mechanical properties in Heat Affected Zone of welded EN AW 5083 H321. Technical report, August 2014.

[69] S. M. W. Breivik and E. F. Thomsen. Perforation of Welded Aluminium Structures. Master's thesis, Norwegian University of Science and Technology (NTNU), June 2014.

[70] ASTM International. Standard Test Method for Measurement of Hydrogen Embrittlement Threshold in Steel by the Incremental Step Loading Technique. Technical Report ASTM F1624 - 12, November 2012.

[71] M. Stoknes. Effect of Copper and Zinc of Corrosion Behaviour and Mechancial Properties in 6082-Alloys. Master's thesis, Norwegian University of Science and Technology (NTNU), June 2015.

[72] B. E. Sakshaug. Korrosjonsoppførsel av 5083- og 6082-legeringer ved ulike temperaturer. Master's thesis, Norwegian University of Science and Technology (NTNU), June 2015.

[73] Trond Furu. Materials Certificate for the alloys 7108 and 7030: Preparation and characterization of industrial starting material. Technical report.

[74] A. C. Haaland. Hydrogen induced stress cracking of alloy 718: Effects of chemical composition and microstructure. Master's thesis, Norwegian University of Science and Technology (NTNU), June 2013.

[75] E. Bardal. *Korrosjon og Korrosjonsvern*. Tapir Akademiske Forlag, Trondheim, Norway, 3 edition, 2010.

Appendix A

Tensile testing

A standard tensile test procedure was conducted to determine yield strength ($R_{p0.2}$) and tensile strength (R_m) of sensitized EN AW 5083 H321, 5083BHT, and of two EN AW 6082 T6 alloy variants, 6082C and 6082Z. The tensile test samples were machined by NOMEK AS according to the dimensions given in Figure A.1.

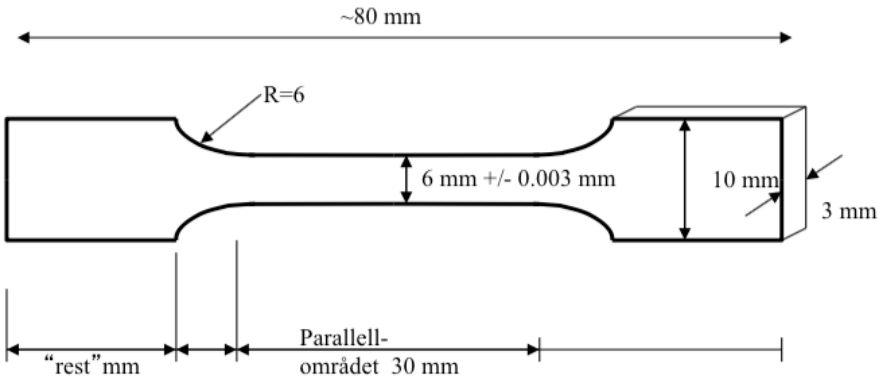

Figure A.1: Dimensions of the tensile test samples.

Three parallels from each alloy variant were tested, and the stress-strain curves are presented in Figure A.2-A.4. The correpospondig values of $R_{p0.2}$ and R_m are given in Table A.1-A.3.

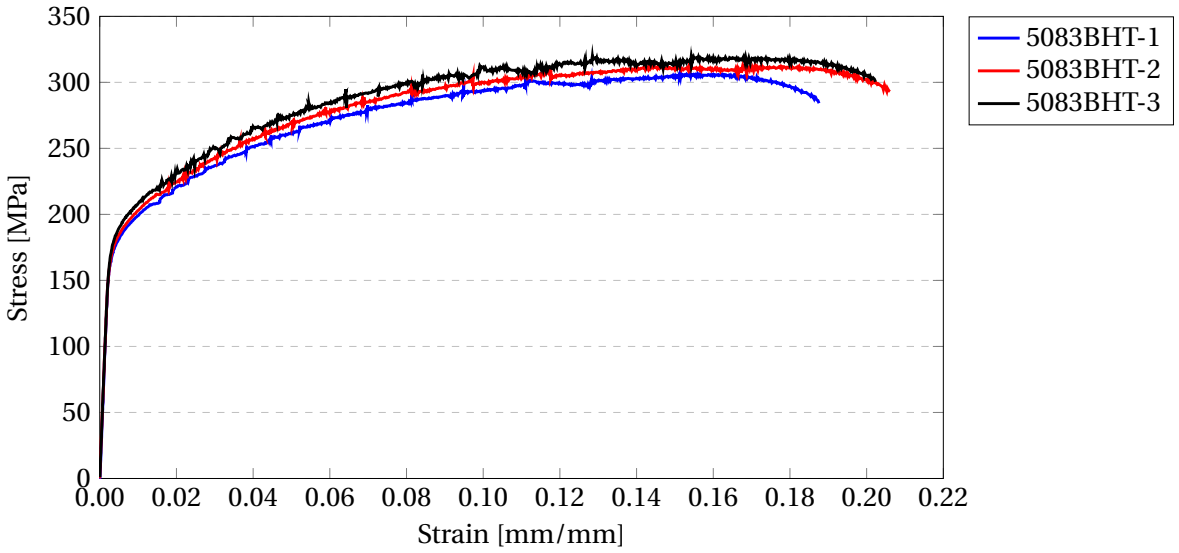

Figure A.2: Stress-strain curves obtained from tensile testing of sensitized EN AW 5083 H321, 5083BHT. Three parallels were included.

Table A.1: Yield strength ($R_{p0.2}$) and tensile strength (R_m) obtained from tensile testing of sensitized EN AW 5083 H321, 5083BHT. Three parallels were included and average values were determined.

	$R_{p0.2}$ [MPa]	**R_m [MPa]**
5083BHT-1	178.58	307.26
5083BHT-2	181.60	312.89
5083BHT-3	185.93	319.63
Average	182.04	313.26

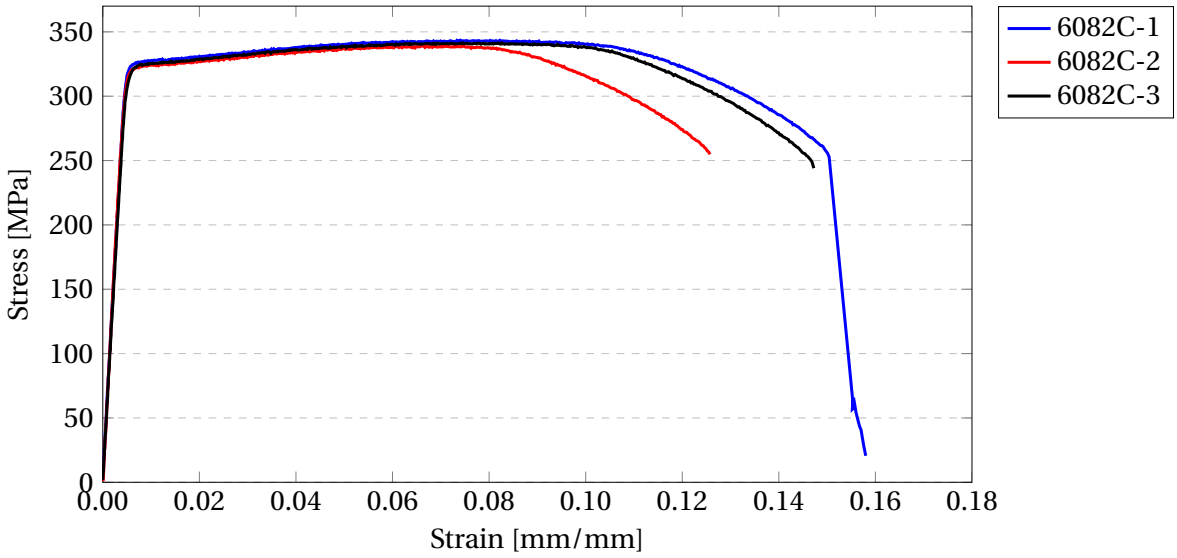

Figure A.3: Stress-strain curves obtained from tensile testing of the EN AW 6082 T6 alloy variant 6082C. Three parallels were included.

Table A.2: Yield strength ($R_{p0.2}$) and tensile strength (R_m) obtained from tensile testing of the EN AW 6082 T6 alloy variant 6082C. Three parallels were included and average values were determined.

	$R_{p0.2}$ [MPa]	**R_m [MPa]**
6082C-1	325.96	343.48
6082C-2	321.58	339.27
6082C-3	323.28	341.39
Average	323.61	341.38

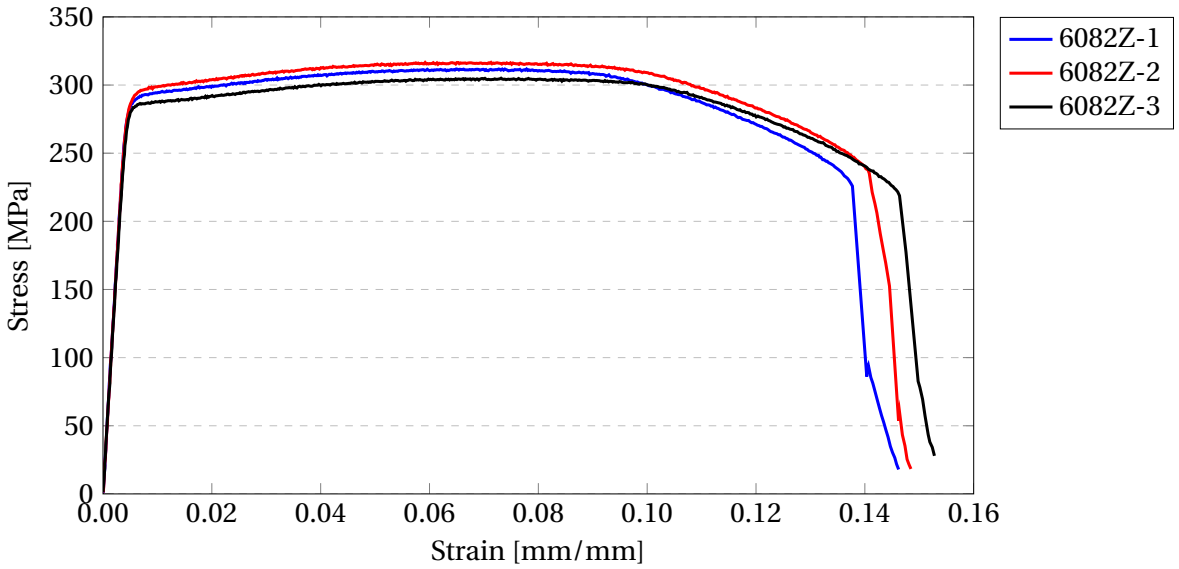

Figure A.4: Stress-strain curves obtained from tensile testing of the EN AW 6082 T6 alloy variant 6082Z. Three parallels were included.

Table A.3: Yield strength ($R_{p0.2}$) and tensile strength (R_m) obtained from tensile testing of the EN AW 6082 T6 alloy variant 6082Z. Three parallels were included and average values were determined.

	$R_{p0.2}$ [MPa]	**R_m [MPa]**
6082Z-1	289.79	311.80
6082Z-2	295.14	316.63
6082Z-3	285.72	305.04
Average	290.22	311.15

Appendix B

Current curves

Current-time curves from the tensile tests with in situ cathodic polarization are presented in Figure B.1-B.8.

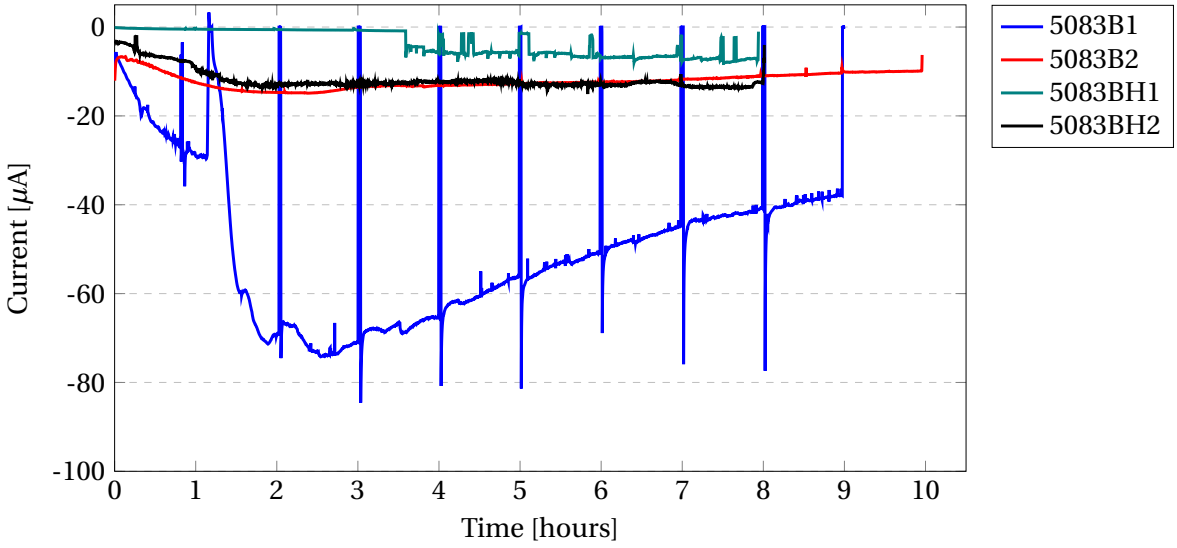

Figure B.1: Plot showing the current-time behaviour during tensile testing of the EN AW 5083 H321 base material, 5083B, for not pre-charged samples (5083B1-2) and hydrogen pre-charged samples (5083BH1-2). Applied potential was -1093 mV_{SCE}.

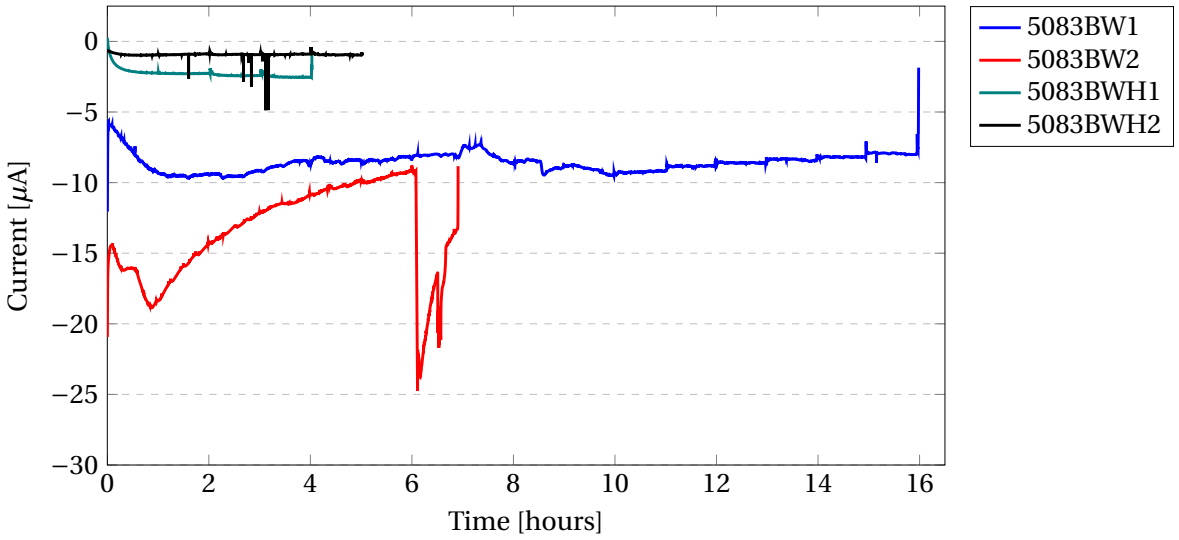

Figure B.2: Plot showing the current-time behaviour during tensile testing of the welded profile of EN AW 5083 H321, 5083BW, for not pre-charged samples (5083BW1-2) and hydrogen pre-charged samples (5083BWH1-2). Applied potential was -1093 mV_{SCE}.

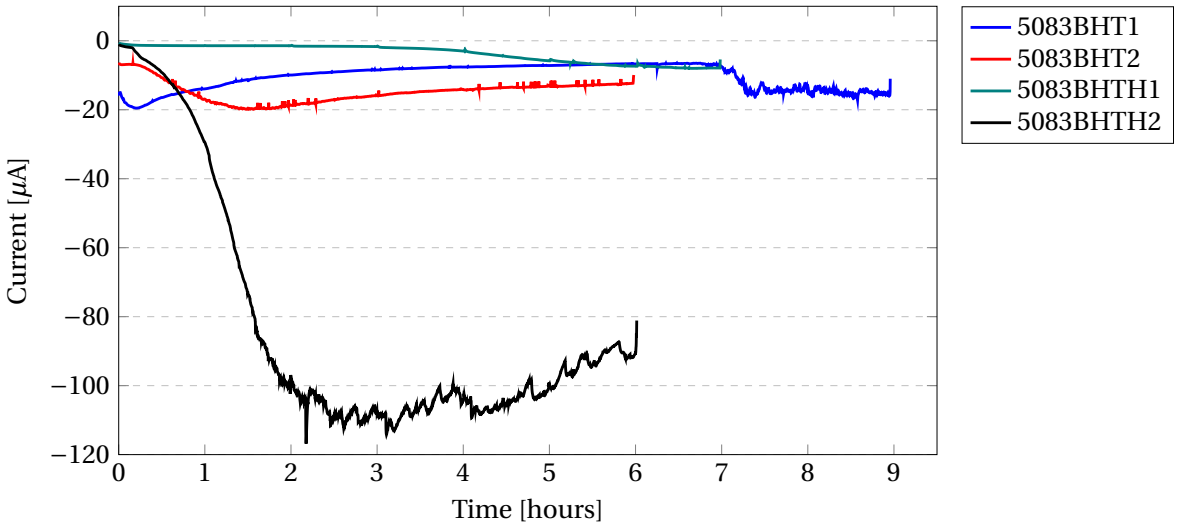

Figure B.3: Plot showing the current-time behaviour during tensile testing of sensitized EN AW 5083 H321, 5083BHT, for not pre-charged samples (5083BHT1-2) and hydrogen pre-charged samples (5083BHTH1-2). Applied potential was -1093 mV_{SCE}.

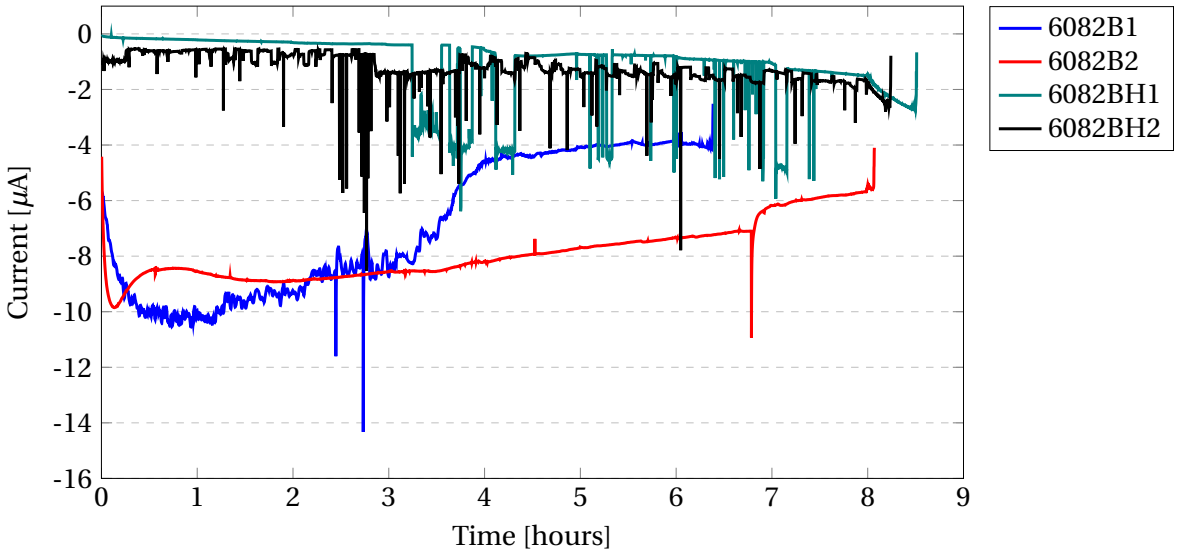

Figure B.4: Plot showing the current-time behaviour during tensile testing of the EN AW 6082 T6 base material, 6082B, for not pre-charged samples (6082B1-2) and hydrogen pre-charged samples (6082BH1-2). Applied potential was -1093 mV_{SCE}.

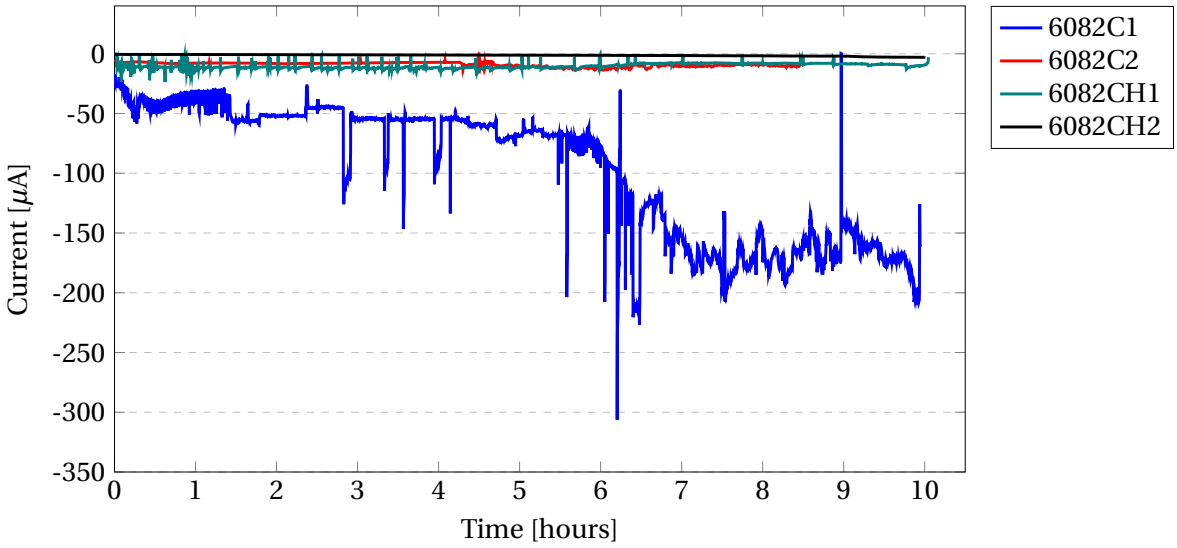

Figure B.5: Plot showing the current-time behaviour during tensile testing of the EN AW 6082 T6 alloy variant 6082C, for not pre-charged samples (6082C1-2) and hydrogen pre-charged samples (6082CH1-2). Applied potential was -1093 mV_{SCE}.

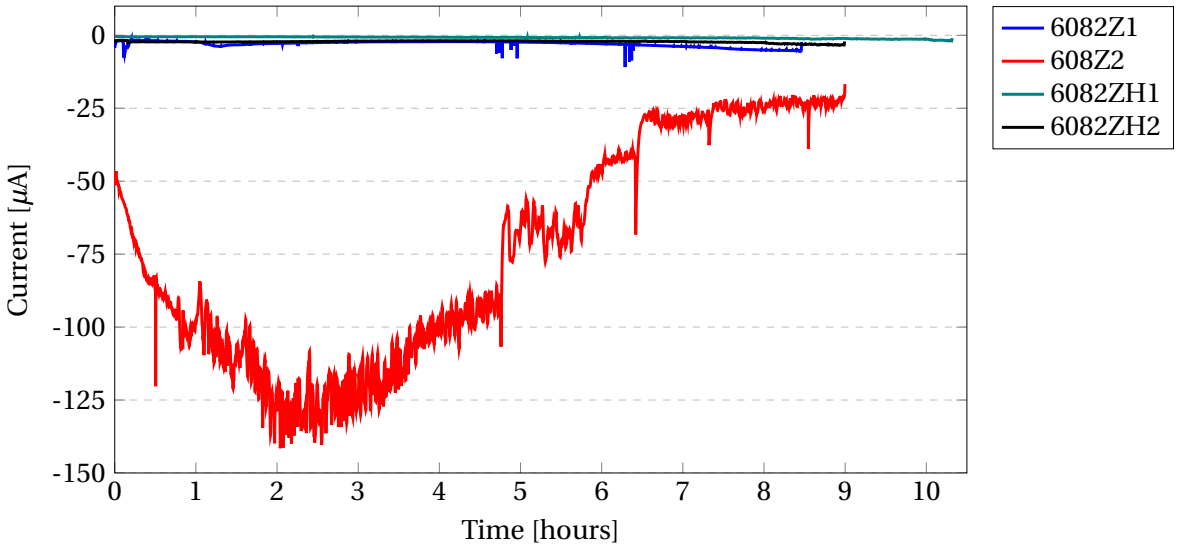

Figure B.6: Plot showing the current-time behaviour during tensile testing of the EN AW 6082 T6 alloy variant 6082Z, for not pre-charged samples (6082Z1-2) and hydrogen pre-charged samples (6082ZH1-2). Applied potential was -1093 mV_{SCE}.

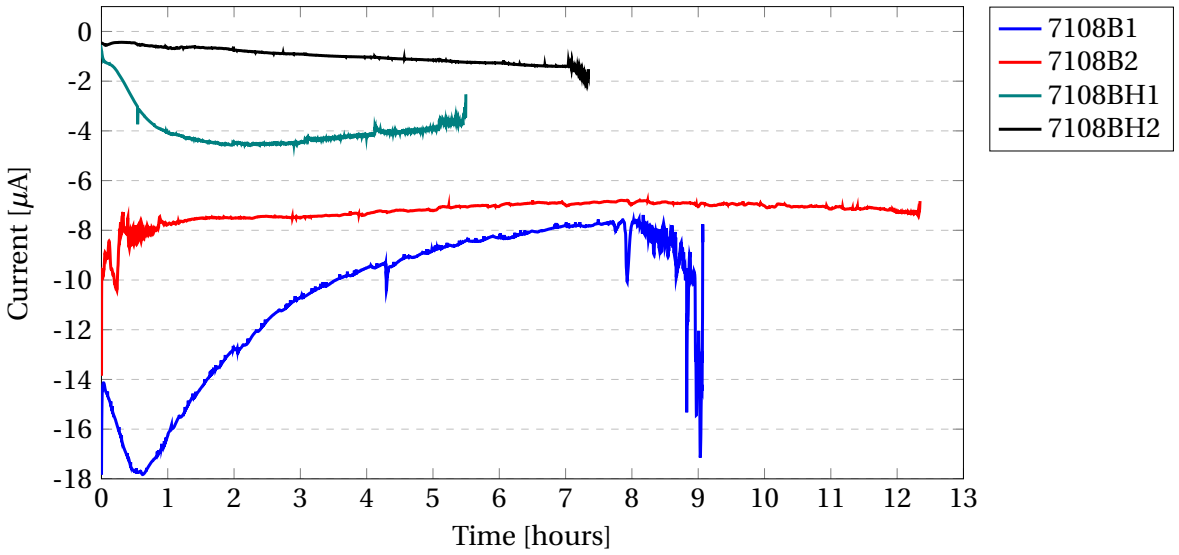

Figure B.7: Plot showing the current-time behaviour during tensile testing of the AA 7108.50 base material, 7108B, for not pre-charged samples (7108B1-2) and hydrogen pre-charged samples (7108BH1-2). Applied potential was -1093 mV_{SCE}.

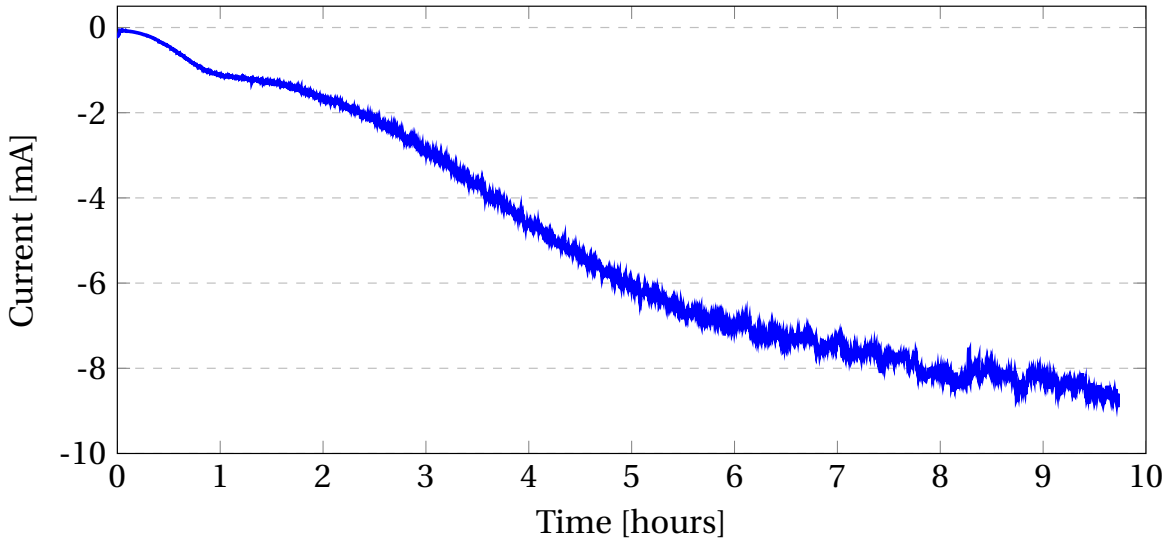

Figure B.8: Plot showing the current-time behaviour during tensile testing of the AA 7108.50 base material, 7108B, for the not pre-charged sample 7108BLP. Applied potential was -1500 mV_{SCE}.

Appendix C

Examination of pitting occurrence

The observed pitting after tensile testing with in situ cathodic polarization was examined by use of SEM. Figure C.1 shows a SEM image obtained from the not pre-charged 5083B1 sample.

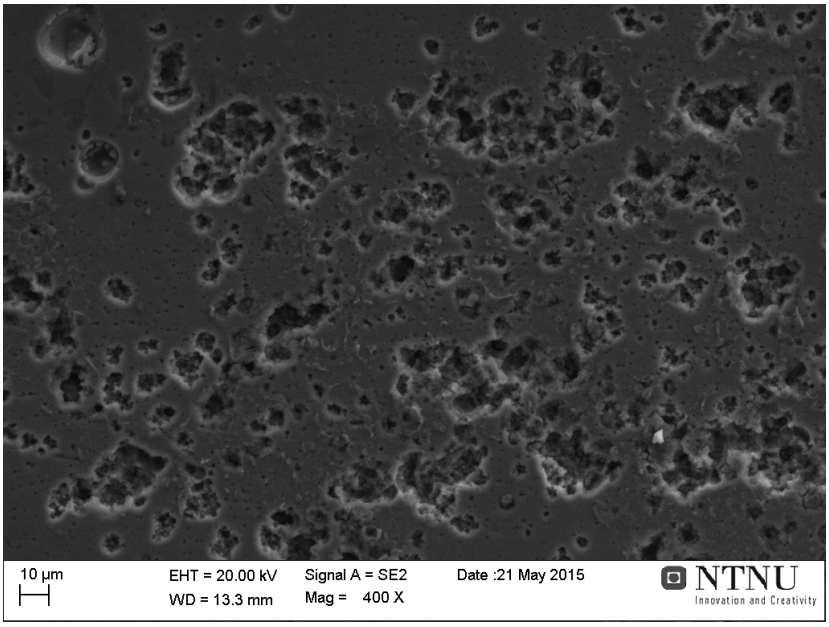

Figure C.1: SEM image showing the pitting occurence on the not pre-charged 5083B1 sample from the EN AW 5083 H321 base material, 5083B. The pits were observed after tensile testing with in situ cathodic polarization (400× magnification).

Appendix D

Open circuit potential curves

OCP measurements were conducted both before the cathodic polarization curves were recorded and before the anodic polarization curves were recorded. OCP curves from the EN AW 5083 H321 base material, 5083B, are presented in Figure D.1-D.2, while OCP curves from the AA 7108.50 base material, 7108B, are presented in Figure D.3-D.4

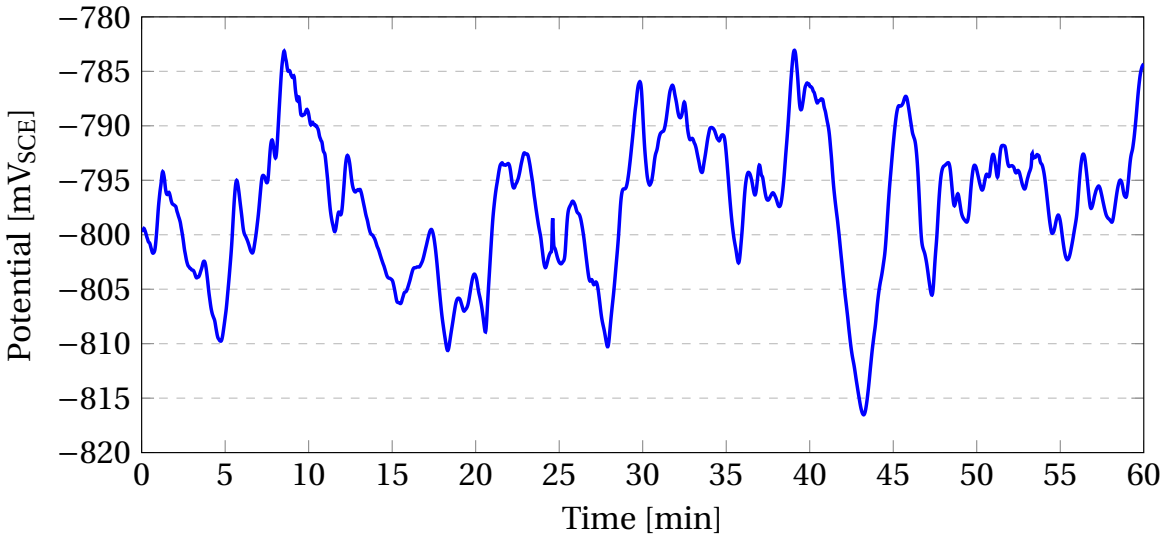

Figure D.1: Open circuit potential (OCP) curve for the EN AW 5083 H321 base material, 5083B, measured before the cathodic polarization curve was recorded.

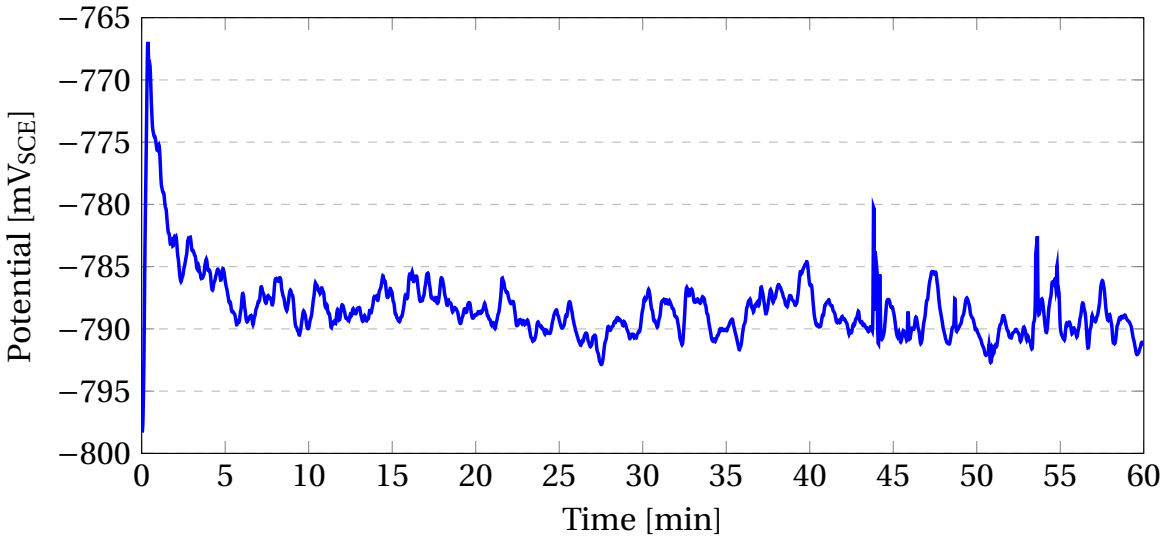

Figure D.2: Open circuit potential (OCP) curve for the EN AW 5083 H321 base material, 5083B, measured before the anodic polarization curve was recorded.

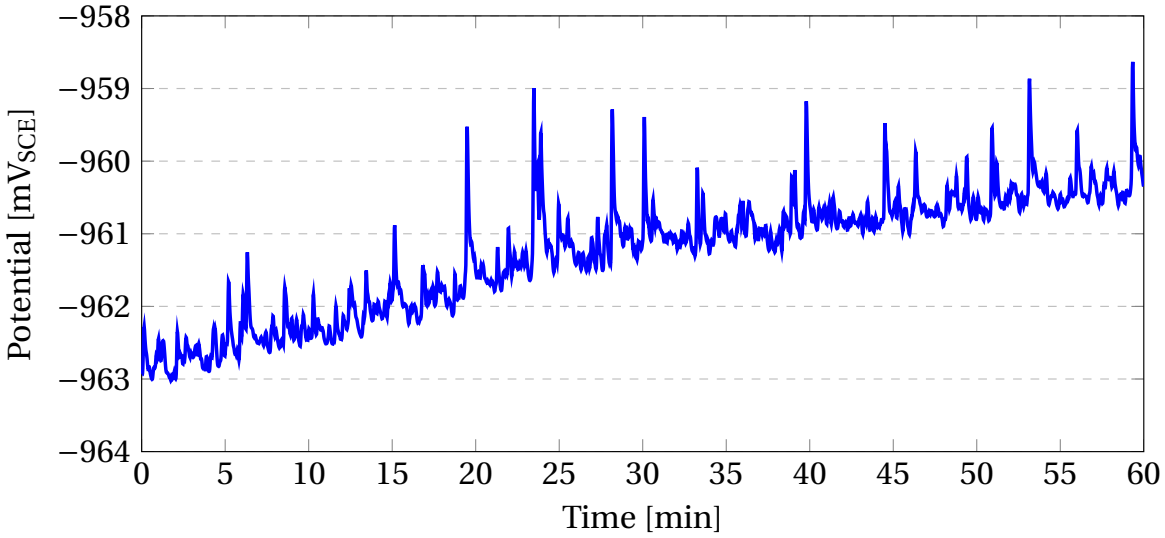

Figure D.3: Open circuit potential (OCP) curve for the AA 7108.50 base material, 7108B, measured before the cathodic polarization curve was recorded.

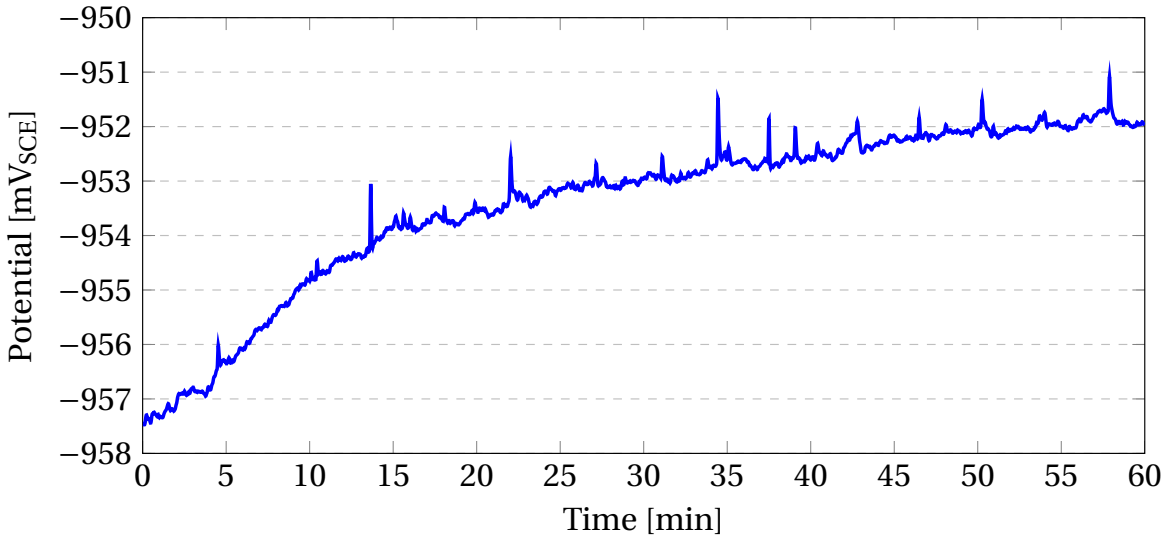

Figure D.4: Open circuit potential (OCP) curve for the AA 7108.50 base material, 7108B, measured before the anodic polarization curve was recorded.

A relationship between the current density, i, and the overpotential, η, is for an activation controlled polarization process given by Tafel's equation according to Equation D.1, where b is the Tafel slope and i_0 is the exchange current density [75].

$$\eta = b \cdot log \frac{i}{i_0} \tag{D.1}$$

Tafel's equation can be expressed both for the anodic curve and the cathodic curve, as shown in Equation D.2 and Equation D.3.

$$\eta_a = b_a \cdot \log \frac{i_a}{i_0} \tag{D.2}$$

$$\eta_c = b_c \cdot \log \frac{i_c}{i_0} \tag{D.3}$$

b_a and b_c can be determined from the slopes of the tangents in the linear parts of the polarization curves. Furthermore, the corrosion potential, E_{corr}, and the corrosion current density, i_{corr}, are found from the intersections of the tangents. Figure D.5 and Figure D.6 shows the polarization curves for 5083B and 7108B, where the tangents are included.

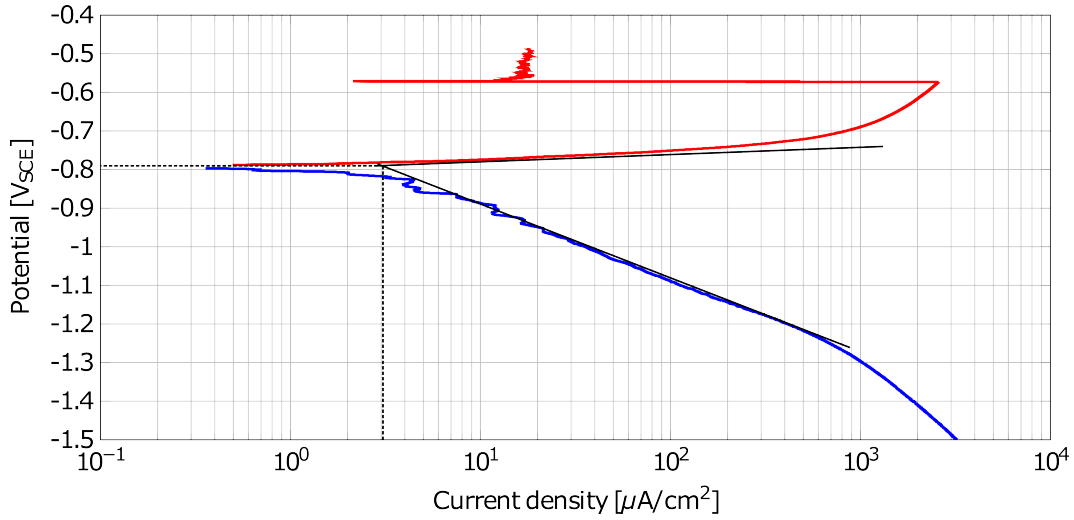

Figure D.5: Polarization curve for the EN AW 5083 H321 base material, 5083B, where cathodic and anodic Tafel constants were found from the slope of the tangents. E_{corr} and i_{corr}, were found from the intersection of the tangents.

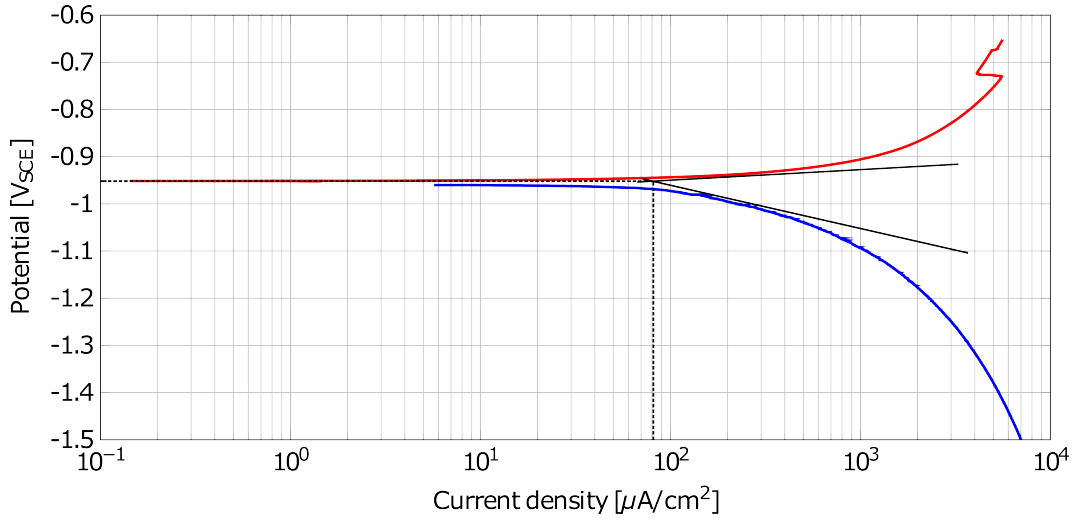

Figure D.6: Polarization curve for the AA 7108.50 base material, 7108B, where cathodic and anodic Tafel constants were found from the slope of the tangents. E_{corr} and i_{corr}, were found from the intersection of the tangents.